DEVELOPMENT OF A NEW EULER-LAGRANGE MODEL FOR THE PREDICTION OF SCOUR AROUND OFFSHORE STRUCTURES

Thesis submitted in accordance with the requirements of
the University of Liverpool for the degree of Doctor in Philosophy
by

YARU LI

November 2015

Contents

Illustrations

List of Figures

List of Tables

Notations

A	particle acceleration
C_d	drag coefficient
D	cylinder diameter
d_{50}	particle median grain size
D_p	parameter related to drag coefficient
g	gravitational acceleration
h	water depth
k	turbulence kinetic energy
k_{sgs}	sub-grid scale kinetic energy
KC	Keulegan-Carpenter number
n	porosity
p	subscript for particles
P	pressure
P_d	dynamic pressure
q	sediment transport rate
q_b	bed load sediment transport
r_p	particle radius
Re	Reynolds number
$\mathbf{Re}$	viscous stress tensor
Re_D	pile Reynolds number
Re_d	particle Reynolds number
Re_δ	bed boundary layer Reynolds number

s	specific gravity of sediment grains
S	equilibrium scour depth
$\mathbf{S}$	face normal vector
$\mathbf{S}_U$	momentum source
$\mathbf{S}_{imt}$	interphase momentum transfer
t	time
Δt	time step
T	time period of an oscillatory flow
T_s	time scale of the scour process
T_{ve}	volume exclusion term
T_w	wave period
$\mathbf{U}$	velocity
U_f	undisturbed bed shear velocity
$\mathbf{U}_f$	fluid phase velocity
$\mathbf{U}_p$	particle velocity
U_w	undisturbed orbital velocity
V_p	particle volume
x	abscissa
$\mathbf{x}$	position vector
$\mathbf{x}_p$	particle position vector
y	vertical coordinate
z	transverse coordinate
α_τ	amplification factor
α	volume fraction of water
δ	bed boundary layer thickness
ε	turbulence dissipation
ζ	water surface elevation
η	Kolmogorov scale

θ	Shields parameter
θ_{cr}	critical Shields parameter
θ_{cs}	critical solid volume fraction
θ_f	fluid volume fraction
θ_s	solid volume fraction
κ	Von Karman constant
λ	fraction factor
μ	dynamic viscosity
μ_0	intrinsic viscosity
μ_f	fluid viscosity
μ'_f	modified fluid viscosity
ν	kinematic viscosity
ν_t	eddy viscosity
ρ	density
ρ_f	fluid phase density
ρ_p	particle density
τ	bed shear stress
τ_p	inter-particle stress
τ_∞	undisturbed bed shear stress
τ^s_{ij}	subgrid-scale stress
ϕ	particle distribution function
ω	specific dissipation rate
ω_s	particle fall velocity

Acknowledgements

I would like to thank Dr. M. Li, of School of Engineering, The University of Liverpool, for teaching me coastal engineering and scientific writing, and for invoking my scientific scepticism. I would like to thank Dr. J. M. Harris, of HR Wallingford, for teaching me knowledge of scour and scientific writing, and nurturing my enthusiasm for research. I have been particularly privileged to have both as my supervisors, who provide me with invaluable advice and guidance, generous support and patient mentoring throughout my Ph.D. study. I would like to thank Dr. S. Ilic, of Lancaster Environment Centre, Lancaster University, and Dr. J. Zhou, of School of Engineering, The University of Liverpool, for agreeing to be my examiners and for their valuable time, detailed attention and invaluable advice given to the thesis. I would like to thank Prof. X. Chen, of Ocean University of China, for teaching me Physical Oceanography, and for his care, patient mentoring, and invaluable support and guidance. I would like to thank Prof. P. D. Thorne and Dr. J. Wolf of National Oceanography Centre for teaching me sediment transport and Physical Oceanography, and for the fruitful discussions and guidance. I would like to thank Dr. D. M. Kelly of HR Wallingford for his initial input into this work, and his patient teaching and guidance. I would like to thank Dr. J. R. Finn, of School of Engineering, The University of Liverpool, for his insightful advice, stimulating discussions, and inspiring suggestions. I would also like to thank Dr. J. Nicholson, of School of Engineering, The University of Liverpool, for his encouragement and inspiration over the small talks on the corridor. In memory of him. I am also very grateful to the financial support from Engineering and Physical Sciences Research

Council (EPSRC U.K.) and HR Wallingford. Finally, I thank my parents and my grandmother for their wholehearted support of my study.

Abstract

Numerical modelling of scour around offshore structures is still a challenging research topic for engineers and scientists due to the complex flow-structure-seabed interactions. In comparison to single-phase models and Eulerian models with Exner equation, a multiphase approach has advantages in interpreting the flow-particle and particle-particle interactions. In the present study, an Euler-Lagrange multiphase approach is adopted to develop a new scour model in order to simulate the air-water-sediment interplay simultaneously while being computationally efficient. The model is able to represent free-surface flow with a mobile bed, which is often critical for realistic scour modelling. Based on the open source computational fluid dynamics (CFD) software package OpenFOAM®, the model solves the Navier-Stokes equations on an Eulerian computational grid. The sediment particles are traced using the multiphase particle-in-cell (MP-PIC) method in a Lagrangian approach. The drag force from the fluid, body forces and inter-particle stresses as well as the interphase momentum transfer are all accounted for in the model. The model system is calibrated using several simple test cases, including a falling particle and steady flow passing isolated blocks, to identify optimal parameters for model operation. The model is then validated against available experimental data on a steady current around a vertical cylinder and sand suspension under oscillatory sheet flow, amongst other tests, with satisfactory agreement. Application of the model against laboratory experiments includes benchmark scour

cases underneath a horizontal pipeline under currents and waves, respectively. The tunnel erosion and lee-wake erosion stages are captured well by the model. The scour prediction matches with the measurements. In addition, the onset of scour is reproduced vigorously without any additional numerical assumptions or approximations. The model's capability to resolve the scour process and reveal the mechanisms involved is presented well.

Chapter 1

Introduction

1.1 Initiation of the Study

Scour has long been recognised as a severe safety hazard to the structures constructed in the fluvial and marine environment. Scour is used to distinguish the sediment transport process caused by the presence of a structure from the more general term "erosion"[80]. Scour at bridge piers, for example, has been studied extensively in the past several decades[8, 23, 36, 38, 52, 59]. Studies on scour in the marine environment did not gain as much attention until three or four decades ago when the construction of offshore structures became common, and consequently the geotechnical guidelines towards scour hazard assessment and scour protection

measures were in urgent needs. In engineering practice, the costs of the scour protections or remedial measures are often significant, especially in coastal or offshore projects. As indicated by Whitehouse et al.[92], the scour depth at offshore wind farm monopile foundations can be as large as 1.38 times the monopile diameter. More recently, Harris and Whitehouse[21] noted that the scour depth has been observed up to 2.4 times the monopile diameter, depending on the site conditions. At some sites where scour protections are installed, the edge scour or secondary scour around the protection can cause even deeper scour than the unprotected ones[92]. For instance, the scour protection at Scroby Sands off the east coast of England, has caused unintended expansive secondary scour. Therefore, it is still a challenging and urgent task to better understand the scour process and develop better prediction tools to minimise the risks associated with scour at the offshore structures.

Scour processes in the marine environment are also far more complex under combined waves and currents than those in rivers under currents. The time-varying nature of the sea, the complexity of the seabed formation, and the presence of structures on the seabed all contribute to the difficulties of scour study in the marine environment. For example, the flow dynamics around a structure under currents, waves, or combined waves and currents are still not fully understood, including the amplification of the bed shear stress around the structure and in the ambient flow, the flow separation position with respect to different shape, size, and orientation of the structure etc. The generation and dissipation of turbulence around the structure and in the lee-wake region are also quite challenging, which are often critical to the sediment dynamics and the ultimate scour pattern. Furthermore, the influences of the hydrodynamics and turbulence on the sediment pick-up from the bed and the subsequent suspension in the water column

are yet to be implemented in the commonly used prediction tools. The mechanics of the overall scour process from the initiation to the equilibrium status has not been properly reflected in existing scour models due to the limitation in the assumptions and approximations when resolving the sediment dynamics and its interaction with the flow dynamics.

To tackle these challenges, different approaches have been employed, including in-situ measurements, physical modelling (laboratory based) and computer modelling. Various numerical modelling approaches can be found in the literature, including the single phase mixture approach, the Eulerian type approaches, and the multiphase approaches. Works based on the potential flow theory were carried out at the early stage[41, 43, 50]. However, with the many assumptions and ad-hoc parametrisations, these models often fail to produce the whole picture of the sediment transport and scour process. Later on, Eulerian models with Exner equation were developed to study scour problems with the aid of mesh deformation or dynamic mesh method to resolve the bed. Due to the limitation in resolving the flow-sediment interactions, the pick-up of the sediment particles from the bed and the flow-bed interactions rely on many empirical relations that lead to many uncertainties in the results. Furthermore, mesh deformation and dynamic mesh method require special and careful treatment to prevent mesh distortion and maintain the mesh quality. Therefore, such models usually struggle to resolve the rapid changing bed profile and often fail to resolve the shape of the scour hole and the eroded bed profile correctly, especially where large steepness is observed. Lately, the multiphase approach is gaining in popularity due to its capability to better interpret the flow-sediment and sediment-sediment interactions. However, in such multiphase approach models, usually only the water and sediment are considered, and the free surface effect is rarely represented. It not only limits the application of

such models, but also implicates inaccuracy in the scour prediction as the free surface effect is often critical for realistic scour processes especially those under waves or combined waves and currents. Therefore, incorporating the free surface effect to achieve a better and more reliable scour prediction is one of the motivations of the present work.

In multiphase approaches, the flow is often referred to as the fluid phase, and the sediment is named the solid phase. According to the treatment of each phase, one of the following methods are usually employed: Euler-Euler methods, Euler-Lagrange methods and Lagrangian methods. In Euler-Euler models, both the fluid phase and the solid phase are regarded as continuum, thus, the fluid-particle interactions cannot be resolved directly due to the continuum assumption of the solid phase, and instead they must be addressed explicitly with parameterisations. Moreover, Eulerian models are typically based on cell-averaged quantities, therefore, they often struggle to model complex deformation and interface fragmentation. By contrast, in Lagrangian models, such as the Smoothed Particle Hydrodynamics method (SPH) and the Moving Particle Semi-implicit method (MPS), the inherent discrete-particle property of sediment is well represented. However, as the most well-known drawback, Lagrangian models are particularly demanding on computational resources. Moreover, the incorrect pressure approximation caused by a spurious pressure fluctuation is a common problem associated with the sharp fluid interfaces in such models.

Drawing on the advantages of these two types of models, Euler-Lagrange type models provide an attractive alternative. In such models, the fluid phase is treated as continuum on an Eulerian grid, and the solid phase is treated as discrete particles. Therefore, the inherent properties of each phase are well represented, and the

interaction between the phases can be resolved straightforwardly. It is also computationally efficient compared to Lagrangian models. Therefore, Euler-Lagrange models can be a powerful tool to resolve the physics and reveal the mechanics involved in scour processes. However, the coupling of the Eulerian grid and the Lagrangian framework, the incorporation of the free surface, the treatment of the solid phase in flows ranging from very diluted to hyper-concentrated, among others, are all challenging tasks, and consequently hinder their application in scour studies. Considering the outstanding advantages of such models to possibly resolve the scour mechanics and improve scour prediction, this work is therefore motivated to develop a novel scour model using the Euler-Lagrange multiphase approach to study the scour process around offshore structures with the free surface effect.

1.2 Aims and Objectives

1.2.1 Aims

The present work has the following two aims:

1. To develop a novel numerical tool based on the Euler-Lagrange multiphase approach for reliable scour prediction around offshore structures;
2. To improve the understanding of the scour process and reveal the details of sediment dynamics involved in the process based on the modelling results.

1.2.2 Objectives

The specific research objectives include:

1. To develop an Euler-Lagrange multiphase approach to resolve the dynamics of the flow field and the bed evolution simultaneously during the scour process;
2. To develop a particle based approach to represent the sediment dynamics and the sediment-flow interactions in particulate flow ranging from very dilute to hyper-concentrated flow, as well as a fully packed bed;
3. To perform scour prediction around offshore structures under different hydrodynamic conditions and resolve the detailed processes using the new model;
4. To examine the impact of turbulence characteristics on the scour process;
5. To examine the mechanics of scour development from the initiation to the later stages.

Based on these aims and objectives, the present work also aims to answer several fundamental questions regarding the scour process and its numerical modelling:

1. How can the free surface effect and a mobile sandy bed be simulated simultaneously with the flow dynamics in a computational fluid dynamics (CFD) model?

2. How can the flow-sediment interactions be represented effectively in a CFD model?

3. How does the particle motion initiate in the scour process?

4. How does the flow structure, especially the turbulence characteristics, affect the scour pattern?

5. How does the particle motion affect the overall scour process?

In particular, the current study will focus on the scour processes around horizontal pipelines on the seabed because of its important implications in engineering practice and the challenges involved in the numerical modelling.

1.3 Contents

An Euler-Lagrange multiphase approach is adopted in the present study to develop a new particle based scour model in order to simulate air-water-sediment three-phase interplay simultaneously and to reveal the scour mechanism. The model is able to represent free-surface flow over a mobile bed, to eliminate the inaccuracy caused by the rigid lid assumption. Based on the open source CFD software package OpenFOAM®, the model solves the Navier-Stokes equations on an Eulerian computational gird. The sediment particles are traced using the multiphase particle-in-cell (MP-PIC) method in a Lagrangian framework. The flow and sediment particles are fully coupled, and particle-particle interaction is also resolved in the model.

In this work, a detailed literature review is presented in Chapter 2. Chapter 3 describes the theories involved in the numerical model. The model calibration is presented in Chapter 4. Then the results of the model application are presented in Chapter 5. Discussion, conclusion and future work are outlined in Chapter 6.

Chapter 2

Literature Review

2.1 Introduction

In this chapter, the physical processes involved in the scour process, including the flow regime, sediment transport and scouring, will be reviewed first. Then the review on the numerical modelling approaches concerning the hydrodynamics, including the turbulence modelling, and sediment transport and scour, including the treatment of the solid phase in the multiphase approaches, will be presented in sequence.

2.2 Scour at Offshore Structures

The presence of structures in the marine environment will change the flow patterns, turbulence properties, and local sediment transport in its immediate neighbourhood, resulting in local scour and further influence on the global scour pattern. Several phenomena are usually identified, such as flow contraction, a horseshoe vortex in the upstream side, lee-wake vortices and/or vortex shedding in the downstream side, turbulence enhancement, wave reflection, diffraction and breaking etc.[80]. These changes in the flow field can amplify the local bed shear stress and enhance sediment transport capacity, which leads to a divergence of sediment transport rate and ultimately the occurrence of scour.

Conventionally, scour is classified according to different criteria. These terms below are usually used in scour studies.

- Local scour and global scour. For example, in the case of a multi-leg jacket structure, the scour pits around each single piles are referred to as local scour; the saucer-shaped depression beneath and around the whole installation is called the global scour.

- Clear-water scour and live-bed scour. If the Shields parameter θ (Eq. 2.1) is lower than its critical value θ_{cr}, which means that there is no sediment transport in the far area, it is called the clear-water scour; otherwise, when sediment transport is prevailing in the whole area ($\theta > \theta_{cr}$), live-bed scour is taking place. The Shields parameter is given by

$$\theta = \frac{U_f^2}{g(s-1)d}, \tag{2.1}$$

where g is the gravitational acceleration, s is the specific gravity of sediment grains, d is the grain size, and U_f is the undisturbed bed shear velocity expressed by $U_f = \sqrt{\frac{\tau_\infty}{\rho}}$, and τ_∞ is the bed shear stress for the undisturbed flow. The critical value of the Shields number is a function of the grain Reynolds number.

2.2.1 Flow Pattern

Despite of the undisturbed flow regime, the flow pattern in the scour process largely depends on the shape and size of the structure presented in the flow. Vertical piles and horizontal pipelines are very common structures in the marine environment. In terms of piles, Sumer and Fredsøe[80] categorise it into two flow regimes: the slender-pile regime where the pile diameter D is small compared with the wave length L, and otherwise the large-pile regime. The distinguished feature of the former regime is the flow separation with the presence of separation vortices, which applies to the flow around offshore structures like monopiles in the offshore wind farms, while the flow in the latter regime is unseparated.

Flow around a Slender Pile

A schematic sketch of the slender pile regime is shown in Figure 2.1. When flow is approaching the pile, the flow structure in the bed boundary layer will be affected immediately. Induced by the adverse pressure gradient upstream of the pile, the bed boundary layer separates and a separation line is formed. The separated boundary layer further generates a horseshoe vortex at the upstream side. In the case of a steady current, Baker[4] indicates that the ratio of the bed boundary layer thickness δ to the pile diameter D, i.e., $\frac{\delta}{D}$, the pile Reynolds number $Re_D = \frac{UD}{\nu}$, the bed boundary layer Reynolds number $Re_\delta = \frac{U\delta}{\nu}$, and the pile geometry (shape and size, etc.) are the main parameters to evaluate a horseshoe vortex. The larger $\frac{\delta}{D}$, Re_D, and Re_δ are, respectively, the larger the vortex length x_s will be. The cross-sectional shape of pile also influences horseshoe vortex by its impact on the adverse pressure gradient. Generally speaking, it is more difficult for a streamlined cross-sectional shape to induce large horseshoe vortex. Sumer et al.[77] studied the impact of square-shaped (90° orientation), circular-shaped and square-shaped (45° orientation) cross-sectional piles and found out that the square pile with 90° orientation was the easiest one to generate longer x_s. With respect to pile height, the larger $\frac{L}{H}$ (L is the cross-flow dimension of the pile and H is the pile height) is, the smaller vortices are generated.

Regarding the horseshoe vortex generated under waves, the Keulegan-Carpenter number KC is another important parameter in addition to those aforementioned parameters in steady flow. It is given by

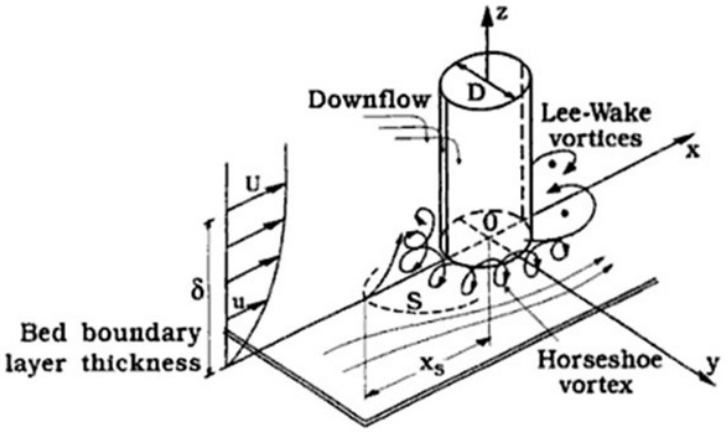

FIGURE 2.1: Sketch of the flow pattern around a vertical pile. S refers to the separation line. (After Sumer and Fredsøe[80].)

$$KC = \frac{U_m T_w}{D} \tag{2.2}$$

where U_m is the maximum value of the undisturbed orbital velocity at the bed and T_w is the wave period. It is difficult for the horseshoe vortex to form if KC number is very small; and if KC number is large, the horseshoe vortex is supposed to behave almost in the same way as in the circumstances of steady flows. Sumer et al.[77] studied the horseshoe vortex under waves with different KC numbers and revealed the impact of KC number on horseshoe vortex by exploring the adverse pressure gradient using the potential flow theory. Their experimental results show that a KC number smaller than 6 will suppress the boundary layer separation in front of a circular pile. In the case of a square pile with 90° orientation, horseshoe vortex comes into being with the threshold KC value of 4. Sumer et al.[77] also indicate that the life span of a horseshoe vortex is longer with a larger KC number and in the case of a less streamlined pile (e.g. a square pile).

In the case of waves with a superimposed current, a horseshoe vortex comes into being more easily. Only a small KC number is required, and the separation distance increases remarkably compared to a case with waves only.

Bed shear stress beneath the horseshoe vortex is an important parameter associated with the scour process. The value of the bed shear stress compared to its undisturbed value is mainly determined by the strength of the horseshoe vortex, and it generally peaks at the side edge of the pile. The study by Baker[4] on laminar flows indicates that with the presence of a horseshoe vortex, the bed shear stress can be amplified by a factor of $5 - 11$ compared to the undisturbed conditions. The study by Hjorth[27] shows that the amplification factor under the combined action of the horseshoe vortex and the flow contraction effect can be as large as 11 at the midway between the front and side edges of the slender pile, which in consequence will lead to dramatically enhanced sediment transport capacity and scour development around the pile. Under waves, the amplification factor of the bed shear stress is found to be a function of KC number, and the bed shear stress increases as KC number increases. Sumer et al.[77] indicate that the transition of a laminar horseshoe vortex into the turbulence regime is dependent on KC number as well as $\frac{\delta}{D}$ and Re_D. In the experiments by Sumer et al.[77], the transition occurred when KC number was between 10 and 20.

The lee-wake vortices are formed at the downstream side of the pile. In steady currents, the lee-wake flow is mainly determined by Re_D and the pile geometry, while under waves, the KC number is a more dominant parameter. Sumer and Fredsøe[84] and Sumer et al.[77] point out that compared to steady-current case, the lee-wake vortex flow is a more essential component for the scour development under waves.

Flow around a Pipeline

Apart from vertical piles, the scour around horizontal pipelines on the seabed has also been studied extensively in the past. The flow around a pipeline is relatively simpler than that around a vertical pile. The seepage flow underneath the pipe and the lee-wake effect are the most predominant features. Driven by the pressure difference between the upstream and downstream side of the pipe, a seepage flow will take place underneath the pipeline. It acts as the agitating force on the sand, and when it exceeds the submerged weight of sand, piping will occur. Sumer et al.[85] measured the pressure gradient around pipelines in a steady current and it is found to be increasing with an increasing flow velocity. Sumer et al.[85] also derived the critical condition of the pressure gradient for piping to occur. Their study indicates that the excessive seepage flow and the resulting piping are the major mechanisms to induce onset of scour, which is the initial stage of scour development around a pipe.

In the case of waves, Sumer et al.[85] measured the surface elevation and the pressure gradient underneath the pipe. The measurements show that there is a $20 - 25^{\circ}$ phase lag in the pressure gradient compared to the surface elevation. In addition, the pressure gradient large enough for piping to occur is only available for a short time during each crest half period. Only after several such exposures, piping takes place.

In addition to the seepage flow, the lee-wake effect also plays an important role. Sumer and Fredsøe[78] investigated the scour development below a pipeline and

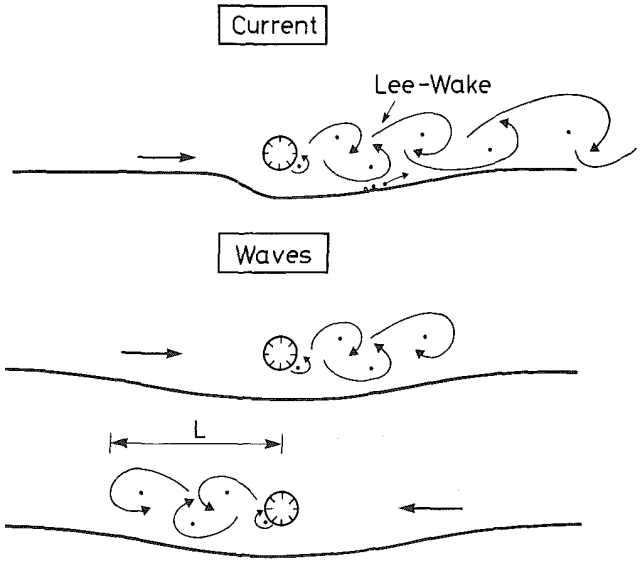

FIGURE 2.2: Sketch of the lee wake effect under waves. (After Sumer and Fredsøe[78].)

found that the lee-wake effect is the key mechanism in this process. Figure 2.2 was depicted by Sumer and Fredsøe[78] to show the difference of the lee-wake effect under steady currents and waves respectively. They summarise that the upstream side of the pipe under a steady current is dominated by potential flow whereas flow separation and a vortex street, which is formed by the lee-wake vortices, are observed at the downstream side. Under waves, the lee-wake vortices are observed at both side of the pipe due to flow reversal during wave cycles as shown in Figure 2.2[78]. They point out that the extension of the lee-wake vortex street L_v under waves is governed by the KC number, and a linear relation is developed by them according to the flow visualisation study by Jensen and Jensen[31] that $\frac{L_v}{D} = 0.3KC$[78].

2.2.2 Sediment Transport

According to the transport mechanism of bed materials, two mechanisms are identified, namely the suspended load and the bed load. The bed load has continuous contact with the bed, of which the particles roll, slide or saltate along the bed. Its transport is almost totally determined by the effective bed shear stress. When the bed shear velocity just becomes larger than the critical value for the initiation of motion, the particles will roll and slide, and saltate if the bed shear velocity continues increasing along the bed, in the regime of bed load transport. Once the value of the bed shear velocity exceeds the fall velocity of the particles, they will become suspended in the flow and transfer into the suspended load mode. The total sum of the bed load and the suspended load is named the total sediment load.

The Shields number (Eq. 2.1) is an indicator of the initiation of motion for sediment particles. The sediment particles will move once the Shields number θ exceeds its critical value θ_{cr}, which is given by,

$$\theta_{cr} = \frac{U_{fc}^2}{g(s-1)d}, \tag{2.3}$$

where U_{fc} is the critical value of the bed shear velocity.

With the presence of structures, the entrainment of bed materials, the transport capacity of both the suspended load and the bed load are enhanced due to the enhanced bed shear stress and stronger turbulence level around the structures. The amplification factor α_τ is used to measure the increase in the bed shear stress, which is given by

$$\alpha_\tau = \frac{\tau}{\tau_\infty}, \tag{2.4}$$

where τ is the enhanced bed shear stress and τ_∞ is that for the undisturbed flow. Certain amount of knowledge about the enhanced bed shear stress has been accumulated, some of which are already reviewed in Section 2.2.1. Sumer and Fredsøe[80] adopted a formula $q_b \sim \tau^{3/2}$ in the discussion of the bed load sediment transport due to bed shear stress. Although this formula is not strictly derived, it demonstrates the importance of the bed shear stress to bed load transport. However, there is still little knowledge on the enhanced turbulence level in the vicinity of the structure as well as its contribution to the sediment transport and scour processes.

2.2.3 Scour Process

With the presence of structures, the amplification factor α_τ is larger than 1 locally, and the increased sediment transport capacity will result in the erosion of the

bed. The scour process continues until $\alpha_\tau = O(1)$ around the structures when the equilibrium stage is reached. The scour depth at that moment is called the equilibrium scour depth. The time required for the scour development is called the time scale of the scour process. Sumer and Fredsøe[80] adopt a formula to represent the time variation of the scour depth,

$$S_t = S(1 - exp(-\frac{t}{T_s})), \tag{2.5}$$

where S is the equilibrium scour depth and T_s is the time scale of the scour process.

In the case of steady currents, Sumer and Fredsøe[80] point out that the scour depth is influenced by such factors as the Shields number, the sediment gradation, $\frac{d}{D}$, $\frac{\delta}{D}$, the cross-sectional shape and the alignment factor. Regarding the scour under waves, the study by Sumer et al.[81] indicates that the KC number is the main parameter governing the scour development on a live bed. In terms of the scour development in combined wave and currents, Sumer and Fredsøe[79] obtained an empirical expression concerning the scour depth in live bed regime from experiments with $KC < 30$, which is given by

$$\frac{S}{D} = \frac{S_c}{D}[1 - exp(-A(KC - B))], \quad KC \geq 4, \tag{2.6}$$

where S_c is the scour depth in steady current alone, and the coefficients A and B are given by

$$A = 0.03 + \frac{3}{4}U_{cw}^{2.6}, \tag{2.7}$$

$$B = 6^{-4.7U_{cw}}, \tag{2.8}$$

where $U_{cw} = \frac{U_c}{U_c+U_m}$, and U_c is the current velocity and U_m is the maximum value of the undisturbed orbital velocity at the bed.

Scour underneath Pipelines

In the scour processes underneath pipelines, three stages are usually identified: onset of scour, tunnel erosion, and the lee-wake erosion stage. Other three-dimensional processes like the self-burial and backfilling process along the free span areas and at span shoulders have also been summarised by Sumer and Fredsøe[80].

Previous studies show that the onset of scour is basically related to the seepage flow in the bed underneath the pipeline, which is caused by the pressure difference between the upstream and downstream sides of the pipeline[50, 80]. Sumer and Fredsøe[79] studied the onset of scour in both currents and waves by measuring the

pressure gradient underneath the pipeline, and found that onset of scour is largely caused by the pressure-gradient driven seepage flow and the resulting piping. A criterion for onset of scour is given in the study by Sumer and Fredsøe[79] as follows,

$$\left[\frac{U^2}{gD(1-n)(s-1)}\right]_{cr} \geq f(\frac{e}{D}), \tag{2.9}$$

where U is the undisturbed flow velocity at the top of the pipeline, D is the pipeline diameter, n is the porosity, s is the specific gravity of sand, e is the burial depth, and the function f on the r.h.s. is determined by experiments. This non-dimensional form is derived from the following equation, which means that the critical condition occurs when the pressure gradient $\frac{\partial}{\partial x}(\frac{p}{\gamma})$ outweighs the floatation gradient $(s-1)(1-n)$[79]:

$$\frac{\partial}{\partial x}(\frac{p}{\gamma}) \geq (s-1)(1-n), \tag{2.10}$$

where γ is the specific weight of water.

When a breach is formed underneath the pipe and it gradually develops into a very narrow tunnel, the tunnel erosion stage starts. At this stage, the gap between the bed and the pipeline is still very small compared to the pipeline diameter D.

However, a considerable amount of water can be diverted through this pathway towards the downstream side. As the velocity is large in the gap, and the shear stress can be increased dramatically, and in consequence the sediment transport there is enhanced considerably. Therefore, at this stage, the scour underneath the pipe develops substantially and the gap between the bed and the pipeline is increased fairly quickly. As the gap becomes larger, the flow velocity in the gap will slow down and this intense scour process will slow down as well. When the gap reaches a certain depth, the tunnel erosion stage will be followed by lee-wake erosion, where the bed downstream of the pipe being eroded by the lee-wake vortices becomes the most prominent feature. Sumer and Fredsøe[80] and Sumer et al.[83] point out that although the organised wake flow, which is formed by the agglomeration of separation vortices shed and convected steadily downstream, takes control of the scour process at this stage, vortex shedding happens from a very early stage. This process continues until the equilibrium stage is reached where the bed shear stress underneath the pipeline stays constant and equals to the undisturbed value, i.e., $\tau = \tau_\infty$; or in other words by Sumer and Fredsøe[78], it happens when the sediment transport just below the pipe equals to that far from the pipe.

Sumer and Fredsøe[78] point out that the scour profile under a steady current is featured by a steep upstream slope and a gentle downstream slope due to the different local flow pattern. The upstream side is dominated by a potential flow whereas the downstream side is featured by a vortex street over a long stretch. Sumer and Fredsøe[78] also clarify that the downstream side is eroded more heavily due to the higher turbulence level and higher instantaneous velocity. Sumer et al.[82] found out via experiments that the instantaneous velocity of the downstream vortices can be larger than the undisturbed velocity by a factor of 2 or more. Regarding the scour process under waves, Sumer et al.[85] found that onset

of scour happens almost at the same time as the passage of a wave crest. The breakthrough under waves is a more progressive process due to the oscillatory nature of the flow. As reviewed in Section 2.2.1, the extent of the lee-wake vortex street is dependent on the KC number, Sumer and Fredsøe[78] indicate that the larger the KC number is, the longer the streamwise extent of the bed is affected by the lee-wake vortices during one half-period of the wave cycle. Again due to the oscillatory nature of waves, the gentle slope being eroded by the lee-wake vortices happens at both sides of the pipe.

2.3 Hydrodynamic Modelling

A reliable prediction of the hydrodynamics is a prerequisite of a well-functioning scour model. Two dimensional scour models can give quick assessment of the scour patterns and predict the maximum scour depth relatively accurately[47]. They are usually based on the water-depth-averaged shallow water equations (SWEs) and sediment transport equations. For a better interpretation of the three dimensional processes, CFD models solve the three-dimensional Navier-Stokes equations directly, describing the three-dimensional nature of the scouring process without any hypotheses. Compared to the shallow water modelling, obviously, CFD models are more capable of capturing the complex hydrodynamics around structures and resolving the full three-dimensional features.

2.3.1 Shallow Water Modelling

Although it cannot resolve the detailed development of the flow pattern, turbulence structures or scour characteristics, two dimensional models have their advantages in giving quick assessment of the main scour parameters with relatively sufficient accuracy and they are less demanding on computational resources.

The shallow water equations have been employed in most two dimensional models to simulate the hydrodynamics. With the hydrostatic assumption and the assumption of constant velocity over the water depth, no pressure term is included in the shallow water equations. Accuracy in second and higher order has been achieved with the finite volume methods[2, 96]. However, as its name suggests, shallow water modelling is only applicable to very limited range of scenarios where the horizontal length scale is much greater than the vertical length scale.

Liu et al.'s model[47] is a typical one using the shallow water modelling approach by coupling the shallow water equations with the sediment transport equation on an unstructured mesh. The Godunov scheme was employed to capture the steep water surface elevation gradient, which was split using the method proposed by Rogers et al.[68] and Rogers et al.[69] to obtain the hyperbolic formulation. The inviscid fluxes were solved by Roe's approach[66, 67], an approximate solver of Riemann problem. Hydrodynamic test of dam break flow in channels with a 90° bend was performed with fairly good prediction of the free surface compared to experimental data. When it comes to scour modelling, the hydrodynamic performance of the coupled model was reasonable as the free surface and the velocity field were

resolved well and a recirculation zone was captured in the results. However, due to the two-dimensional nature of the shallow water equations, three-dimensional features such as the horseshoe vortex cannot be resolved, which is a major drawback to the scour prediction. Moreover, it was problematic of Roe's approach to cope with dry-wet interfaces. In addition, scour process usually involves complex turbulence structures, but no turbulence model was employed in their model. There are many other shallow water approach based models, but the overall structure and method are similar to those in Liu et al.[47]. No further details are reviewed herein.

2.3.2 Computational Fluid Dynamics Modelling

Without the assumptions made in shallow water equations, the three-dimensional Navier-Stokes equations can be solved directly by CFD methods. In scour modelling, the free surface variations often need to be taken into account, such as the surface gradient induced secondary flow around a bend in open channels and free surface waves induced scour. However, in cases where the surface variation does not cause significant effects, the rigid lid method is often applied for simplicity. Currently, to resolve the free surface effect, the marker and cell method (MAC), the volume of fluid method (VOF)[26] and the level set method[72] are available in the literature. In the simulation of multiphase flow, the VOF method has been widely used. In particular, it has been employed in several scour studies[46, 65].

Zhao et al.[101] simulated the local scour around a submerged vertical cylinder

in steady currents using a three-dimensional finite element model. The Reynolds-Averaged Navier-Stokes equations (RANS) were solved by the Arbitrary Lagrangian Eulerian (ALE) scheme and the free surface effects are ignored by using a rigid lid approximation. They extended the Petrov-Galerkin finite element scheme to three-dimensional. The weighting function was modified to realise upwind, making the upstream value a computational node larger than the corresponding downstream value. It is noteworthy that they calculated a separate case of flow in a long straight channel (200D long), and used the velocity, sediment concentration and turbulent quantities at the outlet boundary as the input for the scour model. Standard wall function was employed in the bed boundary conditions for computational efficiency. The horseshoe vortex and vortex shedding were captured well by the model, no comparison with flow measurements was presented though. However, the predicted scour depth along the cylinder perimeter was 10% to 20% smaller than the measurements. Moreover, the bed shear stress enhancement was underestimated in the validation test. This could be probably caused by the rigid lid approximation, as well as the inappropriate treatment in the wall function, among other simplifications.

Zanganeh et al.[98] investigated current-induced live-bed scour beneath marine pipelines at tunnel erosion and early stages of lee-wake erosion. The flow was simulated with the Smoothed Particle Hydrodynamics (SPH) method in a Lagrangian two-phase model. They adopted the Sub-Particle Scale (SPS) model as the turbulence closure scheme for the flow. The hydrodynamic performance reached good agreement with experimental data in the upstream and downstream part of the pipe while the velocity around the pipe was under-estimated. It could be due to the inappropriate specified boundary conditions at the pipe surface.

Tofany et al.[88] studied numerically the influence of the breakwater steepness on the hydrodynamics under standing waves and the scour pattern in front of impermeable breakwaters. Their model solves the RANS equations closured by the $k-\varepsilon$ turbulence model for the hydrodynamics. The VOF method was employed to capture the free surface. The predicted near bottom velocity was in good agreement with the experimental data. However, an additional term of bottom shear stress had to be included in the momentum equation according to Karambas[32] such as to achieve a physically sensible scour pattern.

2.3.3 Turbulence Modelling

In scour process, as highlighted previously, the flow tends to be in high turbulence flow region. Vortex shedding and turbulence generation/dissipation are very important processes that often are deterministic to the final scour pattern. To accurately model the turbulence level is therefore a key factor in the hydrodynamic simulation. A variety of turbulence models are available to simulate the turbulence generation and dissipation processes for the flow field, including direct numerical simulation (DNS), large eddy simulation (LES) and Reynolds-averaged simulation (RAS).

Direct Numerical Simulation

Direct numerical simulation solves the Navier-Stokes equations directly after numerical discretisation without any averaging or approximation. It gives detailed information about the velocity and pressure among other variables of interest at numerous grid points. The results are so detailed that they can even be treated as equivalent to experimental data and can be adopted for statistical use. Moreover, DNS can control external variables like the wall roughness easily, while it may be very difficult or even impossible to accurately control some variables in the laboratory. Hence, it is a great tool to understand the physical mechanisms of turbulence production and dissipation.

However, this huge amount of information may be unnecessarily sufficient to coastal engineers, especially considering the large amount of effort needed in post-processing, let alone the very high expense of computational resources for the simulation. In order to capture all the significant structures in turbulence as well as all the kinetic energy dissipation, the computational domain is required to be no smaller than the physical prototype or the largest turbulent eddy, while the grid size must be no larger than a viscosity determined scale — Kolmogorov scale. Even in case of homogeneous isotropic turbulence, the cost of simulation scales as large as Re_l^3[15], where Re_l is the Reynolds number with respect to the velocity fluctuations and the integral scale l. Therefore, it is less applicable to high-Reynolds-number simulations. On top of that, the time-advance methods, the generation of the initial and boundary conditions, among other numerical issues are also challenging. Hence, its application in scour studies has hardly been conducted.

Large Eddy Simulation

Turbulent flows contain a wide range of eddies, and the large scale ones are more effective in the transport of conserved properties. It could be a sufficient solution to most turbulence simulations that the large scale eddies are resolved directly, and the less effective small scale eddies are simply parameterised. LES is based on this hypothesis. LES is three-dimensional and time dependent, producing detailed turbulence structures, and it is much less expensive than DNS. Hence, it is more suitable in situations where the Reynolds number is too high and the geometry is too complex for DNS.

The sub-grid scale (SGS) stress τ_{ij}^{s} is an important concept introduced in LES models for approximation, which is given by $\tau_{ij}^{s} = -(\overline{u_i u_j} - \overline{u}_i \overline{u}_j)$. It is the large scale momentum flux caused by the unresolved scales. It contains information about local averages of the small scale field. There are several SGS modelling concepts, based on which several LES models are developed such as Smagorinsky models, dynamic models and deconvolution models.

LES models require less computational resources than DNS, and it can reproduce a desirable amount of turbulence information. Although its application in coastal engineering field is still at its early stage due to the limited computational resources and numerical techniques, with its outstanding advantage and the rapid progress in the computational technologies, the application of LES in scour studies has started emerging in recent years. In particular, Li and Cheng[42] indicate that LES is suitable for the vortex shedding flow around a horizontal cylinder based on

their own research and that of others[7, 43].

Nguyen and Wells[54] studied the bedform development under turbulent flow using a coupled LES and Immersed Boundary Method (IBM) to resolve the three-dimensional flow field. The SGS stress was computed using the shear-improved Smagorinsky eddy viscosity model by Leveque et al.[40]. The computed shear stress distribution over a sinusoidal bed surface was compared to DNS results with fairly good agreement. The mean flow fields including the streamwise velocity, the vertical velocity, the turbulence kinetic energy and the Reynolds stress all agree well with the DNS results.

Kim et al.[35] studied the local scour at two adjacent cylinders under clear-water scour conditions using a combined hydrodynamic-sediment-trasnport-morphodynamic model. The three-dimensional hydrodynamics was resolved using LES with a Smagorinsky sub-grid model combined with IBM. The time-averaged velocities and turbulence intensities in the flow through two vertical cylinders agreed well with the experimental data, even in front of and behind the cylinders. The velocity spike near the bed behind the cylinder due to the high momentum flux resulted from the transfer of vortices into the wake region was captured by their LES model. The relatively high turbulence intensity behind the cylinder due to vortex shedding was also resolved. In their study, Kim et al.[35] also indicate that the presence of the cylinders are the principal source of turbulence rather than the bed friction. The good agreement demonstrates the strength of LES in dealing with scour process in which complex turbulence dominates the flow dynamics.

Reynolds-Averaged Simulation

Even less demanding on the computational resources, in RAS models, variables in a statistically steady flow can be expressed as the sum of a time-averaged quantity and a fluctuation. The eddy viscosity ν_t is introduced to represent the unresolved scales. Different models have been developed to compute ν_t, including the $k-\varepsilon$ model, $k-\omega$ model, and $k-\omega$ SST model.

$k-\varepsilon$ Model

The $k-\varepsilon$ model has been adopted for turbulence modelling in a number of sediment transport and scour models[19, 46, 88, 93, 99, 100, 103]. A number of damping functions have been developed for various applications with the $k-\varepsilon$ models so far, and results agree well with DNS data. The $k-\varepsilon$ models are proven to be suitable for flows with small pressure gradients, such as free-shear layer flows, wall-bounded and internal flows where the mean pressure gradients are small[6].

Liu and Garcia[46] studied wall jet scour using the $k-\varepsilon$ model as the turbulence closure. The strong jet-induced recirculation behind the sluice gate, small isolated circulation areas, and the circulation zone inside the scour hole were all captured well by their model. The momentum diffusion along the abscissa direction was resolved as well. The horizontal velocity along the abscissa agreed well with the experimental data, whereas the velocity far downstream of the jet inlet was underestimated by their model.

However, in flows with large adverse pressure gradients, the performance of $k-\varepsilon$ models is declining. It was also commented by Liu and Garcia[46] that two equations models such as $k-\varepsilon$ models can become unstable when simulating wave driven orbital motions, especially when the wave is strong or where wave breaking takes place. Mayer and Madsen[51] performed analytical stability analysis of the $k-\varepsilon$ model under waves, and found out that the turbulent eddy viscosity became unbounded. Hence, they proposed a modified two-equation model for waves, whereas most models rely on the tuning of the empirical parameters[46] when using the $k-\varepsilon$ model.

$k-\omega$ Model

The $k-\omega$ model is also a popular choice, especially in the sublayer of the boundary layer[53]. Different from the $k-\varepsilon$ model, $k-\omega$ model does not implicate damping functions, and simple Dirichlet boundary conditions can be specified[53]. With its accuracy in predicting the mean flow profiles as well as its numerical stability, the $k-\omega$ model has also been widely adopted[16, 34]. Moreover, $k-\omega$ model produces better results in the logarithmic part of the boundary layer than $k-\varepsilon$ model in adverse pressure gradient flows as reported in the literature.

$k-\omega$ SST Model

On the basis of the original $k-\omega$ model, Menter[53] proposed two new eddy-viscosity turbulence models: the baseline (BSL) model and $k-\omega$ shear stress transport (SST) model. The former switches between $k-\omega$ model in the boundary

layers and $k-\varepsilon$ model in the outer regions to avoid the strong free stream sensitivity of the original $k-\omega$ model. The latter modifies the definition of the eddy-viscosity in the BSL model to represent the effect of the transport of the principal turbulent shear stress and remarkably improves the modelling results in adverse pressure gradient flows as found out by Menter[53] and Zhao et al.[101].

Due to its good performance in flows with strong adverse pressure gradient, the $k-\omega$ SST Model has been a popular choice for scour models[10, 101, 102, 104]. Zhao et al.[101] studied the local scour around a submerged vertical cylinder in steady currents with the $k-\omega$ SST turbulence closure model. The modelled pressure distribution upstream of the pile along the stagnation line and along the abscissa respectively agreed well with the experimental data. The time-averaged bed shear stress distribution along the symmetry line upstream of the pile was also reproduced well, the bed shear stress very close to the pile was underestimated though.

2.4 Sediment Transport and Scour Modelling

Like the modelling of hydrodynamics and turbulence, the prediction of sediment transport and scour processes are also dealt with by various approaches depending on the focus of the individual work as well as the available numerical methods at the time, which now can be largely divided into single phase and multiphase approach. Works based on the potential flow theory were carried out at the early

stage[41, 43, 50]. However, with the massive assumptions and ad-hoc parameterisations, these models often fail to produce the whole picture of the sediment transport and scour process; only certain aspects of the problem, such as scour depth at the upstream side, can be predicted reasonably. Later on, the Eulerian approach with Exner equation type models emerged. In such models, the governing equations of flow and sediment transport equations are solved on an Eulerian grid, and the sediment continuity equation, i.e., Exner equation, is used to resolve the bed elevation. Such models are capable of resolving the scour process with more detailed calculation compared to the single-phase models. However, empirical or semi-empirical formulas are still indispensable in such models, and the mesh deformation or dynamic mesh approach used to resolve the bed elevation is a major difficulty. Therefore, such models often struggle to resolve the rapidly changing bed profile, the maximum scour depth is usually underestimated, and the bed profile is much milder due to the limitation of mesh deformation. Deterministic models and stochastic models have also been used for scour prediction. However, the former usually involves many uncertainties because of the empirical nature; and the latter usually requires a large amount of data prior to model development, and a number of assumptions have to be made to determine particle motion as the forces are usually not calculated directly. In recent years, the multiphase approach is gaining in popularity due to its capability to better interpret the flow-sediment and sediment-sediment interactions. In multiphase approach, the mesh deformation is no longer necessary to resolve the bed. According to the treatment of each phase (solid phase and fluid phase), one of the following methods are usually employed: Euler-Euler methods, Euler-Lagrange methods and Lagrangian methods.

In multiphase approaches, the coupling between the the solid phase and fluid phase is a major concern for sediment transport and scour processes. The volume

fraction of the solid phase θ_s and the mass loading ϕ_m, which is the mass ratio of the solid phase to the fluid phase, are the two determinant parameters with respect to the interaction level between the two phases[5]. When θ_s and ϕ_m are small, only the influence of the fluid phase on the solid phase is predominant, thus one-way coupling is sufficient. When the mass is comparable between the two phases, the influence of the solid phase back on the fluid cannot be neglected, two-way coupling is therefore needed. If the volume fraction of the solid phase increases to a critical value, the particle-particle interactions such as inter-particle stress and collision become more notable and thus four-way coupling is required.

2.4.1 Single-phase Model

Single-phase models are usually based on the potential flow theory and viscosity/turbulence closure models. They are able to predict the maximum scour depth and the upstream session of the scour hole, yet their prediction ability of the scour profile are largely restricted. Moreover, although some fluid-particle interaction effects can be considered by the addition of an extra production term in the turbulence model equations, single-phase models are usually not capable to account for the particle-particle interaction.

Li and Cheng[41] developed a numerical model to simulate the equilibrium scour hole in clear-water scour based on the potential-flow theory. The Laplace equation of the flow velocity potential was solved for the fluid phase and the free surface was simply approximated by a horizontal streamline. The bed profile acted simply

as the bottom boundary condition to the flow, and it was determined by the force balance acting on a particle. Therefore, no particle-particle interaction was interpolated in the model. Moreover, the flow field and the bed profile were both unknown initially and had to be solved iteratively, during which process, the bed profile had to be adjusted manually to satisfy the bottom boundary condition. In addition, a characteristic velocity was used in the calculation of the drag force and lift force acting on a particle. The maximum scour depth was underestimated if the potential flow velocity was used as this characteristic velocity directly and thus it had to be modified empirically. With those approximations, the model predicted relatively well at the upstream part of the scour hole, and failed to reproduce the downstream slope.

2.4.2 Eulerian Approach with Exner Equation

In Eulerian Exner models, the governing equations of the fluid phase and the sediment transport equations are solved on an Eulerian grid. The suspended load transport is usually solved by the the convection-diffusion equations, and the bed load transport is usually resolved by empirical or semi-empirical formulas. The bed deformation is determined by the mass balance equation of sediment, i.e., Exner equation. Exner equation (Eq. 2.11) was derived from the conservation law of fluid mass by Exner in 1925 for the first time, which laid the foundation of the estuarine and river morphodynamics.

$$\frac{\partial z}{\partial t} + \frac{1}{1-n}(\nabla \cdot q) = 0, \tag{2.11}$$

where z is the bed elevation, n is the porosity of the sediment, and q is the sediment transport rate. Other forms of the mass balance equation can separate the bed load and suspended load, for example,

$$\frac{\partial z}{\partial t} + \frac{1}{1-n}(\nabla \cdot q_b - D_s + E_s) = 0, \tag{2.12}$$

where q_b is the bed load transport rate, D_s is the deposition rate and E_s is the erosion rate[46, 101]. The majority of bed load transport formulas relate the transport rate to the shear stresses, while others relate it to the velocities, for example, the Grass formula[18].

At the water-sediment interface, the bed deformation is closely related to the transient flow field. Automatic grid movement algorithm is widely adopted to deform the bed and resolve the complex mesh, and the Laplacian operator smoothing and the spring analogy are two of the methods proposed. Exner equation will provide the boundary conditions for the mesh deformation equation, i.e., the Laplacian equation, which is given by

$$\nabla \cdot (\gamma \nabla \mathbf{v}) = 0, \tag{2.13}$$

where γ is the diffusion coefficient, and $\mathbf{v}$ is the grid motion velocity. Once $\mathbf{v}$ is resolved, the grid can be relocated by

$$\mathbf{x}^{k+1} = \mathbf{x}^{k} + \mathbf{v}\Delta t, \tag{2.14}$$

where $\mathbf{x}^{k+1}$ and $\mathbf{x}^{k}$ are the grid position at time step $k+1$ and k respectively.

Zhao et al.[101] simulated the local scour around a vertical cylinder in steady currents, considering both suspended load and bed load in the model. The Arbitrary Lagrangian Eulerian (ALE) scheme was employed to solve the RANS equations with bed deformation. The bed load transport rate was resolved by a semi-empirical equation proposed by Engelund and Fredsøe[13]. The suspended load was resolved by the convection-diffusion equation. However, instead of computing the amount of sediment entrained into suspension directly in the equation, it was approximated by an empirical formula based on the bed shear stress to avoid numerical errors. Moreover, the determination of some coefficients involved in the convection-diffusion equation was largely arbitrary. In addition, the free surface was excluded, and the rigid lid assumption was made. The scour depth at the front edge of the cylinder was constantly underestimated by the model, and the modelled scour slope at the downstream side was too mild compared to the measurement. The bed elevation at the downstream side was largely underestimated. Liu and Garcia[46] used very similar approach to that employed by Zhao et

al.[101] to study the turbulent wall jet scour and wave scour around a large vertical cylinder, whereas the free surface effect was incorporated. A Laplacian smooth operator was employed for the automatic mesh deformation. The maximum scour and maximum deposition were underestimated by the model.

As pointed out by Liu and Garcia[46], mesh deformation approach has its limitations when the boundary movement is irregular. Mesh can be highly distorted and even deteriorated if the amplitude of bed movement is big, which is inevitable in scour process. Such problem puts the numerical computation at high risk and the convergence of solution is much harder to achieve. Although the dynamic mesh approach can be used to eliminate such difficulties by splitting or merging cells where necessary, this approach itself is even more difficult to implement.

2.4.3 Multiphase Approach

With the process-based nature, an multiphase approach is able to better represent each phase and the inter-phase interactions. According to treatment of the fluid and solid phase, Euler-Euler method, Euler-Lagrange method and Lagrangian method are developed, among which, the Euler-Euler method has the longest history due to its connection to the conventional numerical methods.

Euler-Euler Method

Euler-Euler Method has a long history in its development and application to investigate sediment transport and scour processes. In Euler-Euler models, both the fluid phase and the solid phase are treated as continuum, and the governing equations of both phases can be solved relatively straightforwardly on an Eulerian grid. The coupling between the two phases is usually achieved through the pressure and/or the interphase momentum exchange terms. In this way, the dynamics of each phase are resolved. As the sediment particles are treated as fluid, the fluid-particle and particle-particle interactions cannot be resolved inherently, and have to be interpolated explicitly in the Eulerian framework. Moreover, Eulerian models are typically based on cell-averaged quantities, therefore, they often struggle to model complex deformation and interface fragmentation.

Zhao and Fernando[103] simulated the scour around pipelines using an Euler-Euler coupled two-phase model embedded in the FLUENT software, excluding the free surface effect. The inadequacy of parameterisations concerning the particle-flow interaction was found to be a major problem in their model, and it caused unrealistic particle pile-up around the pipeline. Moreover, the flow adjustment to the updated bed profile happened on a time scale which a fluid parcel took to travel the whole computational domain. This huge time delay made it extremely difficult for scour simulation. Therefore, although the fluid phase and solid phase were coupled through pressure and inter-phase exchange term, rather than using the two-phase model itself, the governing equations of the fluid phase were solved based on a single-phase system without considering the effects of the solid phase. The hydrodynamic results were then used as input to the two-phase model to

calculate the solid-fluid interactions and resolve the solid phase. Thereafter the grid was regenerated, so that the time delay of the flow field's adjustment to the bed profile update could be avoided in such modelling methods. During their simulation, the time step must be very small to eliminate rapid velocity change caused by flow adjustment to the new grid. In addition, an initially sinusoidal bed profile was introduced as a disturbance to the initial evolvement of the bed.

Yeganeh-Bakhtiary et al.[93] developed a Euler-Euler two-phase model to simulate the tunnel erosion stage of the scour beneath a marine pipeline. In their model, the two-dimensional RANS equations were solved, therefore three-dimensional features both in the hydrodynamics and scour process cannot be fully resolved. The coupling between the solid phase and the fluid phase was achieved through the drag force and lift force. However, the fluid phase and bed sediment motion was simulated separately, causing potential time delay and therefore inaccuracy in the phase interactions. The depth of scour hole at the downstream side of the pipeline was over-predicted, and the bed elevation at downstream side was under-predicted. Moreover, in such two-phase models, only the water phase and sediment phase are considered, and the air phase is excluded. Therefore, the free surface effect cannot be resolved, which limits the application of such models. Such inadequacies were also reflected in other Euler-Euler two-phase models[104]. Zhu et al.[104] employed a two-dimensional Euler-Euler model embedded in FLUENT to simulate the flow around a submarine pipe with a spoiler and current-induced scour beneath the pipe. The $k-\omega\ SST$ model was applied. As the sediment phase was treated in an Eulerian approach, it was straightforward to represent inter-granular stresses using velocity gradient. Detailed results analyses were presented on the effect of spoiler and pipe gap on the pressure and velocity field of water and sandy phase as well as on the seabed scouring. However, no model-validation was presented, and the analysis was merely an interpretation of the numerical results without

theoretical assessment of the reliability of the model. In addition, only drag and lift forces were taken into consideration as the interaction forces for simplicity.

Lagrangian Method

Eulerian models are mesh-based and hence have their weakness in dealing with complex deformation and fragmentation of interfaces. Although such techniques as MAC and VOF enable Eulerian models to cope with free surface deformation problems, the maintenance of a sharp interface still remains a difficulty. The interaction between the fluid phase and the solid phase also requires special treatment. In the contrast, in Lagrangian method, to name a few, Smoothed Particle Hydrodynamics (SPH), Dissipative particle dynamics (DPD), and moving particle semi-implicit method (MPS), the inherent discrete-particle property of sediment is well represented, facilitating the inter-phase interpretation. However, as the most well-known drawback, Lagrangian models are particularly demanding on computational resources. In addition, the incorrect pressure approximation caused by a spurious pressure fluctuation is a common problem associated with the sharp fluid interfaces in such models. Therefore, either additional numerical treatment must be introduced or artificial damping factors like filtering or averaging techniques have to be involved for approximation. Moreover, in Lagrangian models, as the computational domain is discretised into particles, the representation of structures and the associated boundary condition issues are also very challenging.

Zanganeh et al.[98] developed a Lagrangian coupling two-phase model to study the current-induced scour. The sediment particles movement were simulated as

Newtonian fluids by the SPH method. They adopted the soft contact approach to account for the inter-particle collisions in the sediment phase. In addition to the aforementioned deficiencies, in their model, the fluid phase was solved without fluid-solid phase interaction first, then it was solved again after evaluating the interphase term, and this process continued until it converged. The convergence scheme needs careful examination, let alone the extra computational costs arising from such iterations. Moreover, as pointed out in the preceding sections, the hydrodynamic performance of the model was not accurate enough around the pipeline, and it led to the inaccuracy of sediment deposition at the downstream side of the pipe.

Euler-Lagrange Method

In the Euler-Lagrange method, the fluid phase is treated as a continuum on an Eulerian grid, and the solid phase is treated as discrete particles, therefore, the inherent properties of each phase are well represented, and the interaction between the phases can be resolved vividly. It is also computationally efficient compared to Lagrangian models. Euler-Lagrange models have been applied to sediment transport and scour studies recently, and they have been seen as a powerful tool to resolve the physics and reveal the mechanics involved in those processes.

Hajivalie et al.[19] developed a two dimensional Euler-Lagrange model to investigate the scour in front of a vertical breakwater. The RANS equations closed by the $k-\varepsilon$ turbulence models were solved to describe the fluid phase, and the sediment

phase was solved by the two dimensional form of the MBS model by Yeganeh-Bakhtiary et al.[94]. The local scour was simulated by extending the MBS model to account for both suspension and non-suspension mode. A Lagrangian domain for sediment was defined apart from an Eulerian domain for the fluid. The bed sediments were treated as an assemble of spherical particles of uniform diameter, and scour was investigated as the motion of a granular media from a Lagrangian point of view. Sediment transport in unidirectional flow conditions and scour in front of a vertical breakwater induced by standing waves were simulated, and good agreement was obtained in compared to the conventional formula and experimental data. However, only one-way coupling was achieved to account for the influence of fluid phase on the solid phase and no momentum feedback from the solid phase to the fluid was included, which highly limits its applications to dilute particulate flows only. The hyper-concentrated flow areas cannot be correctly resolved due to its lack of the counterforce on the fluid phase.

Yeganeh-Bakhtiary et al.[95] employed an Euler-Lagrange two-phase model to simulate the live bed scour beneath a marine pipeline. The RANS equations was solved for the fluid phase, and the distinct element method (DEM) was employed for the solid phase. It demonstrated the model's capacity to deal with live bed scour situations, however the scour depth was under-predicted, and discrepancies were observed in the shape of the scour hole beneath the pipeline. This can be due to the one-way coupling of the fluid phase and the sediment phase in their model. In addition, the limited capacity of RANS to simulate the complex and ever changing flow structures can also contribute to the discrepancy.

Andrews and O'Rourke[3] and Snider et al.[75] developed the multiphase particle-in-cell (MP-PIC) method for dense particulate flows, drawing upon the advantages

of Eulerian continuum models and Lagrangian discrete models. It has been successfully applied to combustion, sedimentations, bubbling bed dynamics and many other particulate flows[3, 33, 74, 76], which demonstrated its capacity to deal with particulate flows ranging from dilute to dense, and its advantage to reveal the physics involved in those processes. However, this approach has not yet been applied to scour studies. A number of challenges involved in this method hindered such applications, for example, how to incorporate the free surface effect with the particle based approach, and how to deal with the sediment dynamics in a packed bed where the concentration is very close to fully packed conditions.

2.4.4 Treatment of the Solid Phase

In the multiphase approach, treatment of the solid phase is particularly important, including the parameterisation of the drag force, mixture viscosity and interparticle stress, etc. To further highlight these challenges, this section reviews the existing studies in these areas to provide an in-depth background.

Drag Force

In multiphase flow, the hydrodynamic drag force acting on the solid phase is a major consideration. Normally, the drag force is expressed as

$$F_{drag} = D_p(\mathbf{U}_f - \mathbf{U}_p), \tag{2.15}$$

where D_p is a parameter related to the drag coefficient C_d, $\mathbf{U}_f$ and $\mathbf{U}_p$ are the velocity vectors of the flow and the particle respectively. Different models have been proposed in the past to determine the drag coefficient and other related parameters, catering for different research purposes. For multiphase flow, the drag force model by Andrews and O'Rourke[3] has been applied widely and proven to be suitable for a wide range of scenarios. The parameter D_p, drag coefficient C_d, and particle Reynolds number Re_p in the hydrodynamic drag term read,

$$D_p = C_d \frac{3}{8} \frac{\rho_f}{\rho_p} \frac{|\mathbf{U}_f - \mathbf{U}_p|}{r_p}, \tag{2.16}$$

$$C_d = \frac{24}{Re_p}(\theta_f^{-2.65} + \frac{1}{6} Re_p^{2/3} \theta_f^{-1.78}), \tag{2.17}$$

$$Re_p = \frac{2\rho_f |\mathbf{U}_f - \mathbf{U}_p| r_p}{\mu_f}, \tag{2.18}$$

where r_p is the radius of the particle, θ_f is the volume fraction occupied by the fluid, i.e., $\theta_f = 1 - \theta_s$.

Other forms of drag force are also reported in literature. Wang et al.[90] took into consideration the drag force, virtual mass force, lubrication force and contact force (in terms of particle collision) on the solid phase. Both translational and

rotational motions of particles were accounted for, which were governed by the Newton's second law of motion and the conservation law of angular momentum. It is noteworthy that they employed an interphase momentum transfer coefficient β for the correction of the drag model following Gidaspow's approach[17]. It combines the formulation by Ergun[14] when liquid volume fraction is less than 0.8 (β_E) and the formulation by Wen and Yu[91] when the liquid volume fraction exceeds 0.8 (β_{WY}). This method is also employed in a CFD model by Hamidipour et al.[20]. The expression for β_E, β_{WY}, and the drag coefficient C_d are expressed as,

$$\beta_E = 150\frac{\theta_s^2\mu_f}{(1-\theta_s)^2 d_s^2} + 1.75\frac{\rho\theta_s\mathbf{u}_r}{(1-\theta_s)d_s}, \qquad \theta_s \geq 0.2 \tag{2.19}$$

$$\beta_{WY} = \frac{3}{4}C_d\frac{\rho\theta_s\mathbf{u}_r}{d_s}(1-\theta_s)^{-2.65}, \qquad \theta_s < 0.2 \tag{2.20}$$

$$C_d = \begin{cases} \frac{24}{Re}(1+0.15Re^{0.687}) & Re \leq 1000 \\ 0.44 & Re \geq 1000 \end{cases} \tag{2.21}$$

To ensure the continuity of theses two formulations, a switch function φ is introduced and the interphase momentum transfer coefficient β reads,

$$\beta = (1 - \varphi)\beta_E + \varphi\beta_{WY} \tag{2.22}$$

$$\varphi = \frac{arctan[150 \times 1.75(0.2 - \theta_s)]}{\pi} + 0.5 \tag{2.23}$$

By considering the relative velocity between the solid phase and the fluid phase, and the presence of neighbouring particles, the drag force is then given by,

$$F_d = \frac{\beta V_p}{\theta_s}(\mathbf{U}_f - \mathbf{U}_p) \tag{2.24}$$

where V_p is the volume of the particle.

Mixture Viscosity

Penko et al.[62] investigated three types of effective viscosity formulations using a mixture-theory based bottom boundary layer model. In the model, the mixture momentum equation, mixture continuity equation and sediment continuity equation were solved. The mixture viscosity (μ) is a function of the local sediment concentration, the sediment grain shape and the maximum packing sediment concentration. The modified Eilers equation[11] for the mixture effective viscosity is

written as,

$$\frac{\mu}{\mu_f} = \left[1 + \frac{0.5\mu_0\theta_s}{1 - \theta_s/\theta_{cs}}\right]^2, \tag{2.25}$$

where μ_f is the viscosity of pure water, μ_0 is the intrinsic viscosity, which is a dimensionless parameter determined by the sediment grain shape, θ_s is the volume fraction of the solid phase, and θ_{cs} is the maximum packing fraction of the solid phase, which was specified as 0.644. The intrinsic viscosity increases with an increasing axis ratio of the particles; for spherical particles it is well documented as 2.5. A sensitivity test of Eilers equation with varying intrinsic viscosity (from 2.5 to 5.0) was performed. Values between 2.5 and 3.5 for the intrinsic viscosity was suitable for their model.

The other two formulations are the Krieger-Dougherty equation and the Mooney equation, which are given by Eq.2.26 and Eq.2.27, respectively.

$$\frac{\mu}{\mu_f} = \left[1 - \frac{\theta_s}{\theta_{cs}}\right]^{-\theta_{cs}\mu_0} \tag{2.26}$$

$$\frac{\mu}{\mu_f} = exp\left[\frac{\mu_0\theta_s}{1 - \frac{\theta_s}{\theta_{cs}}}\right] \tag{2.27}$$

Results indicated similar and reasonable results by the Eilers equation and the Krieger-Dougherty equation. The Krieger-Dougherty equation produced the most suspended sediment on average, which was 5% more than the Eilers equation and about 14% more than the Mooney equation. Only the Mooney equation failed to capture the turbulent vortices at flow reversal. In addition, the mixture theory model showed higher sensitivity to the variations of the effective viscosity at high solid fraction ($0.4 < \theta_s < 0.6$) than at low solid fraction ($0 < \theta_s < 0.3$). It also suggested that a decreasing effective viscosity would increase the response of the sediment to the flow.

The Eilers equation and the Krieger-Dougherty equation are the two widely accepted effective viscosity formulation, which is reassured by Penko et al.[62]. Both formulations produced similar patterns of suspended sediment and captured turbulent vortices. The only difference is that the Krieger-Dougherty equation produced a slightly larger amount of suspended sediment.

In addition to the mixture viscosity, other forms of viscosity directly acting on the solid phase are also reported. Hamidipour et al.[20] simulated gas-liquid-solid fluidized beds in the framework of multiple-Euler approach using the commercial software FLUENT. In their laminar model, a constant viscosity for the liquid and gas respectively was used. The solid shear viscosity and bulk viscosity arising from the momentum exchange due to translation and collision were calculated based on the kinetic theory of granular flow (KTGF) following the work of Syamlal et al.[86] and Lun et al.[48] respectively.

The solid shear viscosity is given by,

$$\mu_s = \mu_{s,col} + \mu_{s,kin} \tag{2.28}$$

$$\mu_{s,col} = \frac{4}{5}\theta_s \rho_s d_s g_0 (1 + e_s)\left(\frac{t_s}{\pi}\right)^{\frac{1}{2}} \tag{2.29}$$

$$\mu_{s,kin} = \frac{\theta_s d_s \rho_s \sqrt{\pi t_s}}{6(3 - e_s)}\left[1 + \frac{2}{5}(1 + e_s)(3e_s - 1)\theta_s g_0\right] \tag{2.30}$$

where g_0 is the radial distribution function, e_s is the solid restitution coefficient, and t_s is the particle granular temperature.

The solid bulk viscosity λ_s is given by,

$$\lambda_s = \frac{4}{3}\theta_s \rho_s d_s g_0 (1 + e_s)\left(\frac{t_s}{\pi}\right)^{\frac{1}{2}} \tag{2.31}$$

Such solid shear stress and solid bulk viscosity provide a new way to look at viscosity issues, however, it has not yet been employed and validated widely, and still needs further investigation.

Inter-particle Stress

The inter-particle stress model developed by Ahilan and Sleath[1] computes the inter-particle stress in a Lagrangian sense:

$$\tau_{px} = 1.2\left[\left(\frac{\theta_{cs}}{\theta_s}\right)^{\frac{1}{3}} - 1\right]^{-2} \rho_f \nu \frac{\partial \mathbf{U}_p^x}{\partial z} \tag{2.32}$$

$$\tau_{pz} = 1.2\left[\left(\frac{\theta_{cs}}{\theta_s}\right)^{\frac{1}{3}} - 1\right]^{-2} \rho_f \nu \frac{\partial \mathbf{U}_p^x}{\partial z} cot\alpha_0, \tag{2.33}$$

where τ_{px} and τ_{pz} are the inter-particle stress in the horizontal and vertical directions, respectively; α_0 is the sand friction angle. Defined in a Lagrangian framework, it can be applied to Lagrangian models straightforwardly.

Snider[73] proposed a continuum particle stress model, which was extended from the model by Harris and Grighton[22]. In this model, particles are treated as a continuum with an assumption of an isotropic inter-particle stress where the off-diagonal elements of the stress tensor are omitted. The particle normal stress is modelled by a continuum calculation of the particle pressure based on the Eulerian grid, which will then be interpolated back to discrete particle's location to calculate the normal stress due to motion and inelastic collision of particles. The model is given by,

$$\tau_p = \frac{P_s \theta_s^{\beta}}{max[\theta_{cs} - \theta_s, \varepsilon(1 - \theta_s)]}, \tag{2.34}$$

where P_s is a constant with the unit of pressure, and the recommended value of the constant β is $2 \leq \beta \leq 5$. A small number ε of the order 10^{-7} is introduced by Snider[73] to remove the spikes at close pack. Obviously, this model depends only on the solid volume fraction, and both particle size and velocity are excluded. Although it is a simple model, it has been employed and proven to be efficient in dense particulate flows[60, 73], and can help to exert the maximum packing fraction limit to each cell. Plus, compared to Lagrangian type inter-particle stress models, it is more computationally efficient.

2.5 Conclusions

In conclusion, the scour processes around offshore structures are rather complicated. In order to improve the scour prediction, the complex flow structures and turbulence properties should be resolved as a prerequisite. The horseshoe vortex and lee-wake vortex flow are critical to the scour development.

In the hydrodynamic modelling, CFD models can produce the comprehensive features in the flow field, therefore they are more suitable to simulate the scour process compared to shallow water models. In the turbulence models reviewed

here, DNS models resolve the most detailed turbulence structures and processes, however, they are also the most computationally expensive ones. LES models produce a reasonable amount of turbulence properties and are less expensive than DNS models. Within the near field scale, i.e. in the immediate neighbourhood of the individual structures, LES models are favourable choices to resolve the turbulence properties in scour studies due to its outstanding ability to capture more detailed turbulence structures than RAS models. RAS models are the least computationally expensive ones, and have a relatively longer history in application than the other two types. Within the RAS scheme, $k-\varepsilon$ model, $k-\omega$ model and $k-\omega\ SST$ model are all popular choices, and the latter two are proven to have better performance in scour problems where adverse pressure gradient is often observed.

In sediment transport and scour modelling, single-phase models are developed in the early stage due to their simplicity. The Eulerian approach with Exner equation type models implicate more detailed modelling than single-phase models, and have been applied more widely to scour studies. However, the major drawbacks in mesh deformation method or dynamic mesh approach associated with such models have largely limited their application and further development. The multiphase approach has recently been a popular choice due to its advantage in the flow-sediment and sediment-sediment interactions. Euler-Euler multiphase models are the most straightforward for numerical implementation. However, they are flawed by the continuum assumption of the solid phase, therefore they usually struggle to capture the interface fragmentations and interpret the fluid-solid phase interaction accurately. On the contrary, Lagrangian multiphase models represent the inherent properties of the solid phase well yet at a very high expense by solving both the fluid phase and solid phase as discrete particles. As an attractive alternative,

Euler-Lagrange multiphase models draw on the advantages of the former two approaches. Therefore, the inherent properties of each phase can be well represented and the computational efficiency is also retained.

Based on above review, the present research will be developed based on CFD modelling, coupling with different turbulence closure models, including LES, and RAS turbulence models. The free surface effect will be taken into account via the VOF method. The sediment transport and scour modelling will be dealt with by the Euler-Lagrange multiphase approach. However, the challenges are to implement the free surface as well as to resolve the dynamic bed evolvement in the scouring process. The existing knowledge on the treatment of the solid phase also needs further development in order to deal with the sediment transport and scour processes properly.

Chapter 3

Numerical Model

3.1 Introduction

Motivated by the multiphase particle-in-cell (MP-PIC) method developed by Andrews and O'Rourke[3] and Snider et al.[75], the present work aims to develop a new scour model for free-surface flow over a mobile bed. The hydrodynamic module solves the modified Navier-Stokes equations, which incorporate the VOF method, in an Eulerian regime; and the solid phase is described in a Lagrangian approach following Newton's Law of Motion. As the number of particles involved is enormous, it is essential to introduce the concept of parcel, which is assumed to be a group of particles with the same properties such as size, velocity etc., to ensure the feasibility of the model simulation. In this hybrid Eulerian-Lagrangian

technique, parcels are the actual computational units of the Lagrangian phase, and the inter-particle stress is used instead of the individual inter-particle collisions to reduce the computational expense.

The model is built on the platform of the open source CFD software package OpenFOAM®. The hydrodynamic module is based on an existing multiphase solver, and necessary modifications are made for the introduction of the solid phase. A new particle module is developed and fully coupled with the hydrodynamic module. In this chapter, the governing equations for the hydrodynamic module are presented first in Section 3.2. The details of the new particle module are given in Section 3.3, followed by its coupling with the hydrodynamic module in Section 3.4. The boundary and initial conditions are described in Section 3.5. The discretisation and the solution procedures are presented in Section 3.6. The conclusions are drawn in Section 3.7.

3.2 Hydrodynamic Module

The present scour model is a full three-phase (water, air, and sediment) model incorporating a free surface and a mobile bed. The fluid phase comprises of both water and air, and the solid phase refers to the sediment particles. In this section, the approaches to solve the fluid phase are presented.

3.2.1 Navier-Stokes Equations

The Navier-Stokes equations for incompressible flows are written as,

$$\nabla \cdot \mathbf{U} = 0, \tag{3.1}$$

$$\frac{\partial \rho \mathbf{U}}{\partial t} + \nabla \cdot (\rho \mathbf{U}\mathbf{U}) + \nabla \cdot \mathbf{Re} = -\nabla P + \rho \mathbf{F}_b, \tag{3.2}$$

where $\mathbf{U}$ is the flow velocity, ρ is the density, $\mathbf{Re}$ is the deviatoric viscous stress tensor, P is the pressure, and $\mathbf{F}_b$ is the body force.

As the fluid phase involves both water and air, either two sets of Navier-Stokes equations should be solved, or new techniques should be used to solve both water and air simultaneously. Apparently, the latter strategy is more computationally efficient. A modified two-fluid methodology is therefore introduced in Section 3.2.2 for this purpose.

3.2.2 Two-Fluid Methodology

The Volume of Fluid (VOF) method was first proposed by Hirt and Nichols[26] for multiphase flow simulations, based on which, a modified two-fluid methodology for incompressible flows was developed by Rusche[71] to resolve the hydrodynamics of the water and air phases, which were both assumed to be Newtonian and incompressible. The hydrodynamic module here is based on the work of Rusche[71].

In this two-fluid methodology, the volume fraction of water, α, is defined as the volume fraction occupied by the water phase in a cell, and by definition it is bounded between 0 and 1. Consequently, the volume fraction of air in a cell can be obtained by $(1 - \alpha)$. In this way, the dependent variables of the fluid phase, i.e., the mixture of water and air, can be easily expressed with the aid of α. Assuming that the standard Navier-Stokes equations can be applied to this ensemble averaged flow field, the governing equations of the two-fluid methodology are derived by substituting the ensemble averaged density and velocity into $\mathbf{U}$ and ρ in Eq. 3.1 and Eq. 3.2. Therefore, the derived governing equations have exactly the same format as the standard Navier-stokes equations for incompressible flows. The ensemble averaged density and velocity are defined by,

$$\rho = \alpha\rho_w + (1 - \alpha)\rho_a, \tag{3.3}$$

$$\mathbf{U} = \alpha\mathbf{U}_w + (1 - \alpha)\mathbf{U}_a, \tag{3.4}$$

where the subscripts w and a represent the properties of water and air, respectively. It can be easily seen that in the cells full of water, the ensemble averaged velocity is purely the velocity of water as $\alpha = 1$; and in the air, the ensemble velocity is purely that of air. The ensemble density follows the same rule. In these areas, the governing equations for the two-fluid methodology are purely the original Navier-Stokes equations.

The introduction of volume fraction α spontaneously requires an additional equation for α itself. The transport equation for α is given by,

$$\frac{\partial \alpha}{\partial t} + \nabla \cdot (\mathbf{U}\alpha) + \nabla \cdot [\mathbf{U}_r \alpha(1-\alpha)] = 0, \tag{3.5}$$

where $\mathbf{U}_r$ is the relative velocity, $\mathbf{U}_r = \mathbf{U}_w - \mathbf{U}_a$. The last term on the l.h.s. of Eq. 3.5 is an additional convective term, which is introduced for the purpose of achieving a higher interface resolution without using additional special convection schemes[30]. It is noteworthy that this term is applicable only within the interface region, of which the thickness is theoretically infinitesimal. With the definition of α itself, this term vanishes in cells where there is purely water or purely air.

By now, the governing equations for the hydrodynamic module have been derived, i.e., Eq. 3.1, Eq. 3.2 and Eq. 3.5. The continuity equation Eq. 3.1 and the transport equation of α Eq. 3.5 are simply as they are. The existing terms in the momentum equation Eq. 3.2 are worth discussing, and it will be presented in the

following section.

3.2.3 Existing Terms in Momentum Equation

The existing terms in the momentum equation Eq. 3.2, i.e., the viscous stress term, body force, and pressure term, will be discussed in this section, so that the final form of the momentum equation for the pure fluid phase can be assembled.

Viscous Stress

The deviatoric viscous stress tensor **Re** is expressed as,

$$\mathbf{Re} = -\mu[\nabla\mathbf{U} + (\nabla\mathbf{U})^T] + \frac{2}{3}\mu(\nabla \cdot \mathbf{U})\mathbf{I}, \tag{3.6}$$

where μ is the effective viscosity, and $\mathbf{I}$ is the identity matrix. The effective viscosity comprises of the fluid viscosity μ_f, which is defined for the mixture of water and air, and the eddy viscosity ν_t.

$$\mu = \mu_f + \rho\nu_t, \tag{3.7}$$

$$\mu_f = \alpha\rho_w\nu_w + (1-\alpha)\rho_a\nu_a. \tag{3.8}$$

where ν_w and ν_a are the kinematic viscosity of water and air, respectively.

As both the water and air phases are treated as Newtonian and incompressible fluids, $\nabla \cdot \mathbf{U} = 0$ is satisfied. Consequently,

$$\nabla \cdot \mathbf{Re} = -\nabla \cdot \left(\mu[\nabla\mathbf{U} + (\nabla\mathbf{U})^T]\right) = -\nabla \cdot (\mu\nabla\mathbf{U}) - (\nabla\mathbf{U}) \cdot \nabla\mu. \tag{3.9}$$

Body Force

The body force considered here is the gravitational force.

$$\mathbf{F}_b = \rho\mathbf{g}, \tag{3.10}$$

where **g** is the gravitational acceleration. The surface tension can also be included in the body force, however, it is usually negligible even at the scale of a few centimetres. Hence, the surface tension is not included in the model.

Pressure

The pressure term can be split into a dynamic pressure and a hydro-static component:

$$P = P_d + \rho \mathbf{g} \cdot \mathbf{x}, \tag{3.11}$$

where **x** is the position vector.

With this modification, the dynamic pressure P_d is zero in the area far away from the object of concern. Therefore, it facilitates the specification of pressure at the boundaries. Furthermore, when taking the gradient of Eq. 3.11 and substituting that (Eq. 3.12) into the momentum equation, the gravity term is balanced out.

$$\nabla P = \nabla P_d + \nabla(\rho \mathbf{g} \cdot \mathbf{x}) = \nabla P_d + \rho \mathbf{g} + \mathbf{g} \cdot \mathbf{x} \nabla \rho. \tag{3.12}$$

Final Form for Pure Fluid Phase

Substituting Eq. 3.9, Eq. 3.10, and Eq. 3.12 into Eq. 3.2, the final form of the momentum equation for the pure fluid phase reads,

$$\frac{\partial \rho \mathbf{U}}{\partial t} + \nabla \cdot (\rho \mathbf{U}\mathbf{U}) - \nabla \cdot (\mu \nabla \mathbf{U}) - (\nabla \mathbf{U}) \cdot \nabla \mu = -\nabla P_d - \mathbf{g} \cdot \mathbf{x} \nabla \rho. \tag{3.13}$$

3.2.4 Turbulence Closure

The $k-\varepsilon$ model, $k-\omega$ model, $k-\omega$ SST model and LES as reviewed in Chapter 2 will be used as the turbulence closure in the simulations. Regarding the RAS models, i.e., $k-\varepsilon$ model, $k-\omega$ model and $k-\omega$ SST model, the standard forms will be used. For LES, the $k-$equation sub-grid-scale models by Yoshizawa[97] will be used in some tests. The transport equation for sub-grid scale kinetic energy k_{sgs} can be written as,

$$\frac{\partial k_{sgs}}{\partial t} + \frac{\partial (u_j k_{sgs})}{\partial x_j} = \frac{\partial}{\partial x_j}\big[(\nu + \nu_{sgs})\frac{\partial k_{sgs}}{\partial x_j}\big] - C_\varepsilon \frac{k_{sgs}^{3/2}}{\Delta} + 2\nu_{sgs}\mathbf{S}_{ij}\mathbf{S}_{ij}, \tag{3.14}$$

where the sub-grid scale eddy viscosity $\nu_{sgs} = C_k k_{sgs}^{1/2} \Delta$, Δ is the cell length scale, $\mathbf{S}_{ij}$ is the strain tensor rate, and C_ε and C_k are constant.

3.3 Particle Module

3.3.1 Introduction

In the hydrodynamic module, all the dependent variables of the fluid phase are solved on the Eulerian grid. In the particle module, the solid phase, i.e., the sediment particles, is treated individually as discrete spherical particles, and is solved using Newton's Law of Motion in a Lagrangian regime. To couple these two modules, the particles need to know the ambient fluid phase properties, and the fluid phase should feel the presence of particles. For the first aspect, the fluid phase properties, such as the flow velocity etc. will be interpolated to the discrete particle positions so that the solid phase can access the information of the fluid phase. With regard to the second aspect, as the sediment particles are evolved using the multiphase particle-in-cell (MP-PIC) method, in which the particles are dealt with on a sub-grid scale, the particles' information within a cell is integrated and stored as Eulerian variables on the computational grid, via whom the fluid phase can get the feedback from the solid phase. To realise this particle based approach, a particle tracking scheme is therefore essential as given in Section 3.3.7.

3.3.2 Governing Equation

In the multiphase particle-in-cell method, a particle distribution function $\phi(\mathbf{x}_p, \mathbf{U}_p, \rho_p, V_p, t)$ is introduced to describe the particle concentration on the basis of the Eulerian grid. Therefore, it works as the bridge between the Lagrangian discrete particles and the Eulerian grid. The particle distribution function follows the Liouville equation:

$$\frac{\partial \phi}{\partial t} + \nabla_x \cdot (\phi \mathbf{U}_p) + \nabla_{\mathbf{U}_p} \cdot (\phi A) = 0, \tag{3.15}$$

where the subscript p represents the particles, V_p is the particle volume, and A is the particle acceleration, $A = \frac{d\mathbf{U}_p}{dt}$.

Particle motions are governed by Newton's Law of Motion, and the particle acceleration is expressed as

$$A = \underbrace{D_p(\mathbf{U}_f - \mathbf{U}_p)}_{\text{Drag}} - \underbrace{\frac{\nabla p}{\rho_p}}_{\text{Pressure}} + \underbrace{(1 - \frac{\rho_f}{\rho_p})\mathbf{g}}_{\text{Gravity}} + \underbrace{\frac{1}{\rho_p}\nabla \cdot (\mu_f \{\nabla \mathbf{U}_f + \nabla \mathbf{U}_f^T\})_p}_{\text{Viscous stress}} - \underbrace{\frac{1}{\theta_s \rho_p}\nabla \tau_p}_{\text{Particle stress}}, \tag{3.16}$$

where the subscript f represents the fluid phase, and τ_p is the inter-particle stress. Terms on the r.h.s. account for the acceleration due to hydrodynamic drag, dynamic pressure gradient, net buoyant force (gravitational force minus buoyant force), fluid viscous stress gradient and inter-particle stress gradient, respectively. Eq. 3.16 is not an exhaustive expression. For example, the lift force where the shear rate of the mean flow is usually involved, is not included. That is because in the MP-PIC method, particles are always at a sub-grid scale, and the shear stress in one cell or on the boundary of two adjacent cells is not significant, using the interpolated value to the particle positions instead of the flow velocity at the cell centre may have a very slightly different result though. The fluid viscous stress gradient term in Eq. 3.16 reflects the influence of the mean flow diffusivity on the particles. It is less effective in scour process than in dilute particulate flows. Therefore, this term can be neglected. Considering the MP-PIC framework and the processes important for scour studies, particle accelerations due to hydrodynamic drag, dynamic pressure gradient, net buoyant force and inter-particle stress are taken into consideration in this work. The above equation is thus simplified as

$$\frac{d\mathbf{U}_p}{dt} = D_p(\mathbf{U}_f - \mathbf{U}_p) - \frac{\nabla p}{\rho_p} + (1 - \frac{\rho_f}{\rho_p})\mathbf{g} - \frac{1}{\theta_s \rho_p}\nabla \tau_p. \tag{3.17}$$

When the agitating forces, including the hydrodynamic drag force, the pressure gradient force and the buoyant force, outweigh the resisting forces, including the gravitational force and the inter-particle stress, the particles will get entrained. The exclusion of the lift force and the viscous stress gradient force may result in a smaller agitating force. However, this potential effect is not considered significant due to the small particle size compared to the grid size.

The dynamic pressure gradient force and net buoyant force are in their standard form, while drag force and inter-particle stress have several different choices, and the selected choices will be presented in Section 3.3.5 and 3.3.6, respectively.

The particle velocity and position can then be updated in sequence by

$$\frac{D\mathbf{U}_p}{Dt} = \mathbf{A}. \tag{3.18}$$

$$\frac{D\mathbf{x}_p}{Dt} = \mathbf{U}_p, \tag{3.19}$$

Up to now, the particle acceleration, velocity and position are calculated. The calculation is on per particle basis. The fluid phase information required during this process, such as the flow velocity, is linearly interpolated from the Eulerian grid onto the discrete particle positions. Once the particle information is updated, it will be integrated back onto the Eulerian grid and stored as Eulerian variables, so that the fluid phase can feel the presence of the particles. The solid volume fraction occupied by particles in a cell, θ_s and the interphase momentum transfer from the solid phase to the fluid phase are two of such Eulerian variables. The former is introduced in the next section, and the latter will be discussed in Section 3.4.

3.3.3 Solid Volume Fraction

In the communications between Eulerian grid and Lagrangian calculation, the solid volume fraction occupied by particles in an Eulerian cell, θ_s, plays a very important role. It assembles the particle volume and location information on a discrete per particle basis back to the Eulerian grid. It can be expressed as an integral of the particle distribution function as follows, and sediment concentrations can be derived easily using θ_s.

$$\theta_s = \int\int\int \phi V_p dV_p d\rho_p d\mathbf{U}_p. \tag{3.20}$$

In scour process, particle concentrations are very high in bed load, and up in the water column, it can vary in a wide range. From a computational point of view, cases with volume fraction higher than 5% are considered as dense particulate flows where particle-particle interactions are significant[60]. The value of the solid volume fraction cannot exceed a critical value either. In the case of sandy particles, the porosity determines that the maximum volume concentration for fully packed bed is approximately 65%. Therefore, a critical solid volume fraction θ_{cs} should be employed and it is usually assigned around 0.65.

3.3.4 The Concept of Parcel

Although Euler-Lagrange models are more computationally efficient compared to Lagrangian models, it still comes at a price to simulate the particles using Lagrangian method due to the huge number of particles involved, which is usually much more than the cell numbers of the Eulerian grid. Therefore, the concept of parcel is introduced to improve the computational efficiency. Particles of the same properties such as size, velocity etc. can be grouped into parcels, and parcels are actually used as the computational unit in the Lagrangian framework. Theoretically, the number of particles in a parcel is not restrained, as long as the parcel size is smaller than the grid size. It is common to use a parcel to accommodate $10^3 - 10^4$ particles. In this way, the computational expense is saved considerably.

As aforementioned, the determination of the parcel size depends on both the grid size and the particle size. The parcel size should be no larger than the grid size, and no smaller than the particle size, otherwise, it will be meaningless. In practice, particles of the diameter $62.5 - 125$ μm are categorised as very fine sand, $125 - 250$ μm are fine sand, $0.25 - 0.5$ mm are medium sand, and $0.5 - 1$ mm are coarse sand. In cases where grid resolution can be coarse, for example, grid size is 1 cm, a parcel can accommodate 10^3 medium sand particles (for example, $d_{50} = 0.3mm$), the introduction of parcels is obviously advantageous. On the other hand, in cases where very fine grid resolution is required, for example, in the sheet flow regime, the grid size can be 0.5 mm or even smaller, and the particle size is of the same magnitude, then the strength of parcel is not very obvious, however, it will not do any harm either. Certainly, the determination of parcel size is not as arbitrary as it appears, the examples here are just to give an immediate impression. It will be

examined further in Chapter 4.

The parcel's motion is determined by the particles' properties, and all the particles within the same parcel have the same mechanical properties, which determine the forces acting on the particles, and consequently the same motion. Therefore, it is only necessary to calculate the motion of the whole parcel using the mechanical properties of one single particle in this parcel. In this sense, the notion of parcel and particle can be essentially the same, only that the number of particles to be tracked is largely reduced.

3.3.5 Drag Force

The drag force model by Andrews and O'Rourke[3] is selected in this work. The parameter D_p, drag coefficient C_d, and particle Reynolds number Re_p in the hydrodynamic drag term read,

$$D_p = C_d \frac{3}{8} \frac{\rho_f}{\rho_p} \frac{|\mathbf{U}_f - \mathbf{U}_p|}{r_p}, \tag{3.21}$$

$$C_d = \frac{24}{Re_p}(\theta_f^{-2.65} + \frac{1}{6} Re_p^{2/3} \theta_f^{-1.78}), \tag{3.22}$$

$$Re_p = \frac{2\rho_f |\mathbf{U}_f - \mathbf{U}_p| r_p}{\mu_f}, \tag{3.23}$$

where r_p is the radius of the particle, θ_f is the volume fraction occupied by the fluid, i.e., $\theta_f = 1 - \theta_s$.

3.3.6 Inter-particle Stress

As mentioned above, when the solid volume fraction is above 5%, frequent particle collision will take place and this effect cannot be neglected. A collision model is needed for this purpose. As the particles are tracked explicitly, it is straightforward to compute particle collision effect in the Lagrangian frame, for example, the inter-particle stress model developed by Ahilan and Sleath[1] (see Section 2.4.4). However, with the enormous number of particles involved, the calculation of such a process obviously consumes a huge amount of computational resource. It will require a much larger amount of time than that for the Eulerian grid, and the Euler-Lagrange model will lose its strength in computational efficiency. Therefore, for dense particulate flows in the Eulerian-Lagrangian approach, it is not common to use Lagrangian collision calculations. Instead, the effect of an isotropic particle collisional pressure is usually adopted to represent particle collisions and prevent the solid volume fraction from exceeding its critical value. Such continuum models have been proven to be suitable for Eulerian-Lagrangian regimes, and they are computationally efficient as well[60, 73].

In the present study, a continuum particle stress model[73], which is extended from the model by Harris and Crighton[22], is employed. In this model, particles are treated as a continuum with an assumption of an isotropic inter-particle stress

where the off-diagonal elements of the stress tensor are omitted. The particle normal stress is modelled by a continuum calculation of the particle pressure based on the Eulerian grid, which will then be interpolated back to discrete particle's location to calculate the normal stress due to motion and inelastic collision of particles. The model is given by,

$$\tau_p = \frac{P_s \theta_s^{\beta}}{max[\theta_{cs} - \theta_s, \varepsilon(1 - \theta_s)]}, \tag{3.24}$$

where P_s is a constant with the unit of pressure, and the recommended value of the constant β is $2 \leq \beta \leq 5$. A small number ε of the order 10^{-7} is introduced by Snider[73] to remove the spikes at close pack. Obviously, this model depends only on the solid volume fraction, and both particle size and velocity are excluded. Although it is a simple model, it has been employed and proven to be efficient in dense particulate flows[60, 73], and it can help to exert the maximum packing fraction limit to each cell.

Adopting this inter-particle stress model, the particle velocity will be updated in two stages. Firstly, the particle velocity updated by forces excluding the inter-particle stress is calculated; secondly, the particle velocity change due to inter-particle stress is calculated and added to the velocity obtained in the first stage.

The integrated form of Eq. 3.17 excluding the inter-particle stress term can be written as,

$$\mathbf{U}_{p1}^{n+1} = \frac{\mathbf{U}_p^n + \Delta t D_p \mathbf{U}_{f,p}^{n+1} - \frac{\Delta t}{\rho_p}\nabla p^{n+1} + \Delta t(1 - \frac{\rho_f}{\rho_p})\mathbf{g}}{1 + \Delta t D_p}, \tag{3.25}$$

where $\mathbf{U}_{f,p}^{n+1}$ is the fluid velocity interpolated at the particle location. The velocity change due to inter-particle stress is given by,

$$\mathbf{U}_{p2}^{n+1} = -\frac{\Delta t \nabla \tau_p}{\rho_p \theta_s (1 + \Delta t D_p)}. \tag{3.26}$$

The particle velocity updated in these two stages is then summed up to get the velocity at the new time step,

$$\mathbf{U}_p^{n+1} = \mathbf{U}_{p1}^{n+1} + \mathbf{U}_{p2}^{n+1}. \tag{3.27}$$

A particle might be moving towards a fully packed cell, and the inter-particle stress model helps to suppress this particle motion and prevent the solid volume fraction from exceeding the critical value. Practice however shows that the inter-particle friction/collision is often significant and the inter-particle stress alone is not sufficient enough to represent such large friction/collision effect and therefore to completely prevent the cells from being fully packed, which will cause both numerical instability and physical unreality. This is due to the fact that in the

inter-particle stress model of Snider[73], only the gradient of τ_p is utilised to impose the velocity correction $\mathbf{U}_{p2}$, and the magnitude of τ_p itself and therefore the value of the solid volume fraction θ_s itself is not utilised substantially. In the case of a particle up in the water column falling towards the fully packed bed, the gradient of τ_p is large due to the differences in θ_s between the bed and the water column. Therefore, the inter-particle stress model works properly to prevent the particle from falling inside the packed bed. However, in the case of a particle within the fully packed bed, θ_s is of very high value everywhere inside the bed and hence the gradient of τ_p is very small, which is not strong enough to impose the sufficient velocity correction. As a result, this particle may move from one fully packed cell to another. This is not desirable either physically or numerically. Out of technical considerations, when a particle is moving towards a fully packed region, in principle, it is forbidden. However, if the destination cell has a neighbour cell which is able to accommodate a new particle, this particle can be moved there. This is in line with the fact that when a particle enters a fully packed cell, another particle in the same cell may be repelled into a less packed region due to collision. This principle works well in the present model as a remedial measure, however, ways to improve the inter-particle stress model still need further investigation.

3.3.7 Particle Tracking Method

In hybrid Eulerian-Lagrangian models, it is essential to know where the discrete Lagrangian particles are on the Eulerian grid, so that the Lagrangian particles can feel the fluid phase correctly via the dependent variables on the Eulerian grid, and meantime the Lagrangian source terms can be imposed to the correct Eulerian

cell. Therefore, for each and every particle, we must know the exact cell which possesses this particle.

The most straightforward way to achieve that is to search the whole Eulerian grid with the particle position. However, even regardless of the number of cells in the computational domain, the number of particles makes it extremely expensive to do the searching at every time step. To avoid this operation and save computational resources, one can assume that the particles will not travel across many cells within one time step, so that cell number information from the last time step can be utilised. In this way, we check first if the particle is still in the same cell as of the last time step. If not, the new cell which possesses this particle will be determined by searching the neighbour cells of the original cell. If this is still not the case, the search will be extended outwards to the neighbours of the neighbour cells until the new cell is located correctly. This method could be a solution, whereas by the assumption, the time step must be very small so that the particles only travel across a very limited number of cells at each time step, ideally one or two cells, otherwise, it will lose its strength.

A more mature and efficient way to track the particles was proposed and revised by Nordin[55] and Macpherson et al.[49], which is adopted in this work. The cell occupancy information of all the particles is initialised at the beginning of simulations, and will be stored in following time steps unless changed. When a particle moves from its original position $\mathbf{a}$ to the final position $\mathbf{b}$ at the end of an Eulerian time step dt, its trajectory, for example, as depicted in Figure 3.1, will intersects with Face 2 by $\mathbf{p}$ and the face shared by Cell B and C by $\mathbf{p}'$.

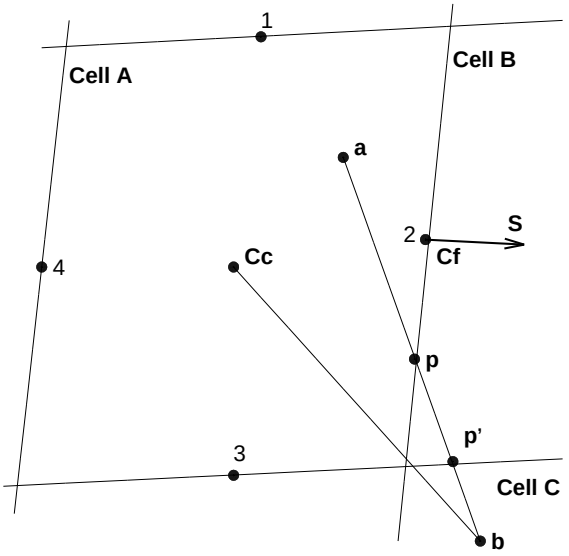

FIGURE 3.1: Sketch of a particle moving from original position **a** to final position **b**. (After Macpherson et al.[49].)

Rather than moving the particle directly to the final position **b**, the trajectory will be split into three parts: **ap**, **pp'**, and **p'b**. Consequently, the Eulerian time step will be split into three Lagrangian sub-time-steps, corresponding to each section of the trajectory. Considering the particle moving from **a** to **p**, which is on the face, the following equations are satisfied:

$$\mathbf{p} = \mathbf{a} + \lambda_a(\mathbf{b} - \mathbf{a}), \tag{3.28}$$

$$(\mathbf{p} - \mathbf{C}_f) \cdot \mathbf{S} = 0, \tag{3.29}$$

where $\mathbf{C}_f$ is the face centre, $\mathbf{S}$ is the face normal vector, and λ_a is a fraction parameter introduced to split the whole trajectory into sections. Combining these

two equations, λ_a can be derived by

$$\lambda_a = \frac{(\mathbf{C}_f - \mathbf{a}) \cdot \mathbf{S}}{(\mathbf{b} - \mathbf{a}) \cdot \mathbf{S}}. \tag{3.30}$$

With a visualised figure we can see which faces the particle will cross, however, during computation, the model needs a criteria to determine which faces are to be crossed and how the Lagrangian sub-time-steps are set.

Taking a two-dimensional grid shown in Figure 3.1 as an example, a λ_a value for each face from Face 1 to Face 4 can be calculated using Eq. 3.30. If a face is to be crossed by the particle, the λ_a value of this face should be the lowest in the the range $0 \leq \lambda_a \leq 1$, among all the faces of the original Cell A. In Figure 3.1, Face 2 meets this criteria, so it will be crossed. Therefore, the particle will be moved to position $\mathbf{p}$ with the consumption of a sub-time-step $\lambda_a dt$. As Face 2 is shared by Cell A and Cell B, the cell occupancy of this particle will be transferred to Cell B at this point. It saves the effort to search for the whole grid by utilising the face connectivity information. In the next sub-time-step, the same calculation procedure will be applied to determine which face of Cell B will be crossed so that it can move to position $\mathbf{b}$. In this example, the particle will be moved from $\mathbf{p}$ to $\mathbf{p}'$ and the cell occupancy will be transferred to Cell C. Again, we calculate the λ_a value of each face in Cell C, however, none of these values comply with the aforementioned criteria; they are either greater than 1 or less than 0, which means that the final destination lies in the same cell and no face will be crossed. Therefore, the particle will be advanced to the final position $\mathbf{b}$ using the remaining

sub-time-step.

This method works well in the situations discussed above. However, when it comes to three-dimensional unstructured grid, with non-planar cell faces, especially in concave cells, it is not robust enough. Because a face plane can be hit while the particle still remains in the same concave cell. When the face is hit, the cell occupancy is transferred to its neighbour cell sharing this face already, but the particle is still in the original cell physically. Thus in the next sub-time-step, the particle will get lost. To overcome this deficiency, Macpherson et al.[49] modified the method by introducing another fraction parameter λ_c. It is calculated simply by replacing position $\mathbf{a}$ with the cell centre $\mathbf{C}_c$,

$$\lambda_c = \frac{(\mathbf{C}_f - \mathbf{C}_c) \cdot \mathbf{S}}{(\mathbf{b} - \mathbf{C}_c) \cdot \mathbf{S}}. \tag{3.31}$$

If $\lambda_c < 0$ or $\lambda_c > 1$ applies to all the faces, the final destination $\mathbf{b}$ is within the same cell, so the particle will be advanced to $\mathbf{b}$ directly, and the cell occupancy remain unchanged. If $0 \leq \lambda_c \leq 1$, which means that the particle will hit a face before reaching the final destination, λ_a of each face will be calculated and the face to be hit will be determined using the aforementioned criteria. The particle will be moved to an intermediate position $\mathbf{p}$ using Eq. 3.28, and cell occupancy will be changed. These procedures will be repeated until the final destination $\mathbf{b}$ is reached. This modified tracking algorithm is employed in this work. More details can be found in Macpherson et al.[49].

3.4 Coupling of the Fluid Phase and Solid Phase

Exposed in the flow, the particles will move when the instantaneous fluid force on a particle just outweighs the instantaneous resistant force due to particle gravity and friction[89]. Then particles may roll, slide or saltate along the bed, and even get entrained into the water column above the bed, and move along with the flow. The influence of the fluid phase on the individual particles is represented via the drag force, the pressure gradient force and the buoyant force (see Section 3.3.2). Likewise, the dynamics of the fluid phase will be affected by the presence of the particles.

In the present study, the effects of individual particles on the fluid phase are simulated through a point-source term in the fluid momentum equation. The collective effects from many particles will become apparent on the overall fluid dynamics inside each Eulerian cell. In practice, the realisation of such interactions is usually called two-way coupling. It is four-way coupling when the particle-particle interaction is also implemented. In the present work, the four-way coupling is implemented. In particular, the particle-particle coupling is realised by adopting the inter-particle stress model as described in the preceding sections, and the influence of the flow on particles has been reflected in Section 3.3.2. In this section, the particle-fluid coupling, to be more specific, the particles' influence on the flow in terms of momentum, viscosity and volume exclusion effect, will be detailed.

3.4.1 Interphase Momentum Transfer

To maintain the computation efficiency, the present study adopts the point-source approach to represent the particle effects. In general, each individual particle is considered as a momentum source/sink in the particular Eulerian cell to the fluid motion. The overall effect from all the particles within the same Eulerian cell can then be integrated as a momentum source/sink in this particular cell. This source term is usually called the interphase momentum transfer in multiphase flow.

Particles are influenced by the flow through the drag force and pressure gradient force, and hence particles gain certain amount of momentum from the fluid phase, which means that the fluid phase lose the same amount of momentum as results of the fluid-particle interaction. Following the work by Snider[73] and Patankar and Joseph[60], the momentum source from the solid phase within a cell, $\mathbf{S}_U$, is integrated as,

$$\mathbf{S}_U = -\int\int\int \phi\rho_p V_p \left[D_p(\mathbf{U}_f - \mathbf{U}_p) - \frac{1}{\rho_p}\nabla p \right] dV_p d\rho_p d\mathbf{U}_p, \tag{3.32}$$

where ϕ is the particle distribution function, ρ_p is the particle density, V_p is the particle volume, and D_p is a parameter derived from the drag coefficient (Eq. 3.21), $\mathbf{U}_f$ is the fluid phase velocity and $\mathbf{U}_p$ is the particle velocity. This is a simple representation of the particle effects to the fluid phase in general. At the particle scale, the fluid dynamics can be fairly complex and hence there will be

energy losses that cannot be represented exhaustively by Eq. 3.32. However, in scour process, such detailed interactions are not considered important to the overall process. Therefore, the present study will not explore further into these sub-grid scale processes.

3.4.2 Mixture Viscosity

In addition to the momentum transfer, the viscosity of the fluid phase is also influenced by the presence of particles. Past studies show that in dilute suspensions, concentration and viscosity are linearly related[12, 62], and as the concentration approaches the maximum packing status, the viscosity becomes infinite[11, 62].

Several popular viscosity formulas have been reviewed in Section 2.4.4. Considering the Eulerian-Lagrangian framework, as well as the huge amount of particles involved in computation, the Eilers equation and the Krieger-Dougherty equation are more suitable and efficient to implement. Simple sensitivity tests show that there is no significant difference by applying either Eilers equation or Krieger-Dougherty equation in the present model. Therefore Eilers equation is employed hereafter for consistency.

Employing Eilers Equation[11, 62], the bulk viscosity accounting for the presence of the solid particles is modified as

$$\mu'_f = \mu_f \left[1 + \frac{0.5\mu_0\theta_s}{1 - \frac{\theta_s}{\theta_{cs}}}\right]^2, \tag{3.33}$$

where μ_0 is the intrinsic viscosity, θ_s is the volume fraction of the solid particles, and θ_{cs} is the critical value of θ_s. The intrinsic viscosity accounts for the shape of particles. For spherical particles, $\mu_0 = 2.5$ is recommended, and for irregularly shaped particles, the determination of μ_0 stays uncertain[12, 62].

The bulk viscosity is a function of the particle shape, the local sediment volume fraction and critical solid volume fraction. In general, the modified bulk viscosity is no less than the original fluid viscosity. In a cell comprising of water and air only, the solid volume fraction θ_s is zero, thus the bulk viscosity μ'_f converts back into the original viscosity of the pure fluid μ_f. When a cell approaches the maximum packing status, for example, $\theta_s = 0.64$ and $\theta_{cs} = 0.65$, the modified viscosity is several thousands times the original viscosity, in line with the findings from the past studies.

3.4.3 Volume Exclusion Effect

The presence of particles will influence the volume displacement of the fluid phase. A volume exclusion term (T_{ve}), which accounts for the displacement of the fluid phase due to particle motion, can be introduced to the l.h.s. of the momentum equation for this purpose. Following the work of Cihonski et al.[9], it reads,

$$T_{ve} = \rho \mathbf{U} \frac{\partial}{\partial t} ln\theta_f + \mathbf{U} \cdot \nabla (ln\theta_f). \tag{3.34}$$

This term was originally derived for the simulation of the volume displacement effects during bubble entrainment in a travelling vortex ring, where gas and liquid phase were involved. By applying it to the present model for scouring, results show that it has very minor effect in the interaction between the fluid phase and solid phase, while it can easily cause numerical instability issues. The examination of this term along with the interphase momentum transfer term will be presented in Chapter 4.

Therefore, the volume exclusion term has been removed from the model prior to model applications. Nevertheless, the work by Cihonski et al.[9] inspires the investigation into the volume displacement effect in terms of liquid-solid interaction, including that during the scour process.

With the modifications described in this section, the final form of the momentum equation for the dispersed fluid phase reads,

$$\frac{\partial \rho \mathbf{U}}{\partial t} + \nabla \cdot (\rho \mathbf{U}\mathbf{U}) - \nabla \cdot (\mu \nabla \mathbf{U}) - (\nabla \mathbf{U}) \cdot \nabla \mu + T_{ve} = -\nabla P_d - \mathbf{g} \cdot \mathbf{x} \nabla \rho + \mathbf{S}_U. \tag{3.35}$$

3.5 Boundary and Initial Conditions

3.5.1 Boundary Conditions

The two typical numerical boundary conditions, namely, the Dirichlet boundary condition and the von Neumann boundary condition, are available in the hydrodynamic module[30, 71]. Dirichlet boundary condition prescribes the value of dependent variables on the boundary directly, and the von Neumann boundary condition prescribes the gradient of the variables normal to the boundary. In the former case, a fixed value ϕ_B can be specified on the boundary and therefore, the values on the cell faces along this boundary are all assigned as $\phi_f = \phi_B$. In the latter case, the face gradient $\nabla\phi$ is specified, and the boundary face value can be computed by

$$\mathbf{S} \cdot \nabla\phi = |\mathbf{S}| \frac{\phi_f - \phi_P}{d_n}, \tag{3.36}$$

where ϕ_f and ϕ_P are the value of the variable on the boundary face and at the cell centre of this boundary cell, respectively, and d_n is the distance from the cell centre to the face, which is also normal to the face area.

Therefore, fixed value or fixed gradient of the dependent variables for the boundaries can be implemented directly in the model. For complex boundary conditions such as wave boundary conditions, new boundary condition types can be developed on top of the existing options.

A typical model setting involves the flow over a sandy bed. The sands are placed on the bottom boundary of the domain, and the water and air are above the bed. There are basically four types of boundaries: inlet, outlet, atmosphere and walls (see Figure 3.2). The inlet is on the l.h.s. and the outlet is downstream at the r.h.s. of the domain. For the inlet boundary, the velocity can be specified directly. Zero normal gradient of the velocity is usually applied at the outlet boundary. The slip/no-slip condition can be used on the front and back wall as needed. Zero velocity is imposed on the bottom wall and the surface of structures. The pressure gradient is set such that it provides the specified flux on each boundary according to the velocity.

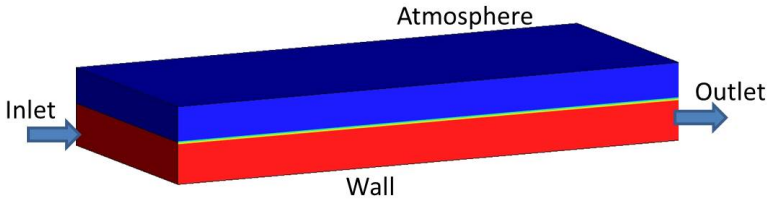

FIGURE 3.2: Sketch of a computational domain. Red: water; blue: air.

The boundary conditions in the hydrodynamic module are also applicable to the solid-phase-related Eulerian variables such as solid volume fraction θ_s. For the Lagrangian variables such as particle position and particle velocity, as they are determined by Newton's Law of Motion, once the initial values are assigned, those values will be calculated accordingly. When a particle reaches the downstream

boundary, it will no longer remain in the solution domain. When periodic boundary condition is assigned, particles will re-enter from the corresponding boundary into the domain again once exit a periodic boundary.

The time step Δt used in a simulation is determined by both the Courant-Friedrichs-Lewy (CFL) condition and the particle time scale $\tau_t = \frac{\rho_p d_p^2}{18\mu}$. Δt must be smaller than the time step required by the CFL condition and the particle time scale. The time step determined this way will be used as the Eulerian time step in the simulation for both the hydrodynamic module and particle module. The Lagrangian sub-time-step used to evolve particles will then be determined automatically during simulation.

3.5.2 Initial Conditions

The initial conditions in the hydrodynamic module can be specified for each Eulerian variable according to test configurations. The initialisation of the Lagrangian variables needs special treatment as they are not based on the Eulerian grid. A particle initialiser was devised for this purpose.

Initialisation of the Parcel Positions

As parcels are the actual computational unit in the particle module, the particle input actually refers to that of the parcels. The parcels' diameter, initial velocity and positions are the necessary input for the particle module. Parcels' initial velocity can be set as required. Parcels' diameters can be determined by other factors, as long as it is smaller than the grid size and larger than particle size. It will be determined along with the initialisation of the particle positions.

In scour process, it usually starts with a sand bed where the cells within the bed are fully packed or close to fully packed. In MP-PIC method, the parcel diameter should be smaller than the grid size. It is worth mentioning that parcel diameter is different from the median particle size d_{50}. Particle d_{50} is assigned according to the experimental set-up or in-situ observations, and will be used to calculate particle Reynolds number and particle motion. The parcel diameter is only used to calculate the parcel volume during the simulation where necessary. Sensitivity tests show that cases with the ratio of the grid spacing to parcel diameter within $3 - 4$ produce reasonable results (See Chapter 4). Bigger ratios than 4 should be suitable as well, but the amount of parcels involved will increase remarkably, which increases the computational expenses dramatically. With these rules in mind, an initialisation method is proposed here.

In the particle initialiser, the particle region is specified first. If it is fully packed and the critical solid volume fraction $\theta_{cs} = 0.65$, each cell in this region will accommodate 42 parcels. The parcel diameter will be set to 0.309 times the cell

length scale. In this way, the solid volume fraction will be approximately 0.6488, close to θ_{cs}. In each cell, the parcels will be distributed randomly. A parcel's position, $\mathbf{x}_p$, is determined by the cell centre $\mathbf{c}$, cell length L and the random number vector $\mathbf{R}$. Each component of this random number vector $\mathbf{R}$ is between 0 and 1. The parcel's position is derived by

$$\mathbf{x}_p = \mathbf{c} + \frac{1}{2}(2\mathbf{R} - 1) \cdot L. \tag{3.37}$$

In this way, parcels are all located within the specified particle region and the distribution results satisfy the solid volume fraction as needed. The numbers in the example above, such as number of parcels per cell, can be easily modified to suit the experimental conditions.

3.6 Discretisation and Solution Procedures

3.6.1 Discretisation

The Finite Volume Method (FVM) is employed to discretise the Eulerian solution domain into control volumes (CV), also called cells (see Figure 3.3). $\mathbf{x}_{i,j,k}$ is the position vector of the cell centre, $\mathbf{V}_{i,j,k}$ is the cell volume, f is the face centre

and **S** is the face area vector, normal to the face and pointing outward of the cell. Control volumes do not overlap with each other, and they fill up the solution domain completely. These control volumes are arbitrarily unstructured; therefore it is convenient to resolve complex geometry and achieve local grid refinement.

To cater for the unstructured grid, all the dependent variables associated with the equations are stored on a CV basis in a collocated arrangement. However, a major disadvantage of such collocated arrangement is the checkerboard effect in the pressure solution field. The spirit of the Rhie-Chow interpolation method[64] is therefore adopted to overcome this drawback. More details can be found in the work by Jasak[30].

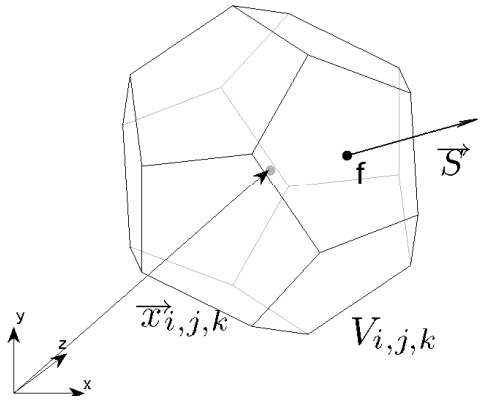

FIGURE 3.3: Control volume.

When it comes to the discretisation of the equations, there are two main issues, non-linearity of the momentum equation and the pressure-velocity coupling[30]. Regarding the first issue, rather than solving a non-linear system, the momentum equation can be linearised to save computational resources. For example, the standard transport equation for a scalar ϕ is,

$$\frac{\partial \rho\phi}{\partial t} + \nabla \cdot (\rho \mathbf{U}\phi) - \nabla \cdot (\rho\Gamma_\phi \nabla\phi) = S(\phi), \tag{3.38}$$

where the temporal derivative term, convection term, diffusion term and source term are all present.

The integral form of this equation over the control volume V_P should satisfy,

$$\int_t^{t+\Delta t} \left[\frac{\partial}{\partial t} \int_{V_P} \rho\phi dV + \int_{V_P} \nabla\cdot(\rho\mathbf{U}\phi) dV - \int_{V_P} \nabla\cdot(\rho\Gamma_\phi \nabla\phi) dV \right] dt = \int_t^{t+\Delta t} \left(\int_{V_P} S(\phi) dV \right) dt. \tag{3.39}$$

As the transport equation is second-order, the discretisation should be equal or higher than the order of the equation to maintain the accuracy. Applying Gauss' theorem and assuming that the control volumes do not change with time, a "semi-discretised"form[25] reads,

$$\int_t^{t+\Delta t} \left[\left(\frac{\partial \rho\phi}{\partial t} \right)_P V_P + \sum_f F\phi_f - \sum_f (\rho\Gamma_\phi)_f \mathbf{S}\cdot(\nabla\phi)_f \right] dt = \int_t^{t+\Delta t} (SuV_P + S_p V_P \phi_P) dt, \tag{3.40}$$

where F is the mass flux, and Su and Sp come from the linearisation of the source term,

$$S(\phi) = Su + Sp\phi. \tag{3.41}$$

To make sure that the discretisation is second-order accurate, the temporal scheme must be second-order accurate. For example, backward differencing in time can be used to achieve the final discretised equation, where three time levels, "00", "0", and "n"in time sequence are used,

$$\frac{\partial \phi}{\partial t} = \frac{\frac{3}{2}\phi^n - 2\phi^0 + \frac{1}{2}\phi^{00}}{\Delta t}. \tag{3.42}$$

The final discretisation form using this temporal scheme is[30],

$$\frac{\frac{3}{2}\rho_P\phi^n - 2\rho_P\phi^0 + \frac{1}{2}\rho_P\phi^{00}}{\Delta t}V_P + \sum_f F\phi_f^n - \sum_f (\rho\Gamma_\phi)_f \mathbf{S}(\nabla\phi)_f^n = SuV_P + SpV_P\phi_P^n. \tag{3.43}$$

A semi-discretised form of the momentum equation can be expressed as follows by applying the aforementioned discretisation procedure,

$$a_P^U \mathbf{U}_P = \mathbf{H(U)} - \nabla P_d, \tag{3.44}$$

where a_P^U is the diagonal coefficients of the momentum equation matrix, and $\mathbf{H(U)}$ is the the non-diagonal coefficient comprising of the convective and diffusive terms, the source part of the transient term, and other source terms in the momentum equation apart from the pressure gradient.

The discretised form of the continuity equation reads,

$$\sum_f \mathbf{S} \cdot \mathbf{U}_f = 0. \tag{3.45}$$

By rearranging Eq. 3.44, the velocity can be expressed as,

$$\mathbf{U}_P = [a_P^U]^{-1} \Big\{ \big[\mathbf{H(U)}\big] - \nabla P_d \Big\}. \tag{3.46}$$

The velocities on cell faces can be obtained by interpolating Eq. 3.46 to the face centres,

$$\mathbf{U}_f = [a_P^U]_f^{-1} \Big\{ \big[\mathbf{H}(\mathbf{U})\big] - \nabla P_d \Big\}_f . \tag{3.47}$$

When this equation is solved implicitly, the predicted velocity does not satisfy the continuity equation automatically. Moreover, in this equation, the pressure field used is from the previous time step. Therefore, a Poisson equation is needed, which can be derived by substituting Eq. 3.47 into the continuity equation, Eq. 3.45,

$$\nabla \cdot \left(\frac{\nabla P_d}{a_P^U} \right) = \nabla \cdot \left(\frac{\mathbf{H}(\mathbf{U})}{a_P^U} \right). \tag{3.48}$$

The r.h.s. of Eq. 3.48 is the divergence of the velocity flux, which is $\nabla \cdot \phi$ in the standard transport equation. To account for the effects of the particles on the fluid phase, the interphase momentum transfer term, $\mathbf{S}_{imt}$, is added to the velocity flux, which reads,

$$\mathbf{S}_{imt} = \mathbf{S}_U \cdot \frac{\mathbf{S}}{|\mathbf{S}|}, \tag{3.49}$$

where $\mathbf{S}_U$ is the momentum source from the solid phase introduced in Section 3.4.1.

Following Eq. 3.44 and Eq. 3.48, the final discretised Navier-Stokes equations read,

$$a_P^U \mathbf{U}_P = \mathbf{H}(\mathbf{U}) - \sum_f \mathbf{S} \cdot (P_d)_f \tag{3.50}$$

$$\sum_f \mathbf{S} \cdot \left(\frac{\nabla P_d}{a_P^U} \right)_f = \sum_f \mathbf{S} \cdot \left(\frac{\mathbf{H}(\mathbf{U})}{a_P^U} \right)_f . \tag{3.51}$$

The updated pressure field can then be used to correct the velocity field. Finally, the face flux that satisfies the continuity conditions can be obtained by multiplying Eq. 3.47 by the cell face vector $\mathbf{S}$,

$$F = \mathbf{S} \cdot \mathbf{U}_f = \mathbf{S} \cdot \left[[a_P^U]_f^{-1} \left\{ \left[\mathbf{H}(\mathbf{U}) \right] - \nabla P_d \right\}_f \right]. \tag{3.52}$$

The linearisation of equations facilitates the numerical computation, however, it involves approximations inevitably. Moreover, second-order accuracy of the finite volume method is only a minimum numerical requirement. Such implementation can implicate errors in the numerical results.

For the particle module, as it is already on a discrete per particle basis, the calculation is straightforward. The updated fluid properties on the Eulerian grid will be linearly interpolated to the particle positions prior to advancing the particles. The particle velocity can be updated by Eq. 3.27. The particle position can then be updated by

$$\mathbf{x}_p^{n+1} = \mathbf{x}_p^n + \mathbf{U}_p^{n+1}\Delta t. \tag{3.53}$$

3.6.2 Solution Procedures

The pressure-velocity coupling of the Navier-Stokes equations requires special treatments. The PIMPLE algorithm is employed for this purpose. It is a merged algorithm of PISO (Pressure Implicit with Splitting of Operators)[28] for transient flows and SIMPLE (semi-implicit method for pressure-linked equations) for steady flow[61]. In the PIMPLE algorithms, the equations are all solved in a segregated approach.

In the present model, the fluid phase is solved first with the PIMPLE algorithm, and the particle velocity and position are then updated using the updated fluid phase properties at the current time step. Particles' influence on the fluid phase, e.g., the interphase momentum transfer, is calculated while evolving the particles, and it will be included in the solution of the fluid phase at the next time step. In

the PIMPLE algorithm, the momentum equation is solved first with the pressure field obtained from the last time-step. Then the operator $\mathbf{H(U)}$ and the pressure equation can be assembled in sequence, so that the initial estimation of pressure field can be obtained, which will be used to correct the velocity field. After that, the pressure equation will be solved again and the non-orthogonality will be corrected. These procedures will be repeated until the desirable residual tolerance is reached. In short, in this PIMPLE loop, the implicit momentum predictor is followed by a series of pressure solutions and explicit velocity corrections[30]. When it comes to steady-state flows, the non-linearity of the system outweighs the issue of pressure-velocity coupling. Therefore, under-relaxed equations can be solved to cater for more flexibility and save computational resources caused by unnecessarily large number of time-steps. More details can be found in Jasak[30]. Once the hydrodynamic information is updated, the particles can then be advanced using the up-to-date flow information. Particle velocity and position are calculated using Eq. 3.27 and 3.53, respectively. The influence of the particle on the flow, such as the interphase momentum transfer, is also calculated and will be involved in the calculation of the flow at the following time step. Now the solution procedures are summarised in Figure 3.4.

3.7 Conclusions

In conclusion, a full three-phase scour model for a mobile bed with a free surface is developed. It maintains the computational efficiency while represents each phase in a natural way. In this Euler-Lagrange scour model, the flow-particle coupling

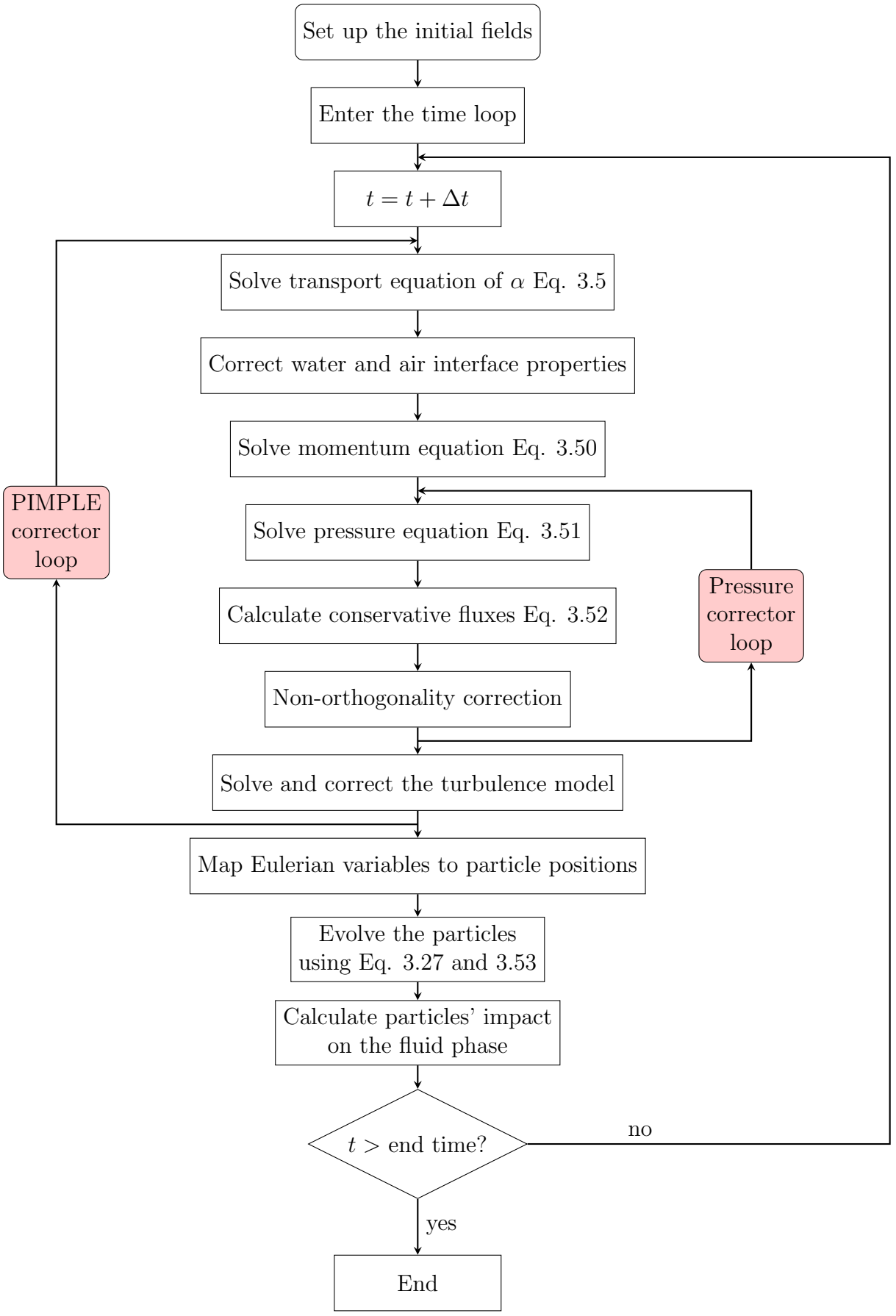

FIGURE 3.4: Flow chart of the solution procedure.

and particle-particle interactions are fully resolved, therefore, four-way coupling is achieved.

In the hydrodynamic module, the fluid phase is resolved on the Eulerian grid by solving the modified Navier-Stokes equations with a two-fluid methodology incorporating the Volume of Fluid method for the free surface. The momentum transfer from the solid phase to the fluid phase is considered in the momentum equation. Particles' influence on the fluid viscosity is also included in the model.

The multiphase particle-in-cell method is adopted to solve the solid phase in a Lagrangian framework following Newton's Law of Motion. Therefore, the discrete-particle nature of the solid phase is very well represented. The movement of individual particles can be physically tracked at each time step, which reveals detailed scour processes which continuum models struggle to achieve. Particle accelerations due to hydrodynamic drag force, dynamic pressure gradient, net buoyant force and inter-particle stress are all accounted for. Special treatment is employed to track the particles' cell occupancy information efficiently.

The Finite Volume Method is used to discretise the Eulerian solution domain, and the governing equations are discretised to second-order accurate. The PIMPLE algorithm is employed to deal with the pressure-velocity coupling and solve the system of equations. Particles can then be advanced using the updated fluid phase information.

Chapter 4

Model Calibration

4.1 Introduction

Prior to realistic applications, the model needs to be calibrated and validated via simple tests and several aspects of the model implementations should be examined. Firstly, the particle motion related implementations are validated through particle falling tests in still water. The computed fall velocity is compared to its theoretical value. Secondly, various ranges of the grid spacing to parcel size are tested to identify the optimal value that can be used in practical applications. Thirdly, the influence of the particles on the fluid phase, i.e., the interphase momentum transfer term and the volume exclusion term, are examined by a series of isolated block tests. The results and discussions are presented in this chapter.

4.2 Particle Falling Tests

Particle falling tests are carried out to examine the numerical implementation concerning particle motion. Cases with various particle median diameter d_{50} are simulated. The computed particle fall velocity is compared to its theoretical value. In addition, cases with various grid spacing ratio to parcel diameter are tested to get a desirable range of this size ratio.

4.2.1 Cases of Various Particle Size

Two single-parcel-falling-in-still-water tests are carried out to examine the model's behaviour at low solid volume fraction. The only difference between these two tests is the number of particles per parcel (see Table 4.1), consequently, the particle d_{50} varies. The test domain in both tests is 0.05 m long, 1 m high, and 0.005 m wide. The grid spacing is 5 mm uniformly in each direction, therefore, it is one cell wide in the z direction. The water depth is 0.8 m. An initially still parcel of a diameter 2.5 mm falls from a height of 0.7 m. The time step is 0.0005 s. Assuming that the fluid phase velocity is zero, the forces applied to the particle including gravity, drag force from fluid and buoyancy force. Once the forces balance out, the particle can reach its terminal fall velocity. By comparing the computed fall velocity with the theoretical values, the implementation of these force terms can be verified, especially the drag force term that needs to be calibrated.

Test number	Number of particles per parcel	Particle d_{50}
PFV-1	1	2.5 mm
PFV-2	1000	0.25 mm

TABLE 4.1: Particle properties in Test PFV-1 and PFV-2

To verify the model in terms of particle motion, the computed particle velocity is compared with the theoretical value. Following the approach of van Rijn[89], the theoretical fall velocity is determined from the balance of the forces acting on a particle (Eq. 4.1) with the assumption that the flow velocity is zero. The terms on the l.h.s. of Eq. 4.1 represent the gravitational force, the buoyant force and the drag force on the particle, respectively.

$$\frac{\pi}{6}d^3\rho_p g - \frac{\pi}{6}d^3\rho g - \frac{1}{2}C_d\rho w_s^2(\frac{\pi}{4}d^2) = 0 \tag{4.1}$$

Here, d is the particle diameter, ρ_p is the density of the particle, C_d is the drag coefficient, ρ is the density of water, and w_s is the terminal fall velocity of a spherical particle in still water. The drag coefficient in the model is expressed by Eq. 3.22, which is a function of the particle Reynolds Number, Eq. 3.23. As water is assumed to be still, $\mathbf{U}_f = 0$ is satisfied in Eq. 3.23, and $\mathbf{U}_p$ is thus w_s. A non-linear equation of w_s can be derived by substituting Eq.3.22 and Eq.3.23 into Eq.4.1, which reads,

$$C_1 w_s + C_2 w_s^{1.667} - C_3 = 0, \tag{4.2}$$

where C_1, C_2 and C_3 are constant:

$$C_1 = \theta_f^{-2.65}, \tag{4.3}$$

$$C_2 = 0.1667\left(\frac{\rho d}{\mu}\right)^{0.667}\theta_f^{-1.78}, \tag{4.4}$$

$$C_3 = \frac{(\rho_p - \rho)gd^2}{18\mu}. \tag{4.5}$$

This non-linear equation is solved using the Levenberg-Marquardt algorithm (LMA)[39]. The theoretical fall velocity of PFV-1 and PFV-2 are 0.0293 ms^{-1} and 0.3114 ms^{-1}, respectively.

To satisfy the assumption that the flow is stationary during the simulation, the influence of particles on the fluid phase is turned off in the model, therefore the fluid phase remains undisturbed.

Good agreement between the modelling results and the theoretical fall velocity is shown in Figure 4.1. The modelled fall velocity and the theoretical value in PFV-1 are 0.31 ms^{-1} and 0.3114 ms^{-1}, respectively. Those in PFV-2 are 0.029 ms^{-1} and 0.0293 ms^{-1}, respectively. The model under predicts it by 0.45% and 1.02% in PVF-1 and PVF-2, respectively. Considering the numerical accuracy limited by truncated errors etc., this high agreement between the modelled value and the theoretical value is considered to be satisfactory. It confirms that the numerical

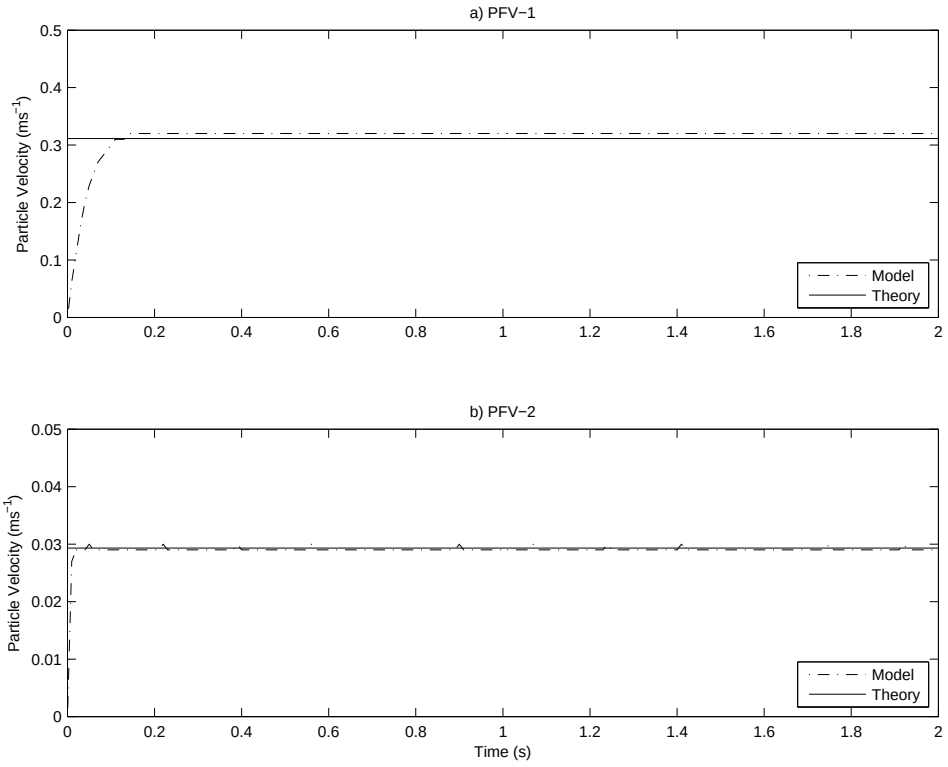

FIGURE 4.1: Computed particle fall velocities in comparison with the theoretical values.

implementation in the model concerning particle motion is reliable. Figure 4.1 also illustrates that the initial acceleration stage differs between these two tests. In PVF-1, the particle velocity has reached its terminal velocity after around 0.18 s, whereas in PVF-2, the terminal velocity is reached almost instantly after release. This demonstrates the fact that the fall velocity of fine particles is much smaller and can be achieved faster than that of the coarse ones.

4.2.2 Cases of Various Grid Spacing Ratio to Parcel Diameter

Theoretically, the particle fall velocity only depends on the particle properties such as the particle size and density (see Eq. 4.1). However, the drag coefficient C_d is determined empirically, and in this model, it is also a function of the fluid phase volume fraction. Therefore, it is influenced by the solid volume fraction in a cell. Different ratio of the grid spacing to the parcel diameter leads to different solid volume fraction in each test, and hence the modelled particle fall velocities in cases with the same particle d_{50} can be different. Likewise, the solid volume fraction is also involved in the interphase momentum transfer term and volume exclusion term, which should be a function of the solid phase and fluid phase properties, rather than the grid size. This can be seen as a limit of numerical models, but reasonable measures can be adopted to minimise this impact.

Particle Fall Velocity

For the particle falling test PFV-2, three follow-up tests are carried out to test the influence of the ratio of the grid spacing to parcel diameter on the modelling results, and identify the desirable ratio range for the model application. In these tests, the only variable changed is the grid size and all the other set-up remains the same as in PFV-2. Detailed information of each tests is listed in Table 4.2.

Test number	Grid spacing (mm)	Ratio of grid spacing to parcel diameter
PFV-2	5	2
PFV-2.1	2.5	1
PFV-2.2	7.5	3
PFV-2.3	10	4
PFV-2.4	20	8

TABLE 4.2: Cases of various grid spacing.

The theoretical fall velocity derived by Eq. 4.2 and the corresponding modelling results in these tests are shown in Table 4.3. When the grid spacing is the same as the parcel diameter, the theoretical value itself is not realistic as a result of a large solid volume fraction, let alone the large difference between the modelled value and the theoretical value. When the grid size is twice the parcel diameter, the modelled fall velocity is the closest to its theoretical value. When the grid size is three times as large as or larger than the parcel diameter, the theoretical fall velocity converges, and the modelled fall velocity is very close to the corresponding theoretical value. Therefore, to minimise the inevitable limit, the grid size should be three times as large as or larger than the parcel size.

Test number	Solid fraction	Theoretical fall velocity (ms^{-1})	Modelled fall velocity (ms^{-1})
PFV-2	0.0654	0.0293	0.0290
PFV-2.1	0.5236	0.0071	0.0015
PFV-2.2	0.0194	0.0319	0.0340
PFV-2.3	0.0082	0.0326	0.0350
PFV-2.4	0.001	0.0330	0.0350

TABLE 4.3: Theoretical fall velocity and modelling results.

Interphase Momentum Transfer Term and Volume Exclusion Term

As described in Chapter 3, the interphase momentum transfer term imposes the momentum impact from the solid phase to the fluid phase (see Eq. 3.32). As

the drag coefficient is involved, this term can also be affected by the ratio of grid spacing to parcel diameter. Likewise, the volume exclusion term (see Eq. 3.34) involves the local temporal and spatial variation of the fluid volume fraction due to particles' motion, therefore, it is also affected by the ratio of the grid spacing to the parcel diameter.

Test number	Grid spacing (mm)	Ratio of grid spacing to parcel diameter
T-1	3.6	1
T-2	7.2	2
T-3	10.8	3
T-4	14.4	4
T-5	28.8	8

TABLE 4.4: Cases of various grid spacing with d_{50} being 0.36 mm.

A series of tests are carried out to examine these two terms with respect to different grid spacing ratios to the parcel diameter. In these tests, the particle d_{50} is 0.36 mm, which is the same value as in a benchmark test by Mao[50]. The parcel diameter is 0.72 mm in each test. The grid spacing used in each test is shown in Table 4.4.

The magnitude of the interphase momentum transfer term and volume exclusion term are shown in Figure 4.2. It is noteworthy that the particles in the all five tests are still falling in the water column toward the bottom wall at 2 s. Therefore, the influence of the bottom boundary is not applicable. It is seen that when the grid spacing is the same as the parcel diameter, the magnitude of the interphase momentum transfer term is neither realistic nor stable. This is because the parcel volume occupies approximately 52% of the cell volume. When the parcel moves from one cell to another, the solid volume fraction of the original cell drops from 0.52 to 0 within a single Lagrangian sub-time-step. Meantime that of the new cell increases from 0 to 0.52. This sharp change induces large oscillation as seen in Figure 4.2. When the grid spacing is twice the parcel diameter or larger, the

magnitude of the interphase momentum transfer term converges among different tests and stays stable regardless of the grid spacing ratio to the parcel diameter. When grid spacing is between two to four times the parcel diameter, the magnitude of interphase momentum transfer term fluctuates slightly over time. When the grid size is five times the parcel diameter, no fluctuation is observed, which is in favour of the numerical stability.

As for the volume exclusion term, which is shown in Figure 4.2b, the influence of the grid spacing ratio on this term is significant. The magnitude difference can be as large as 10^4 for the same particle falling on computational grids with different grid spacing. This is mainly due to the fact that the volume exclusion term is a function of the temporal and spatial derivatives of the natural logarithm of the fluid volume fraction. Thus, it is very sensitive to the ratio of the grid spacing to the parcel diameter. Furthermore, only when the grid spacing is as large as five times the parcel diameter, no significant fluctuations are observed, otherwise, large fluctuations in magnitude always exist, which can be a potential severe hazard to the numerical stability.

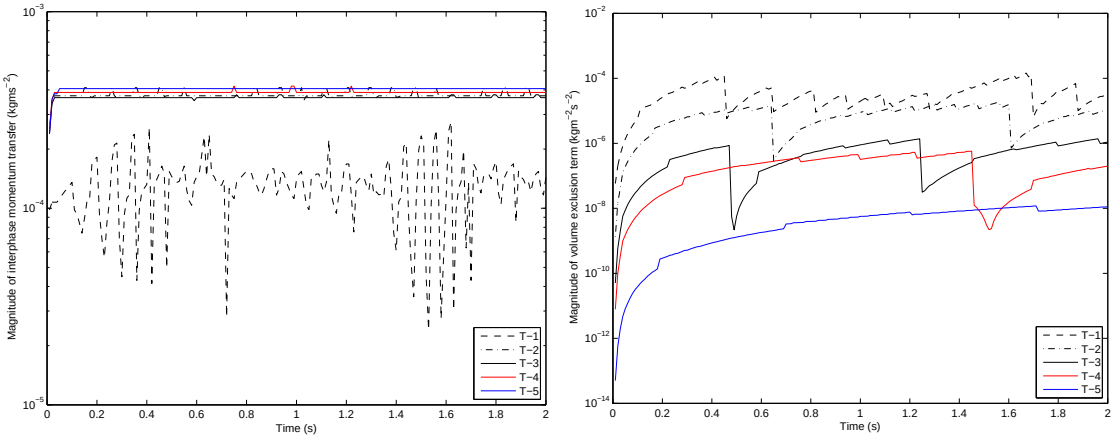

(A) Magnitude of the interphase momentum transfer term

(B) Magnitude of the volume exclusion term

FIGURE 4.2: Magnitude of the interphase momentum transfer term and volume exclusion term.

When the grid spacing is twice, three times, four times, or five times the parcel diameter respectively, the magnitude of the interphase momentum transfer term is roughly two orders, three orders, four orders or five orders as large as that of the volume exclusion term. Therefore, the interphase momentum transfer term is always dominant.

Considering the influence of the grid spacing ratio to the parcel diameter on the particle fall velocity, the interphase momentum transfer term and the volume exclusion term, the results so far indicate that the larger this size ratio is, the better results can be achieved. When the size ratio is between three and four, acceptable predictions are obtained. When the size ratio is as large as five, the best results concerning all these three aspects are achieved. However, a grid spacing ratio to parcel size as large as five means that there could roughly be as many as $5^3 \cdot \theta_{cs}$ parcels in a single cell. Considering cases with a mobile bed, where considerable number of cells are close to fully packed, the number of parcels involved in calculation is definitely a heavy burden, or even exceptionally huge. Therefore, a grid spacing ratio to parcel diameter ranging from three to four is recommended for a reliable prediction while maintaining the computational efficiency.

4.3 Isolated Block Tests

The magnitude of both the interphase momentum transfer term and the volume exclusion term are examined in the preceding section for a single particle falling in the water column. However, the influence of a single particle on the fluid

phase is not significant. In order to test the impacts of the particles at high volume fraction on the fluid phase and hence examine the implementation of these two terms, large number of particles are needed. In this section, a large number of particles in nearly fully packed conditions will be used for this purpose. In particular, an isolated block of particles is placed in the flow. Tests with the isolated block located in the middle of the flow, on the bottom wall and at a trench corner are performed respectively. Details of the flow passing this block can reveal whether the implementation of the two terms are correct in terms of the fluid hydrodynamics. The detailed set-up of the tests are listed in Table 4.5. To minimise other effects, particles are fixed, and the focus is placed on the reaction of the flow field to the presence of particles. The modelling results with both terms on, only the interphase momentum transfer term ($\mathbf{S}_U$) on, and only the volume exclusion term (T_{ve}) on are presented.

Test number	Block location in the flow	Interphase momentum transfer	Volume exclusion term
MDL-1	middle	✓	✓
MDL-2		✓	○
MDL-3		○	✓
BTM-1	bottom	✓	✓
BTM-2		✓	○
BTM-3		○	✓
CRN-1	corner	✓	✓
CRN-2		✓	○
CRN-3		○	✓

TABLE 4.5: Model set-up in the isolated block tests.

The mesh resolution in these tests is 2.5 mm, and it is one cell wide in the transverse z direction. Slip boundary conditions are applied to the front and back $xy-$planes. A steady current boundary condition is imposed at the inlet boundary. The mean flow velocity is 0.35 ms^{-1}. The diameter of the parcel is 0.72 mm,

and particle d_{50} is 0.36 mm. The maximum solid volume fraction in the block is 0.58. The time step is 0.0005 s.

The modelled flow fields and velocity profiles at selected sections in MDL tests are shown in Figure 4.3. The flow velocity fields produced with both the source terms on (MDL-1), and those produced with only the interphase momentum transfer term on resemble with each other, and the physical effects of the source terms are well represented. As shown in Figure 4.3a, 4.3b, 4.3c, and 4.3d, the fluid phase is affected by the presence of the particle block and flows around the block as expected, and vortices in the lee-wake side and flow reversal are captured. As the block of particles is a porous medium, water can flow into the block, and the flow inside it is very minor as expected. The magnitude and direction of the velocity vectors in MDL-1 and MDL-2 agree with each other very well. The only difference between these two tests is that in MDL-2, the volume exclusion term is turned off. It implies that, the volume exclusion term has much less effect than the interphase momentum transfer term, which is consistent with the results in the particle falling tests. When the interphase momentum transfer term is turned off and the volume exclusion term is on, instead of getting blocked by the particles, the flow squeezes into the block and accelerates there due to the spatial gradient of the fluid volume fraction in and around the block. Inside the block, flow accelerates to two to three times the mean flow velocity (see Figure 4.3e and 4.3f). This effect is not desirable for scour studies.

To testify whether the presence of the particles at boundaries can cause problems, the block of particles is placed on the bottom boundary (BTM tests). The modelled flow velocity field and velocity profile at selected sections are shown in Figure 4.4. The flow velocity around the block decelerates and the vortices in the

lee-wake side are fully resolved when the interphase momentum transfer term is on. The velocity profiles are well developed and captured as well. When only the volume exclusion term is on, the flow accelerates inside the block and no vortex is observed. In short, the interphase momentum transfer term achieves the physical impact of the solid phase back on the fluid phase reasonably while the volume exclusion term results in unrealistic flow acceleration inside the block, and the effect of the latter is much less than the former. In the CRN tests, the block of particles is placed at a trench corner. Again, the same phenomena are observed as shown in Figure 4.5.

To further confirm the difference in the tests with both source terms on and with only the interphase momentum transfer term on, the velocity field in the former tests is deducted by that in the latter tests. The velocity difference in the three series of tests is shown in Figure 4.6 to visualise the contribution of the volume exclusion term when both source terms are on. It is clear that the volume exclusion term has little effect in the upstream and the far field. It only has impact on the circulation zone immediately downstream of the block. Water in the downstream side tends to flow upstream towards the block, which is not realistic physically. It again gives a preliminary suggestion that this term is not desirable for scour studies and needs further investigation.

The magnitudes of the interphase momentum transfer term and the volume exclusion term are shown in Figure 4.7. The maximum values of both terms are observed at the two corners of the block at the upstream side in the MDL tests, and at the upper left corner in BTM and CRN tests where the block rests on the bottom boundary. The maximum value of the interphase momentum transfer term is one order larger than that of the volume exclusion term. In the majority

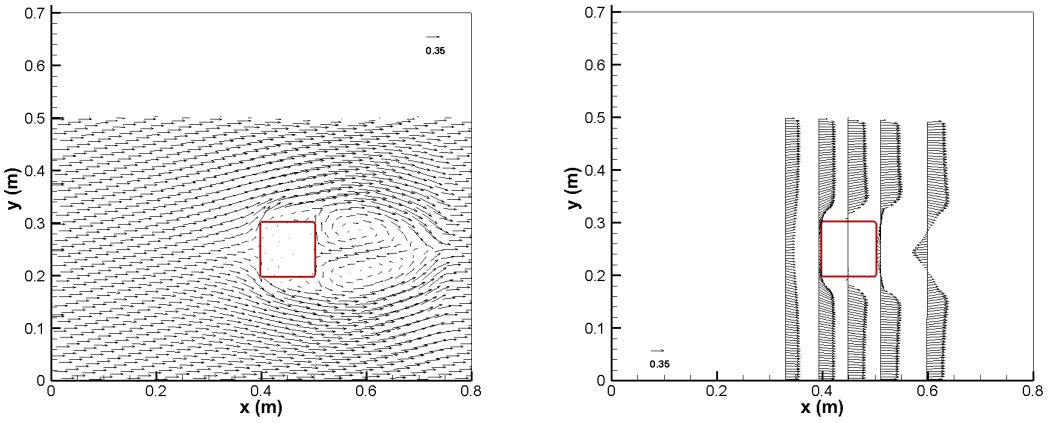

(A) MDL-1 (B) MDL-1

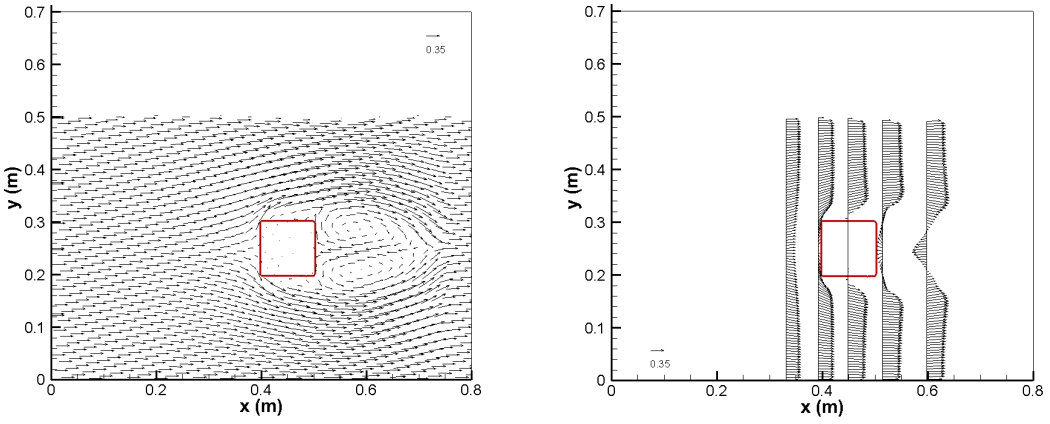

(C) MDL-2 (D) MDL-2

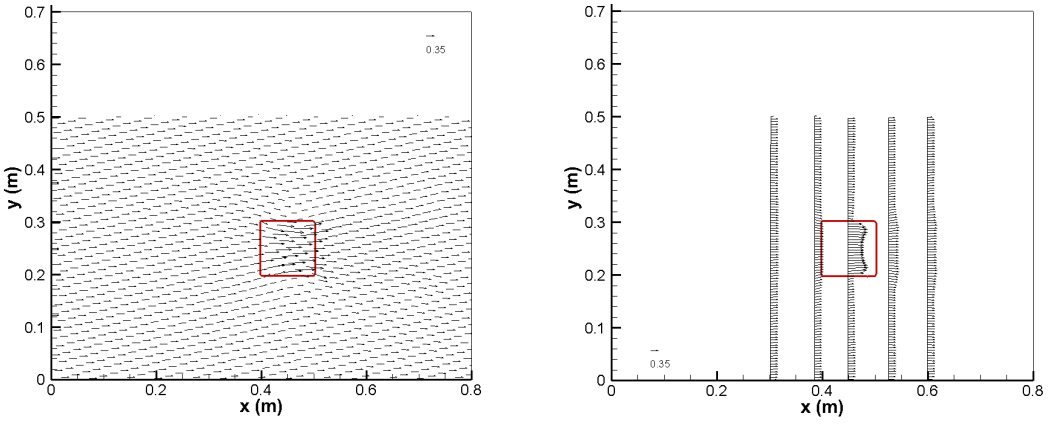

(E) MDL-3 (F) MDL-3

FIGURE 4.3: Velocity vector field (left column) and velocity profiles at selected sections (right column) in Tests MDL. Red line: the boundary of the block.

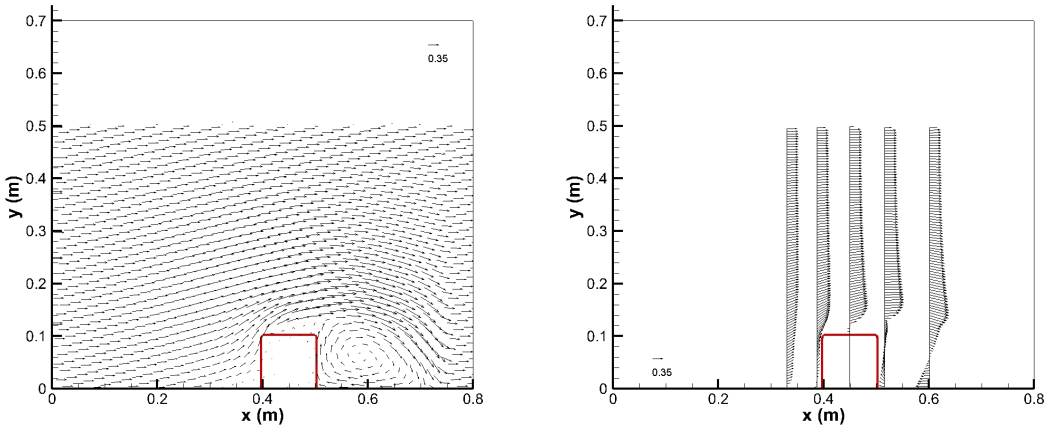

(A) BTM-1 (B) BTM-1

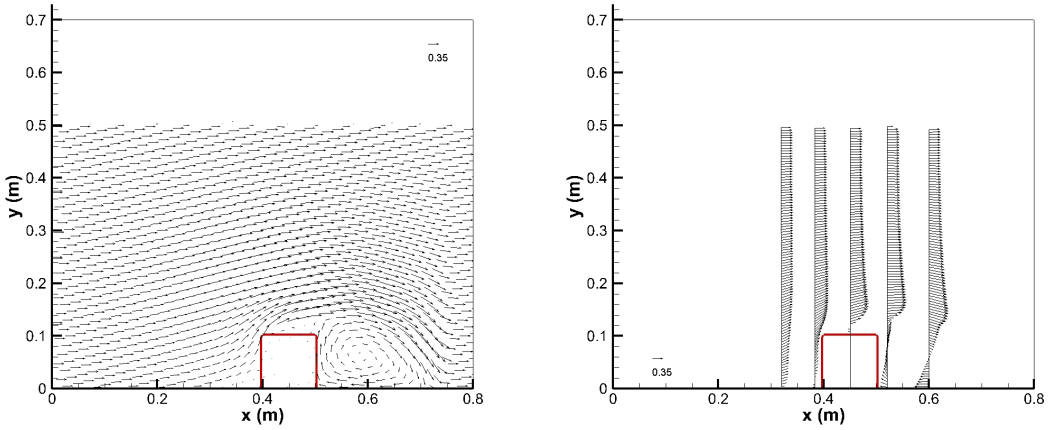

(C) BTM-2 (D) BTM-2

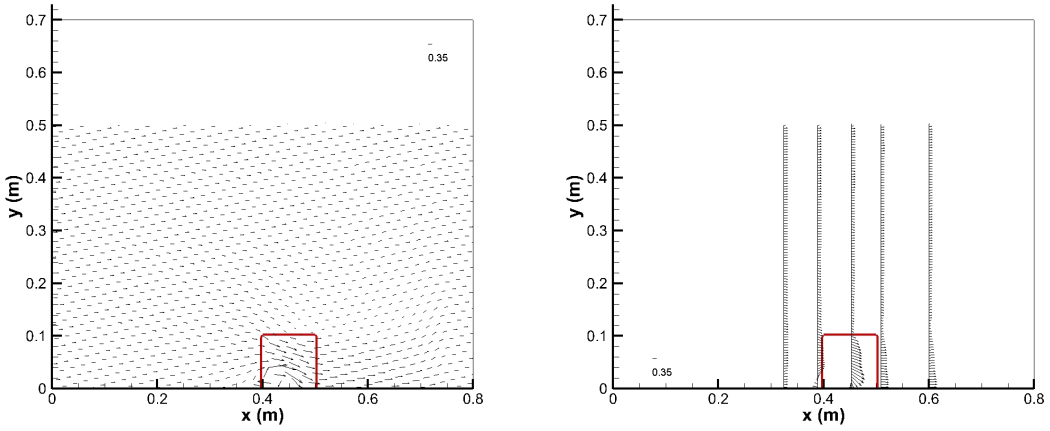

(E) BTM-3 (F) BTM-3

FIGURE 4.4: Velocity vector field (left column) and velocity profiles at selected sections (right column) in Tests BTM. Red line: the boundary of the block.

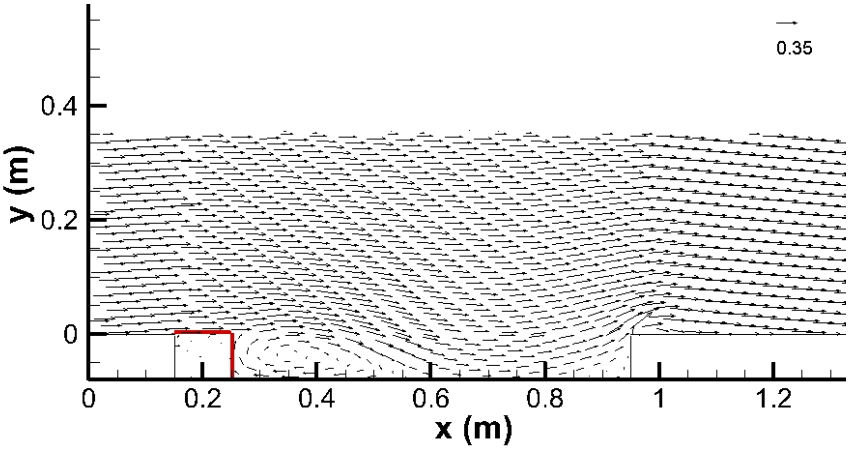

(A) CRN-1

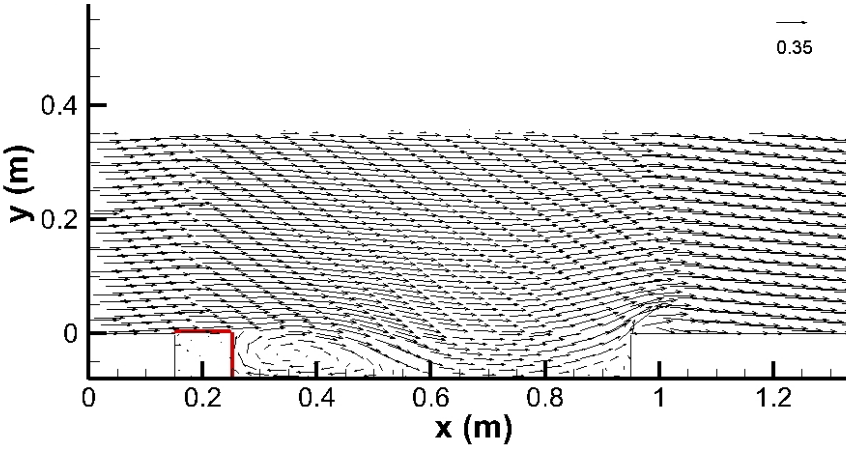

(B) CRN-2

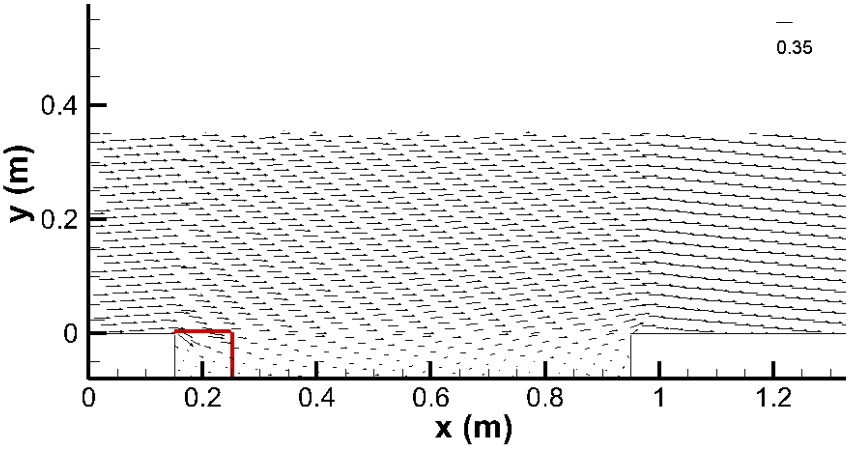

(C) CRN-3

FIGURE 4.5: Velocity vector field in Tests CRN. Red line: the boundary of the block.

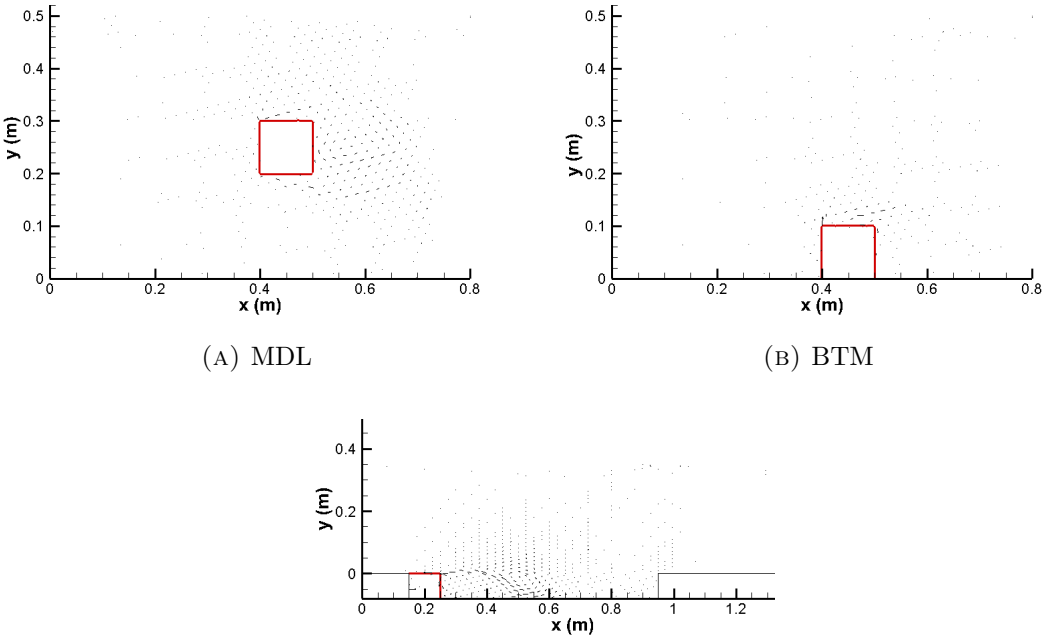

(A) MDL

(B) BTM

(C) CRN

FIGURE 4.6: Velocity difference field. Red line: the boundary of the block.

area, the magnitude of the interphase momentum transfer term is three orders larger than that of the volume exclusion term.

In conclusion, the interphase momentum transfer term decelerates the flow around and inside the particle block as expected. As the fluid volume fraction inside the block is smaller, the effect of the volume exclusion term alone results in water squeezing into the block and getting accelerated there. This is correct mathematically, not realistic physically on its own though. Because the magnitude of the interphase momentum transfer term is several orders larger than that of the volume exclusion term, the overall effect of this two source terms is dominated by the interphase momentum transfer term.

The volume exclusion term is indispensable to compensate for the non-divergence-free flow field caused by the presence of particles. For the two-fluid methodology

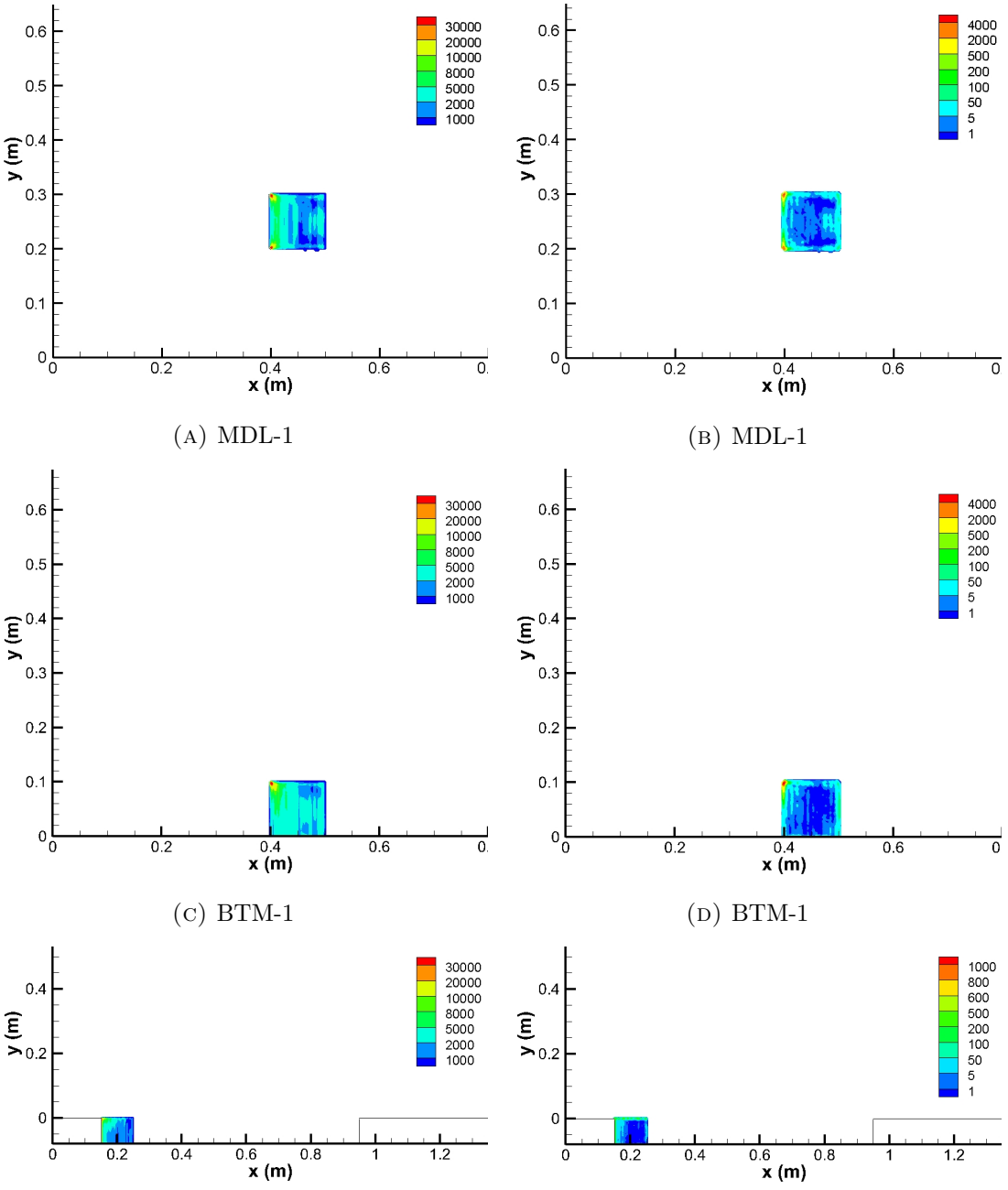

(A) MDL-1 (B) MDL-1

(C) BTM-1 (D) BTM-1

(E) CRN-1 (F) CRN-1

FIGURE 4.7: Magnitude of interphase momentum transfer term (left column) and volume exclusion term (right column).

employed in the hydrodynamic module, zero velocity divergence is satisfied. With the MP-PIC approach coupled with the hydrodynamic module, the density and velocity field of the fluid phase does not implicate any additional elements due to the introduction of particles. Therefore, the fluid phase is still divergence free. For this reason, the volume exclusion term is not a core element to the current model. In addition, considering the unrealistic physical effects and its potential hazard to numerical stability, the volume exclusion term is removed from the model hereafter.

4.4 Extension of the Model Application

The block of particles in the preceding section is fixed in the flow as an immobile structure. Enlightened by this, bespoke particle clusters can be used to represent porous media or complex geometries. As long as the boundary of a structure or geometry is known, the initialiser code as described in Section 3.5.2 can be adapted to generate a cluster of particles or several clusters to represent a structure with specific porosity and geometry. The porosity value can be easily achieved by assigning the desirable solid volume fraction θ_s and the critical solid volume fraction θ_{cs} in the model.

A wedge test is performed as a simple demonstration. The wedge with a porosity of 0.42 is fixed in the flow. Flow gets contracted around the wedge and vortices are formed in the lee-wake side (see Figure 4.8). The magnitude of the interphase momentum transfer term and the volume exclusion term are shown is Figure 4.9.

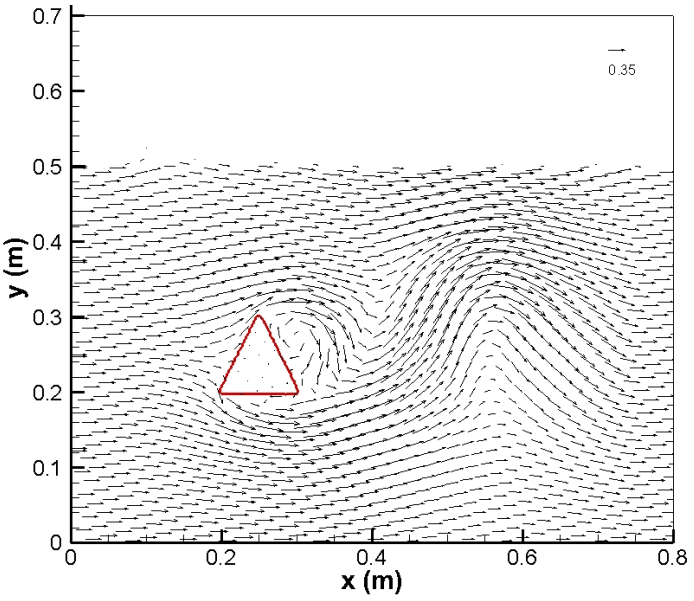

FIGURE 4.8: Velocity vector field. Red line: the boundary of the wedge.

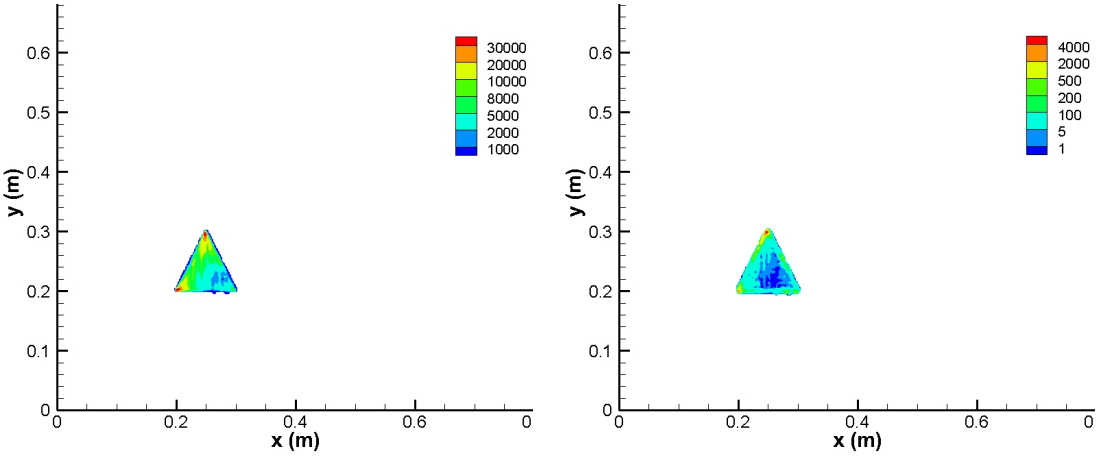

(A) Magnitude of $\mathbf{S}_U$ (B) Magnitude of $\mathbf{T}_{ve}$

FIGURE 4.9: Magnitude of interphase momentum transfer term and volume exclusion term.

The distribution patterns of the magnitude of both source terms resemble those in the isolated block tests. Maximum values of both terms are observed at the upstream corners of the wedge, and the magnitudes inside the wedge are comparable to those in the isolated block tests.

This simple test demonstrates the model's capability to represent rigid structures

in the flow. On top of that, even if a rigid structure involved in the simulation has movement, for example, a turbine blade, the model can be easily modified to accommodate this need by assigning the desired position or velocity to the particles used to represent this structure. The advantage is obvious in this way that no mesh deformation or complex boundary conditions are needed, neither is special treatment or parameterisation for the movement of a structure in the flow as well as the associated requirement on other configurations. In addition, it is also possible to simulate aggregation or dissolution effect of certain structure or materials where applicable. Because particles are traced on a one-to-one basis, they can be introduced or removed as required withoug influencing the rest of the existing particles.

4.5 Conclusions

The particle motion related implementations are calibrated and validated by performing particle falling tests. The modelled particle fall velocity highly agrees with the theoretical value with a discrepancy of only 0.45% and 1.02% for particle $d_{50} = 2.5\ mm$ and $d_{50} = 0.25\ mm$, respectively. Considering numerical accuracy limited by truncated errors etc., this agreement is remarkable. The reliability of the numerical implementation concerning particle motion is confirmed.

For conventional modelling approaches with an Eulerian mesh, the mesh resolution, i.e., the grid size is a typical concern for an accurate prediction of hydrodynamics. On top of that, in the coupled Eulerian-Lagrangian model, the parcel size

is required to be smaller than the grid size. Therefore the ratio of the grid spacing to the parcel diameter needs investigation to ensure a reliable prediction. Particle falling tests with various grid spacing ratios to parcel diameter are performed for this purpose. Considering the predicted particle fall velocity and the behaviour of the interphase momentum transfer term and the volume exclusion term, results show that the larger this size ratio is, the better results are achieved. However, a larger size ratio requires much more parcels in one cell, the number of parcels involved in a simulation can be enormous. Taking into account the limit of computational efficiency as well, the ratio of grid size to parcel diameter is recommended to be between three and four.

The hydrodynamic performance with the influence of the solid phase is examined by a series of isolated block tests. The behaviour of the source terms arisen from the introduction of the solid phase is checked, both inside the computational domain and on the boundaries. The interphase momentum transfer term is the dominant source term. With this term on, the flow deceleration inside the isolated block is significant. Flow accelerates around the block and vortices are formed in the wake side. The volume exclusion term has a very minor effect compared to the interphase momentum transfer term, and is therefore negligible. On its own, this term leads to flow acceleration inside the block due to the gradient of fluid volume fraction. In addition, this term is very sensitive to the size ratio of grid spacing to parcel diameter. As the fluid phase is divergence free, this term is not essential to the model, therefore, it is removed hereafter.

When the particles are fixed, the block of particles behaves as an immobile porous medium. From this perspective, the particle initialiser can be used to generate

clusters of particles to represent porous media, rigid structures or complex geometries. A simple demonstration with a wedge in the flow is presented. Even when the rigid structure has movement or where aggregation and dissolution effect is necessary, the model can be easily extended to account for those effects.

The influences of the Eulerain grid size on the particle motion and potentially the overall transport process demonstrate that the Euler-Lagrange method has certain weak points that need to be treated carefully. However, these challenges are largely due to the numerical implementation methods, including the interpolation method and the solution algorithms, which can be treated with proper numerical method. On the other hand, the Euler-Lagrange method also demonstrates its advantages in dealing with solid obstacles in the flow by grouping a large number of particles. Usually, special treatments have to be employed in the traditional Eulerian approaches to tackle such difficulties, such as mesh masking etc.

Chapter 5

Model Applications

5.1 Introduction

After calibration and validation, the model is applied to a range of experiments in this chapter. The performance of the model regarding the hydrodynamics, sediment transport and scour development will be presented in sequence. Firstly, the model is applied to different hydrodynamic conditions, including steady current and waves. A test of a steady current passing a vertical cylinder by Roulund et al.[70] and a plunging wave breaker experiment by Ting and Kirby[87] are simulated by the model in Section 5.2. Secondly, the model is applied to an oscillatory sheet flow test by O'Donoghue and Wright[56] and O'Donoghue et al.[58] to testify the model's performance regarding sediment transport in Section

5.3.1. Finally, the model is applied to benchmark scour tests in steady current and waves respectively, including a current-induced pipeline scour case by Mao[50] and a wave-induced scour case by Sumer and Fredsøe[78]. Detailed results regarding the hydrodynamics, turbulence structures and scour development will be presented in Section 5.4.

5.2 Hydrodynamics

5.2.1 Vertical Pile under Currents

Roulund et al.[70] conducted a rough rigid bed experiment with a vertical circular pile in a steady current. A pile of a diameter $D = 0.536\ m$ was sealed along its perimeter on a rigid bed covered by a single layer of crushed stones, the roughness height of which was $k = 0.7\ cm$. It was conducted in a 28 m long and 4 m wide flume. The water depth was maintained at 0.54 m. The approach velocity was 0.326 ms^{-1}, which was obtained from the integration of the velocity profile. Only velocity measurements were carried out in this test. The measurements were conducted using a two-component DANTEC "pen-size" laser-Doppler anemometer (LDA) in the plane of symmetry upstream and downstream of the pile. The focal length of the "pen-size" probe with a specially built adaptor was 8 cm. The measurement volume ($d_x \times d_y \times d_z$) was 1.5 mm × 0.12 mm × 0.12 mm[70].

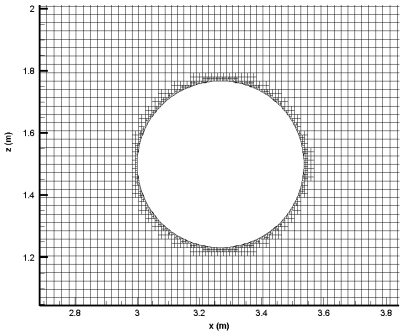

FIGURE 5.1: Refined mesh around the pile.

The model is set up according to the experimental configuration to verify the model's accuracy in the computed hydrodynamics, particularly the flow velocity. The computational domain is 7 m long, 1 m deep, and 3 m wide, consisting of 224, 45 and 112 cells in each direction respectively. The pile is placed in the middle of the domain. Regular grid size varying from 2 cm to 3.125 cm covers the whole domain. Finer mesh down to mm scale is used around the pile (see Figure 5.1) and near the bed. The time step is set at 1×10^{-4} s. Figure 5.2 is a sketch of the computational domain, where water is in red, and air is in blue. A steady current of 0.326 ms^{-1} is imposed on the inlet boundary[29]. Zero normal gradient of the velocity is applied at the outlet boundary. The slip condition is used on the front and back wall. Zero velocity is imposed on the bottom and pile surface. The pressure gradient is calculated according to the velocity such that it provides the correct flux on each boundary. The $k - \varepsilon$ turbulence model is employed. k and ε are set as constant values with a 10% turbulence intensity.

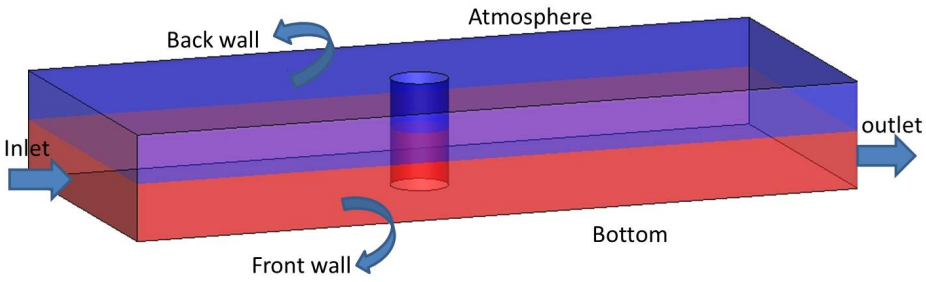

FIGURE 5.2: The computational domain. Red: water; blue: air.

The test starts with a uniform streamwise velocity 0.326 ms^{-1} in the flow. The flow field reaches steady status after $t = 20$ s. Figure 5.3 shows the computed free surface. Only very slight variations are observed around the pile perimeter at the free surface, apart from which, the free surface is level. This is because compared to the computational domain, the pipe diameter is not very large: the computational domain is approximately $13D$ long and $6D$ wide, which is big enough for the flow to adjust to the presence of the pile.

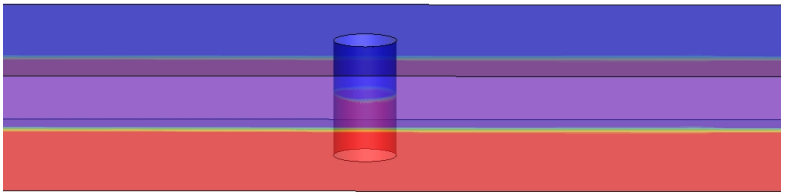

FIGURE 5.3: The developed free surface. Red: water; blue: air.

The streamwise velocity distribution at the free surface, the middle depth of the flow and near the bed surface are presented in Figure 5.4. The flow deceleration in front of the pile and in the wake side, acceleration on the two sides of the pile are captured by the model. At the free surface and the middle depth, the streamwise velocity distribution is similar to each other except that at the middle depth the acceleration zone is even larger, and the deceleration in the immediate wake is stronger. At the bed surface, the acceleration zones on the two sides of the pile shrink into a horseshoe shaped area, while the deceleration areas expand toward both the upstream and the downstream side. Further downstream, not only the flow near the centreline has a lower velocity, two low velocity spots (approximately 0.15 ms^{-1}) are also observed near the front and back wall.

The vertical velocity distribution at these three layers are shown in Figure 5.5. The pattern at each layer is very similar to each other. A downflow is identified at one

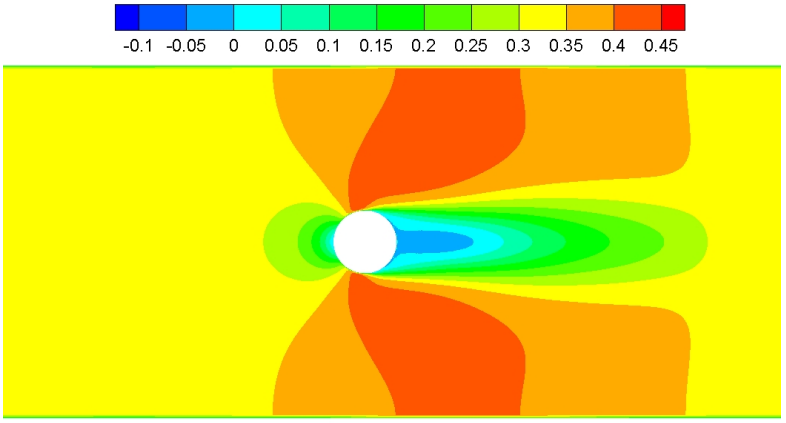

(A) Free surface

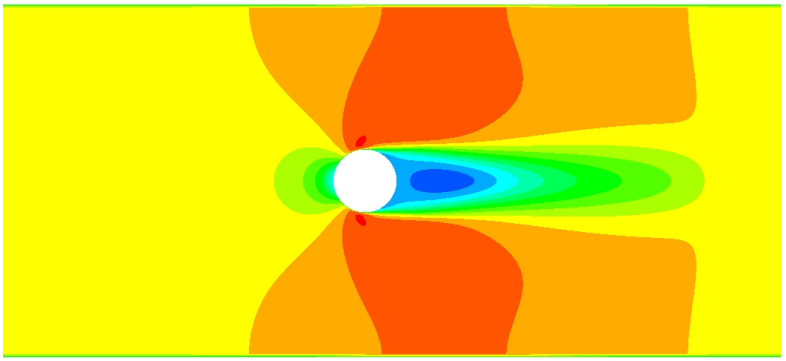

(B) Middle depth

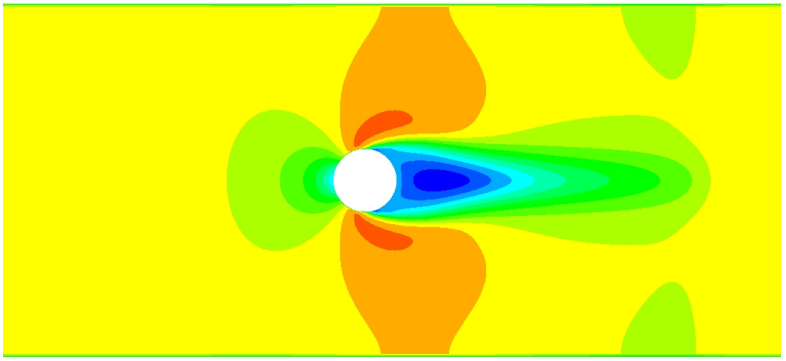

(C) Bed surface

FIGURE 5.4: Streamwise velocity (m/s) distribution at the free surface (A), the middle depth of the flow (B), and near the bed (C).

upstream quarter of the pile perimeter. Correspondingly, on the other upstream side, the vertical velocity is upward. The non-zero regions at the upstream side of the pile expand slightly from the free surface to the bed surface. In the downstream side, two non-zero spots are observed at the middle depth and near the bed surface. The negative velocity spot is on the same streamline as the positive region at the upstream quarter of the pile, and the positive velocity spot aligns with the negative region at the pile perimeter. These two spots are also larger near the bed surface than those at the middle depth.

The streamwise velocity at different vertical layers is presented in Figure 5.6. From top panel to the bottom, the distance from the bed increases. Overall, the modelling results agree with the measurements very well. Particularly, it is seen that the further the layer is away from the bed, the more accurate the modelling results are. The streamwise velocity in front of the pile is predicted accurately at the layer 4.3 cm and above. At layers $z = 1.3$ mm and $z = 2.3$ mm, the predicted velocity between $x/D = -2$ and $x/D = -1$ agrees well with measurements. However, it is over-predicted when approaching the pile, i.e., within $0.5D$ distance from the pile perimeter. The maximum deviation of the modelling results from the measurements is observed at $x/D = -0.87$ with an over-prediction of 0.15 m/s at $z = 1.3$ cm and 0.1 m/s at $z = 2.3$ cm. This can be due to the deficiencies in the boundary condition imposed on the bed surface, for example, the wall function involved in the turbulence model. The grid size being not fine enough near the bed can also be a possible error source. However, the accuracy is considered acceptable in current study considering the challenging situation close to the bed. Apart from that, the deviation of the modelling results stays within 0.01 m/s in most areas, even at locations very close to vertical pile. At the downstream side, the deceleration within $0.5D$ distance from the pile and the acceleration between $1D$ and $2D$ away from pile are all captured very well by the model. Deviations

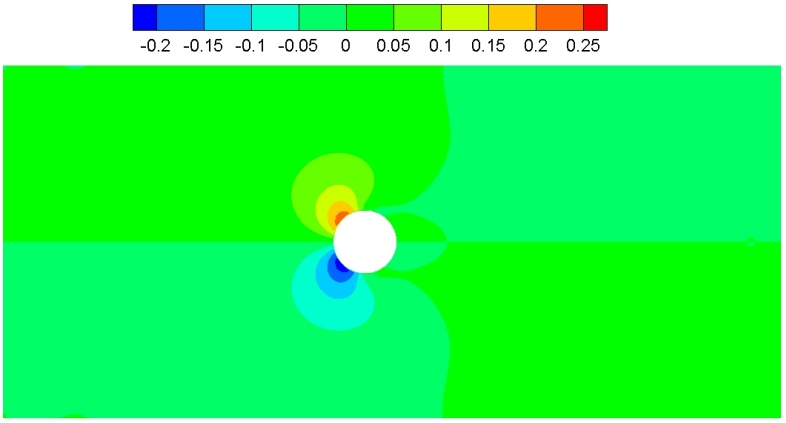

(A) Free surface

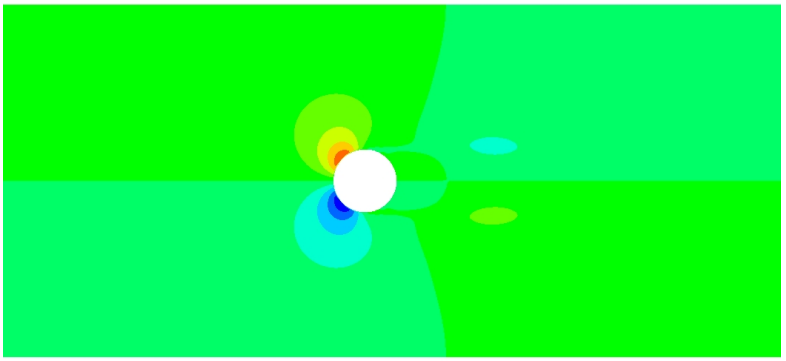

(B) Middle depth

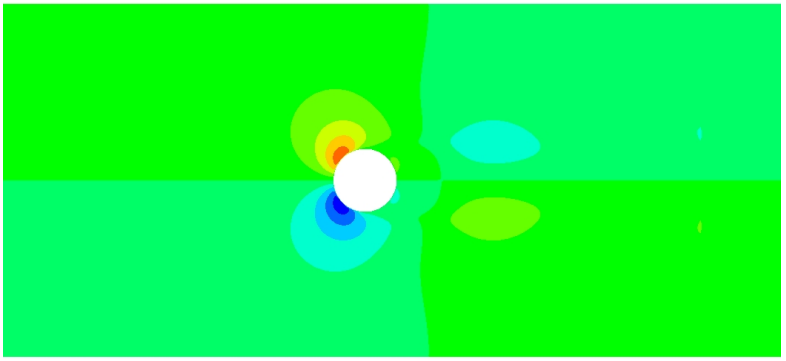

(C) Bed surface

FIGURE 5.5: Vertical velocity (m/s) distribution at the free surface (A), in the middle depth of the flow (B), and near the bed (C).

are mainly less than 0.04 m/s. The good agreement with the measurements at the downstream side is observed at each vertical layer. In the numerical simulation by Roulund et al.[70], the deviations at the downstream side can be larger than 0.06 m/s, which can be caused by the exclusion of the free surface effect in their model. The better results at the downstream side produced by the present model demonstrate well the importance of the free surface effect.

In addition, the three-dimensional feature captured by the model is also seen in Figure 5.6. At the upstream side, the flow deceleration starts at different distances from the pile at each layer. From the bed to the free surface, the beginning point of flow deceleration is observed at approximately $4.5D$, $4D$, $3D$ and gradually converges to $2D$ in front of the pile perimeter. It confirms quantitatively the capability of the model to resolve the full three dimensional features.

The results suggest that the model is able to capture complex flow field around the structure, which is particularly important to the present study. The small deviation from the measurements near the bed surface may potentially affect the particle motion if present. A more delicate treatment of the near wall turbulence could be a solution to further improvement. However, considering the small difference in magnitude, it should not cause significant effects.

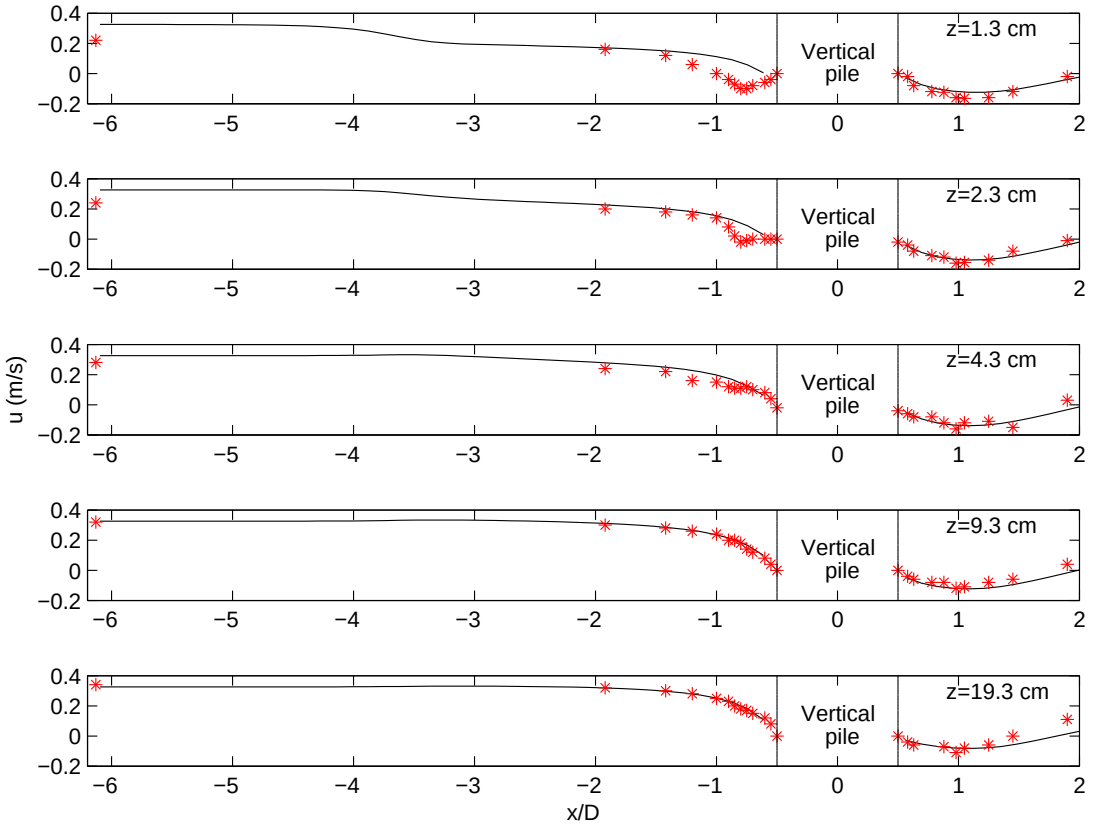

FIGURE 5.6: Streamwise velocity in the plane of symmetry at different vertical layers. The level height z is measured from the bed. Solid line: modelling results; asterisks: measurements.

5.2.2 Plunging Waves Test

To test the model's capacity in dealing with surface variations, the plunging wave breaker experiment by Ting and Kirby[87] is simulated. The experiment was performed in a two-dimensional wave tank, which was 40 m long, 0.6 m wide and 1.0 m deep. A cnoidal wave was generated by a bulkhead wave generator, which was controlled by an electro-hydraulic servo-system, onto a uniform slope of 1 on 35. The wave period was 5.0 s, the wave height was approximately 13 cm in the 10 m long constant-depth region, and the still water depth of which was 0.4 m. A sketch of the experimental arrangement is shown in Figure 5.7. The origin of the abscissa started from the toe of the slope, and the undisturbed still water

level was 0 as shown in Figure 5.7. The water surface elevations and velocities were measured at seven locations along the centreline of the wave tank. Velocities were measured by a two-component fibre-optic laser-Doppler anemometer (LDA). Velocity measurements were obtained by the fibre-optic probe submerged. Owing to the low laser power, only one velocity component could be measured at one time. Therefore, the horizontal and vertical velocities were measured by conducting the same experiment twice. The surface elevation measurements were obtained by capacitance wave gages. Details about the experimental calibration and validation can be found in Ting and Kirby[87].

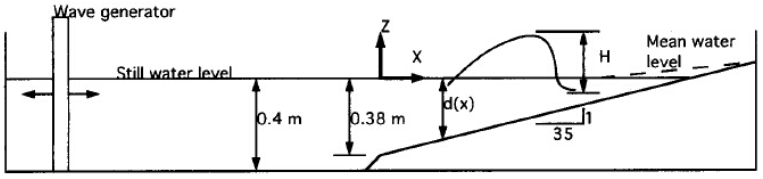

FIGURE 5.7: Experimental set-up of the plunging wave test by Ting and Kirby[87]. (After Ting and Kirby[87].)

The computational domain is 31 m long and 0.7 m deep. The mesh resolution is 1 cm. The time step is 1×10^{-3} s. The still water level rests at $z = 0$ in alignment with the experiment. However, the origin of the abscissa in the model locates at the left beginning point of the computational domain, rather than at the toe of the slope. Necessary shift is made in the results analysis when comparing the modelling results to the measurements. The abscissa in the figures of comparison against measurements corresponds to the experimental set-up, i.e., the origin starts from the toe of the slope. A cnoidal wave is generated[24] according to the experiment. The $k - \omega$ SST turbulence model is employed. The simulation starts from an initially still status as shown in Figure 5.8. The modelling results reach stable status after 28 wave cycles. Therefore, the results hereafter are used below for analysis. Figure 5.9 shows a snapshot of the computed free surface.

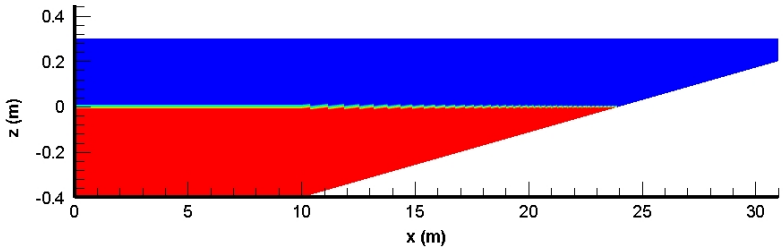

FIGURE 5.8: Computational domain. Red: water; blue: air.

The computed instantaneous free surface elevation and the mean water level are compared to the measured maximum, minimum and mean surface level in Figure 5.10. Very good agreement is achieved by the model overall. In particular, the wave amplitude and the mean water level close to the wave breaking point ($x = 7.795\ m$) agree well with the measurements. The breaking point in the modelling results is slightly further offshore than the measured value. The maximum water surface elevation is slightly over predicted in the surf zone past the breaking point ($x = 10 - 13\ m$), which is very challenging for numerical models. However, it is satisfactory that the deviation of the modelling results from the measurements stays within 2 cm in most areas. The mean water surface elevation agrees very well with the measurements, including the set-down at approximately 7.8 m and the set-up on the beach.

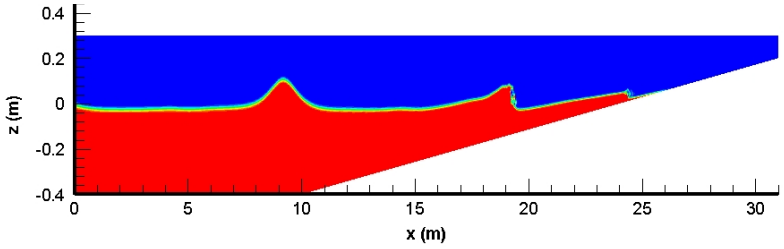

FIGURE 5.9: Snapshot of the computed free surface at $t = 150\ s$. Red: water; blue: air.

The time series of the instantaneous water surface elevation at selected locations are compared with the measurements in Figure 5.11 and Figure 5.12. Overall the agreements of the modelling results with the measurements are achieved. The change in the wave shape from deep water to the breaking point is well predicted

by the model. The performance of the model in the shoaling zone and surf zone is better than that in the breaking zone. The cnoidal wave shape is maintained till $x = 2.0\ m$, and it gradually becomes saw-tooth shaped at $x = 4\ m$. The wave shape at $x = 6\ m$ just before breaking has become fairly asymmetrical. Once past the wave breaking point, the amplitude decreases and the saw-tooth shape is more evident both in the measurements and the modelling results (see Figure 5.12). Only at locations immediately past the breaking point, i.e., $x = 8.0\ m$ and $x = 9.0\ m$, the maximum water elevation is under predicted by the model. This can be due to the lack of additional numerical schemes to deal with wave breaking and reflection among others in the model, while these processes are implicated in the laboratory measurements. Considering the complex nature of wave breaking and the challenges in resolving the surface variation associated with the complex transition in wave dynamics, such results are clearly satisfactory.

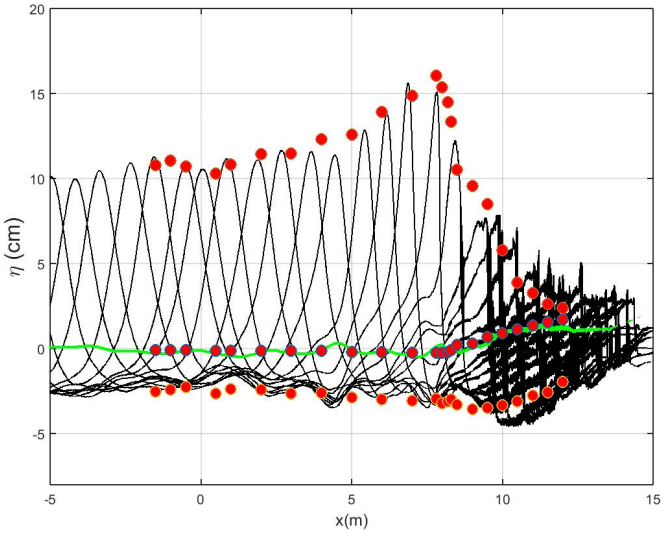

FIGURE 5.10: Distribution of the wave amplitudes and the mean water surface elevation. Black lines: modelling results; green line: computed mean water level; dots: measurements.

Figure 5.13 shows the time averaged horizontal velocity profile at selected sections. The horizontal axis in this figure is the normalised undertow by the wave celerity $\sqrt{gh}$. The vertical axis is the surface elevation normalised by the local mean water

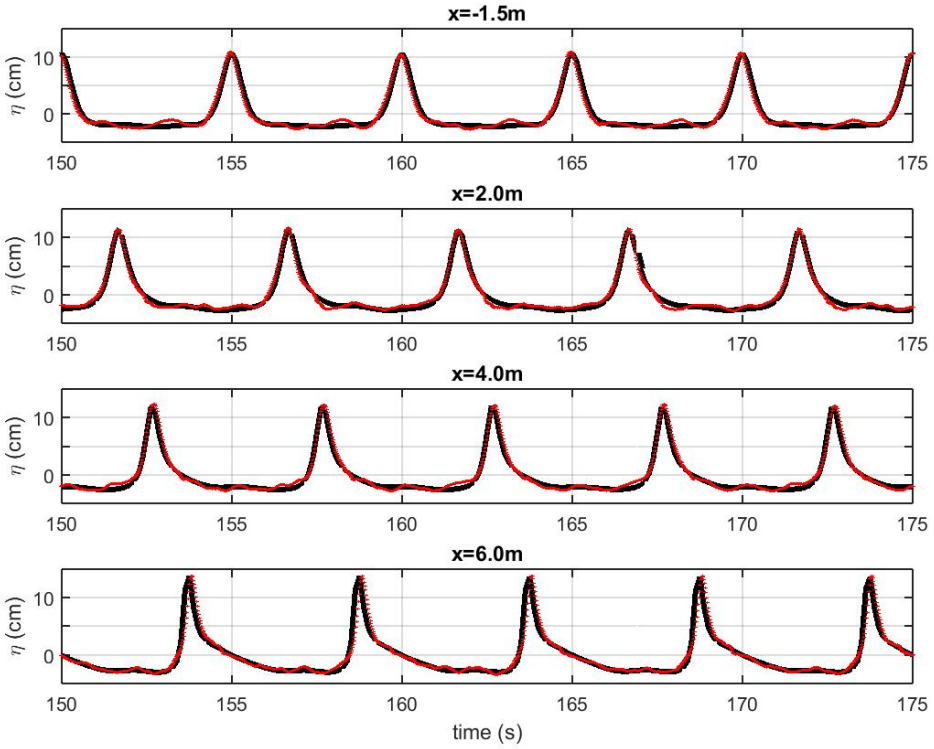

FIGURE 5.11: Time series of the water surface elevation at selected sections (Part I). Black: modelling results; red: measurements.

depth h. Good agreement with the measurements is achieved generally. At the wave breaking point, the variation of the undertow current with depth is virtually constant as seen in both the measurements and the modelling results. Further past the breaking point, the maximum undertow current is formed near the bottom. The computed velocity magnitude agrees well with the measurements especially close to the bottom layer. Deviations are observed close to the free surface, where the instability of surface waves causes large uncertainly in the modelling results. The linearisation of the governing equations and the second-order accuracy of the numerical scheme may result in numerical errors especially in the case of a plunging wave where highly non-linearity exists.

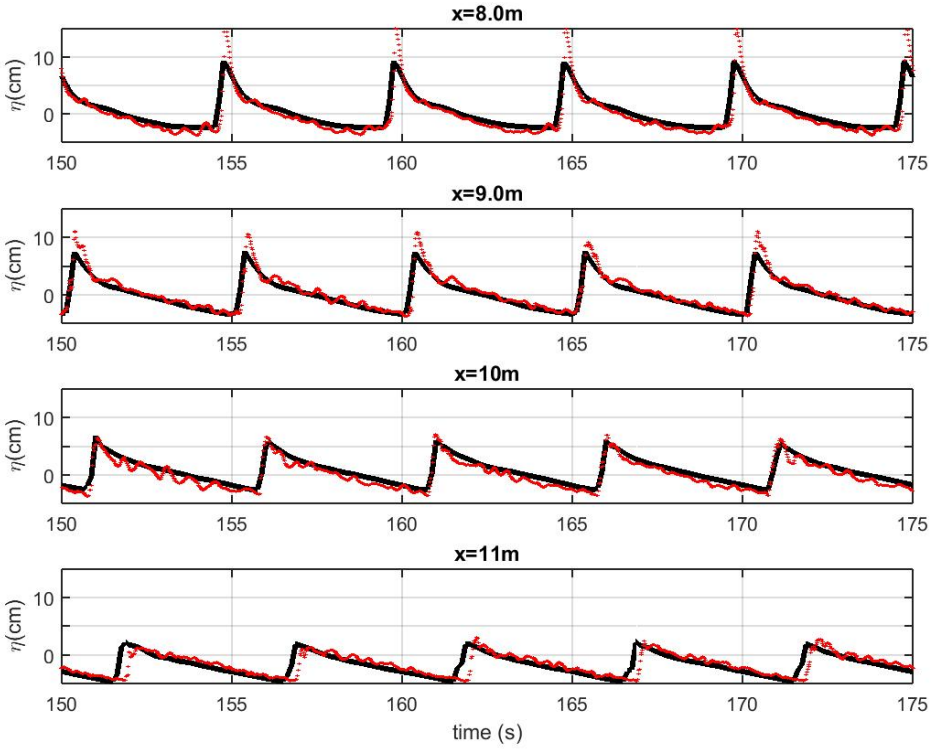

FIGURE 5.12: Time series of the water surface elevation at selected sections (Part II). Black: modelling results; red: measurements.

The variation of the phase-averaged normalised surface elevation η by depth, normalised horizontal velocity $\overline{u}$ by wave celerity, normalised vertical velocity $\overline{w}$ by wave celerity, and normalised turbulent kinetic energy k by wave celerity at selected locations at and past the wave breaking point are shown in Figure 5.14 and Figure 5.15. On the top panel of both figures, the computed surface elevation is compared with the measurement; particularly at $N6$ and $N7$, the agreements are very good. At the breaking point $N2$ and the immediate downstream $N4$, the maximum surface elevation is under predicted as already shown in the preceding figures. The computed horizontal velocity and vertical velocity are in good agreement with the measurements at the four locations, small deviations are observed though. The horizontal velocity dominates the flow speed apparently, and the vertical velocity are fairly small except when the wave crest passes. The normalised turbulent kinetic energy is over predicted at the breaking point $N2$, whereas the

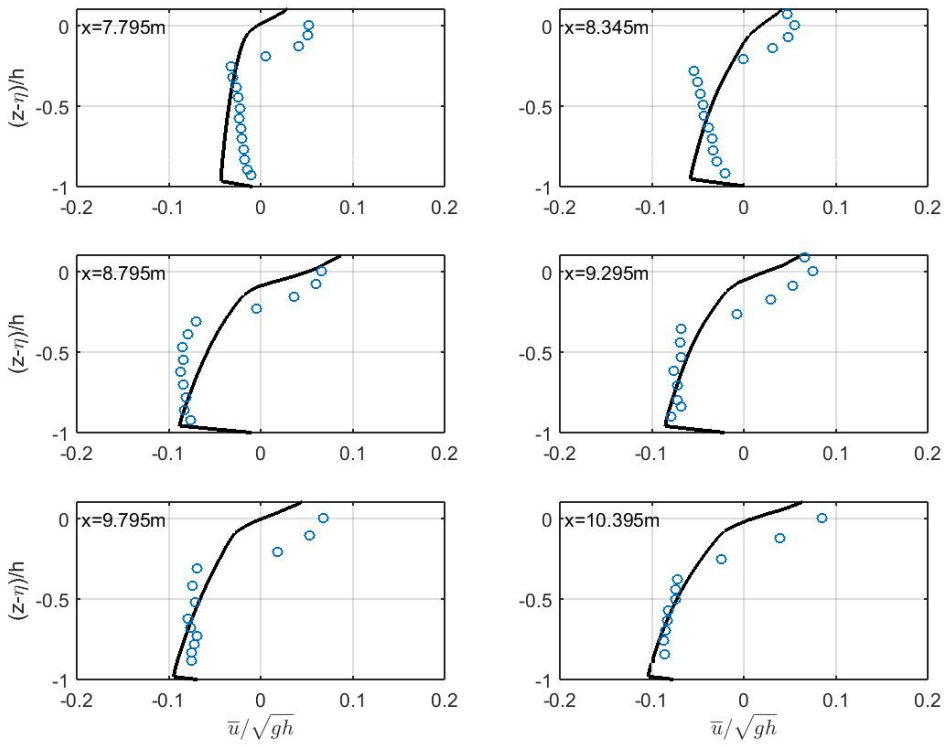

FIGURE 5.13: Time-averaged horizontal velocity ($\overline{u}$) profile at selected sections. Lines: modelling results; circles: measurements.

prediction improves farther downstream. Nevertheless, the overall agreements are considered satisfactory.

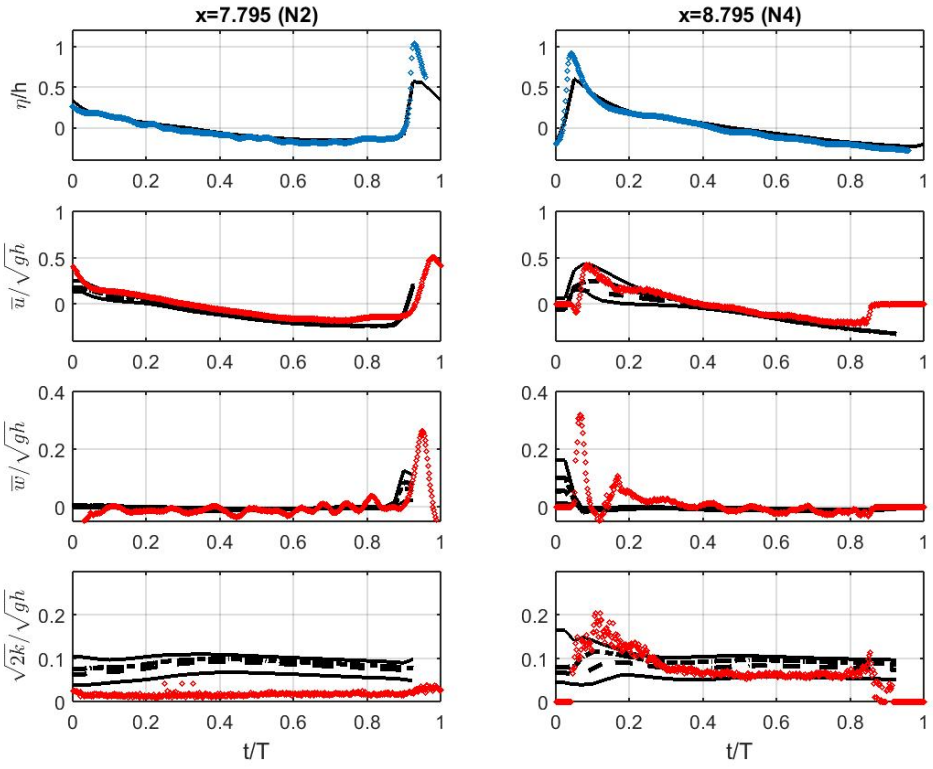

FIGURE 5.14: Phase-averaged surface elevation η, horizontal velocity $\overline{u}$, vertical velocity $\overline{w}$, and turbulent kinetic energy k at selected sections (Part I). Black: modelling results; red: measurements.

5.3 Sediment Transport

5.3.1 Sheet Flow Test

The sediment transport under oscillatory sheet flow is a challenging yet important topic in coastal engineering. The near-bed sediment transport under waves is largely determined by the sand size and the near-bed oscillatory flow caused by waves[58].

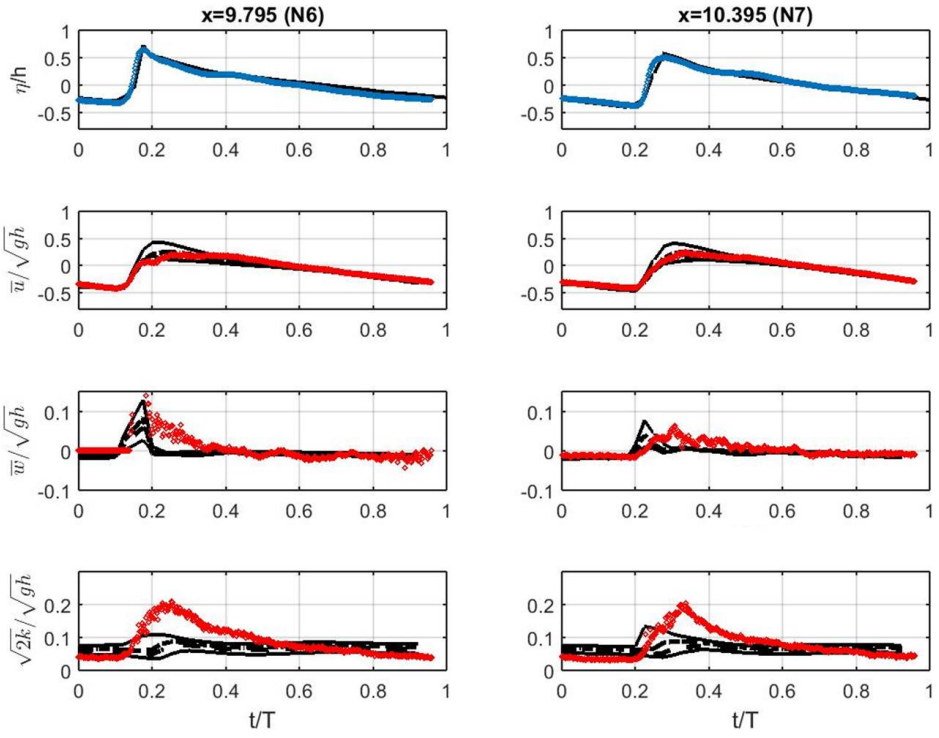

FIGURE 5.15: Phase-averaged surface elevation η, horizontal velocity $\overline{u}$, vertical velocity $\overline{w}$, and turbulent kinetic energy k at selected sections (Part II). Black: modelling results; red: measurements.

The model is applied to a case with fine sand under sinusoidal oscillatory flow condition. The experiment was performed by O'Donoghue and Wright[57] in the Aberdeen Oscillatory Flow Tunnel. It was 16 m long with a 10 m long glass-sided rectangular test section, 0.75 m high and 0.3 m wide. A 250 mm deep bed of well sorted sand with the median grain size 0.13 mm was placed in the central part of the test section. A sinusoidal oscillatory flow was generated with a period of 6 s and an orbital amplitude of 1.2 m. The flow velocity was measured by an ultrasonic velocity profiler (UVP), which was capable to collect data from several millimetres to approximately 50 mm above the instantaneous bed level. The sediment concentration below the initial bed level was measured by three conductivity concentration meters (CCMs) placed at separate locations along the central line of the tunnel[44]. More details can be found in O'Donoghue and Wright[57] and Li et al.[44].

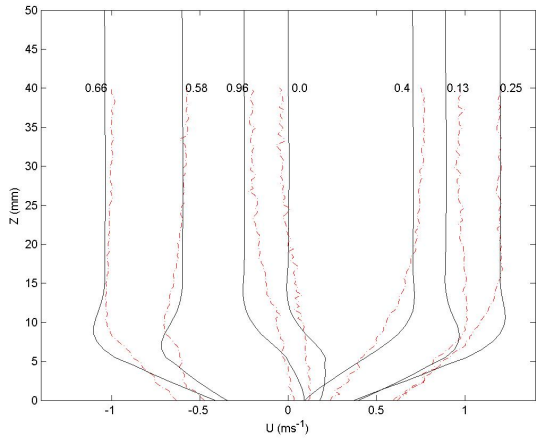

FIGURE 5.16: The velocity profile at selected phases. t/T = 0.0, 0.13, 0.25, 0.4, 0.58, 0.66, and 0.96 as indicated in the figure by each line. Black solid lines: modelling results; red dashed lines: measurements.

The computational domain is set as 100 mm long, 100 mm high, and one cell wide. The mesh resolution is 1 mm. The time step is 1×10^{-3} s. A sand layer of 10 mm is placed on the bottom initially, and the maximum volume concentration is 0.6. Periodic boundary conditions are employed at the inlet and outlet boundaries for both the fluid phase and the solid phase. To save computational costs, a typical boundary modelling approach is adopted, i.e., an oscillatory body force is used to represent the wave induced pressure term in the flow momentum and this force is assumed to be uniformly distributed across the depth. The oscillatory force term is tuned to meet the experimental set-up. The $k-$equation large eddy simulation is adopted. The flow starts from an initially stationary status. The simulation reaches stable status after 60 wave cycles and the results hereafter are found converged to be periodical and therefore are used for analysis.

The computed flow velocity profile at selected phases are compared with the measurements in Figure 5.16. Overall the agreement between the computed and measured velocity is encouraging. In particular, the velocity profile 15 mm above

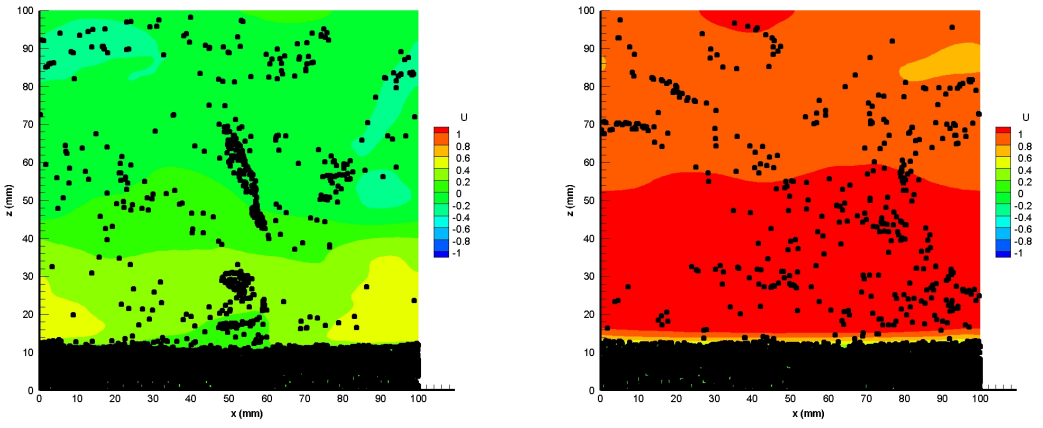

(A) $t/T = 0$ (B) $t/T = 1/6$

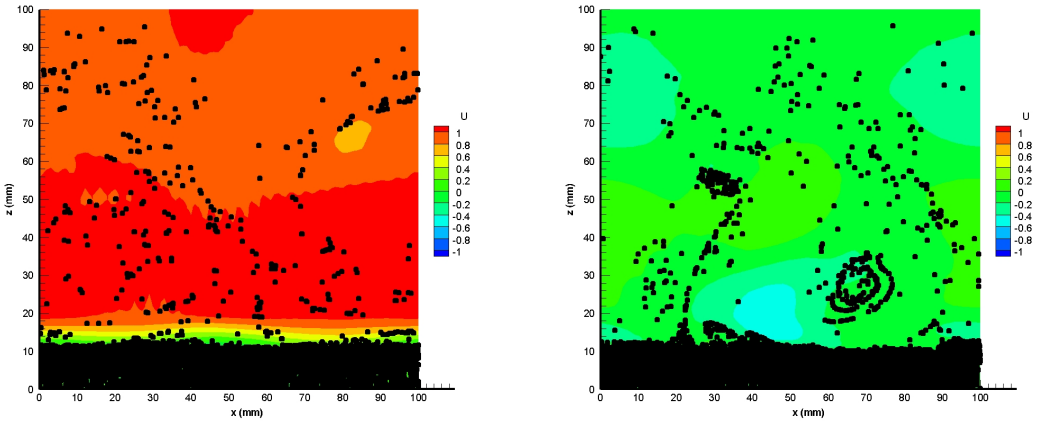

(C) $t/T = 1/3$ (D) $t/T = 1/2$

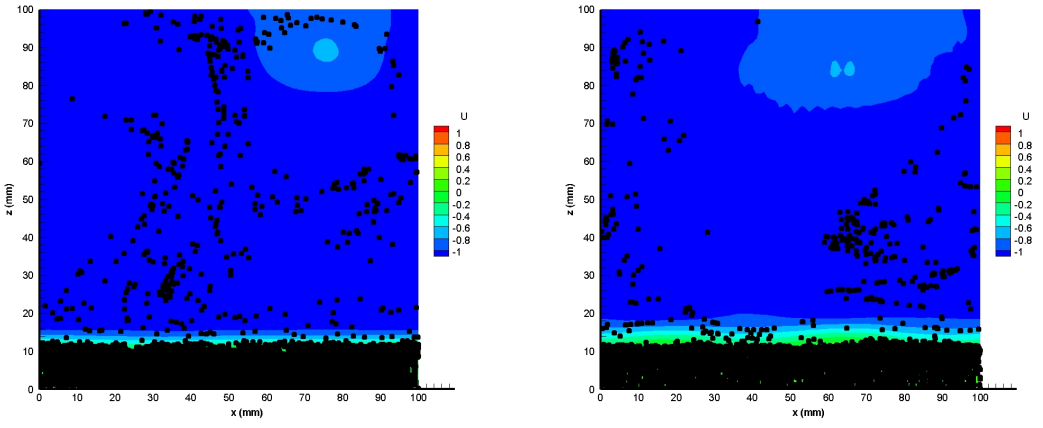

(E) $t/T = 2/3$ (F) $t/T = 5/6$

FIGURE 5.17: Particle distribution and streamwise velocity at selected phases.

the sandy bed reaches better agreement with the measurements than that below this level. The phase lead between the flow in the boundary layer and the outer flow is also captured by the model very well. When approaching peak flow ($t/T = 0.25, 0.66$) and during maximum acceleration ($t/T = 0.13, 0.58$), the agreement is better with the measurements than at flow reversal ($t/T = 0.96$). Most deviations are observed in the region close to the bed, where significant changes occur to the hydrodynamics due to the wave boundary layer process and the sheet flow process.

Employing a particle approach, the model is able to resolve the sand motion at the particle scale. Figure 5.17 shows the particle distribution and the streamwise velocity at selected phases. The velocity contour is generally uniform up in the water column with variations locally. The velocity decreases when approaching the bed. A layered velocity distribution immediately above the bed, i.e., $z = 10 - 15$ mm is observed throughout the flow cycle. It is particularly obvious at peak flow (see Figure 5.17b, 5.17c, 5.17e and 5.17f). It demonstrates that the influence of the sandy bed on the flow is well resolved by the model. The particle distribution at peak flow is widespread over the whole water column due to the strong suspension. At flow reversal, particles are entrained high into the water column, and a vortex-shaped distribution is observed in Figure 5.17a and Figure 5.17d. It is noteworthy that Figure 5.17 is the instantaneous particle distribution at selected phases, and the ensemble averaged values are used for comparison against measurements.

To examine the modelling results on sediment motion, the computed sediment concentration profiles are obtained by averaging those values over the length of the computational domain. The sediment concentration profiles at selected phases are compared to the measurements in Figure 5.18 and 5.19. Overall, very good

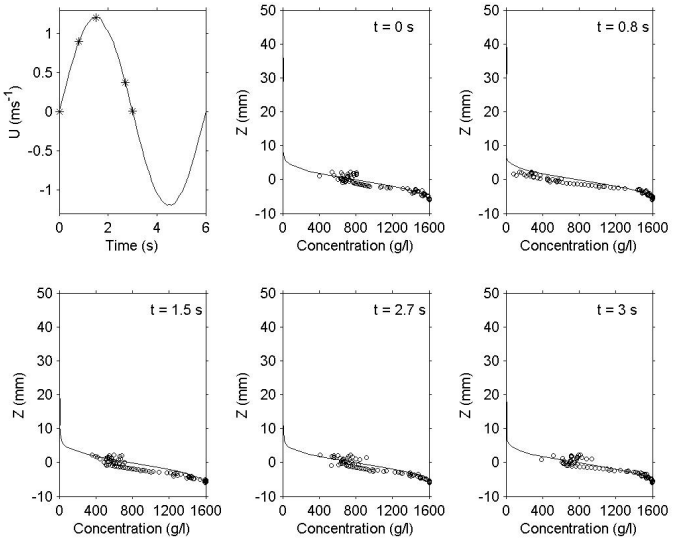

FIGURE 5.18: Comparison of the computed and measured sediment concentration at various flow phases in the first half of a wave cycle. Lines: modelling results; circles: measurements.

agreement is achieved between the computed and measured value, from the high concentration region deep inside the bed up to the low concentration region higher in the water column. However, certain deviations are observed near the bed surface, where the deviation can be as large as 500 g/l. It can be caused by the inaccurately resolved flow velocity there, as well as the challenging situation regarding the active interaction between the flow the sediment dynamics at the bed surface. At layers 1 mm deep in the bed and below, the predicted sediment concentration is much better, suggesting the model's good performance in dealing with a nearly fully packed bed. Also, it can be seen that the model is able to simulate the acceleration induced suspension near the bed, i.e., from $t = 0$ to $t = 1.5$ s. The erosion inside the bed is evident and the concentration curve becomes steeper. In the deceleration phase, sediment is settling down with the rise of bed level and the concentration curve becoming less steep ($t = 2.7$ s and $t = 3$ s). Both the magnitude and the trend of the concentration agree with the measurements very well, indicating the capability of the model in simulating the particle interaction at very high concentration level.

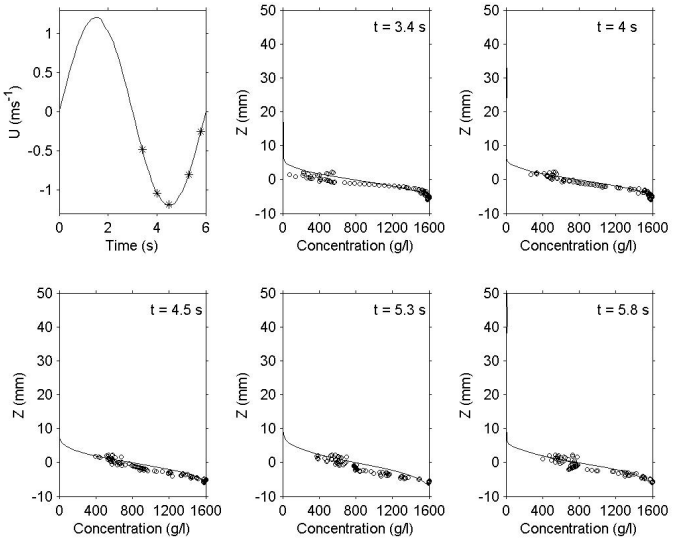

FIGURE 5.19: Comparison of the computed and measured sediment concentration at various flow phases in the second half of a wave cycle. Lines: modelling results; circles: measurements.

5.4 Scour Studies

5.4.1 Current-Induced Pipeline Scour

The model is applied to a current-induced live-bed scour case around a pipeline, a benchmark laboratory test carried out by Mao[50]. In the experiment, the flume was 23 m long, 0.5 m deep, and 2 m wide [98]. The water depth was 0.35 m, and a pipeline of a diameter $D = 0.1$ m was placed above a sand layer. The particle median grain size was 0.36 mm. In this selected live-bed scour case, the Shields number $\theta = 0.098$ and the mean flow velocity was 0.5 ms^{-1}.

The computational domain is set as 1.6 m long, 0.5 m deep and one cell wide.

The mesh resolution is 5 mm. The inlet boundary is on the l.h.s. of the domain and the outlet boundary is in the r.h.s. as sketched in Figure 3.2. The simulation starts with a uniform flow velocity of 0.5 ms^{-1}. The time step is 2×10^{-4} s. The $k-$equation large eddy simulation is adopted to resolve the turbulence structures. The simulation starts with clear water and a uniform flow velocity of 0.5 ms^{-1}.

Flow Field

The computed flow velocity field at $t = 1.5$ min is shown in Figure 5.20, where the bed is coloured in red. Overall the computed flow field is fairly realistic. The flow field $1D$ above the bed at the upstream side remains undisturbed by large. Below this level, the flow field is influenced by the presence of the pipe and sediment particles remarkably. Small eddies are generated close to the bed surface and near the downstream scour hole. Close to the pipe, the flow acceleration around the pipe is well captured by the model. At the downstream side, the recirculation zone immediately behind the pipe and two small cavities between the flow acceleration zone and the recirculation zone are also captured clearly. The lee-wake vortices are formed behind the recirculation zone. The flow field immediately above the bed is resolved vigorously as well. At the upstream side, small vortices are generated and developed along the streamwise direction. The flow velocity magnitude immediately above the bed is small because the particles act as a momentum sink. At $t = 1.5$ min, the scour hole underneath the pipe has already formed a well-shaped pathway for the flow. Therefore, the flow acceleration between the bed and the pipe develops without much obstacles. The acceleration jet propagates to around $2D$ behind the pipe and encounters the flow from above the pipe. Consequently, the lee-wake vortices take place and propagate further

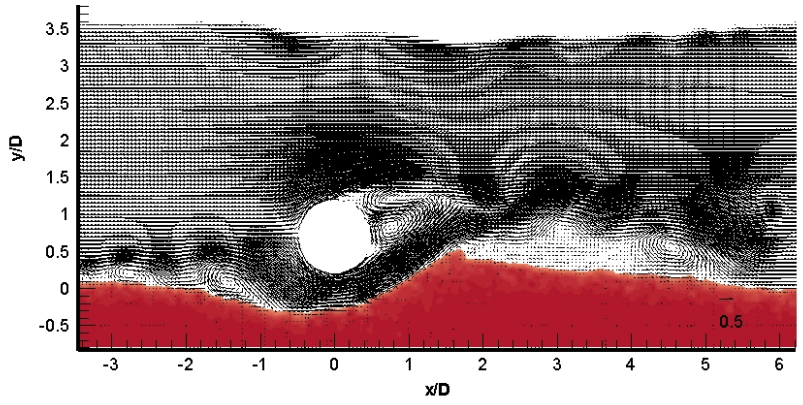

FIGURE 5.20: Computed flow velocity field at $t = 1.5\ min$.

downstream. Between the lee-wake vortices and the bed, the flow is decelerated by the bed, especially past the mount shaped at $x = 1.8D$.

Also we can see that the free surface is no longer level at the initial water depth. Due to the flow acceleration and lee-wake vortices caused by the pipe, the water level decreases from $x = -1D$ and fluctuates in the downstream side. By resolving the free surface, the internal flow field can adjust more realistically and timely to the bed profile development.

The velocity profile at six selected sections located upstream, across the pipe, and downstream of the pipe are shown in Figure 5.21 along with the streamwise velocity field. The overall pattern of the streamwise velocity field resembles each other at the selected time. From $t = 80\ s$ to $t = 100\ s$, the bed underneath the pipe and the slope in the downstream side are being eroded continually. However, no dramatic change is observed in the bed profile. Therefore, the flow filed is relatively stable during this period. Flow is decelerated in front of the pipe, and gets accelerated below and above the pipe. A recirculation zone is observed with reversed flow immediately behind the pipe. Further downstream, the high velocity region and

reverse velocity region caused by the lee-wake vortices evolve downstream with time.

At the upstream, two high velocity regions are observed approximately $0.5D$ above the bed. The size and location of these two regions evolve with time. Apart from that, the flow field is relatively uniform. Correspondingly, the velocity profiles at the selected upstream locations are generally constant with depth; only slight overshoot can be found in the high velocity region. Underneath and above the pipe, the velocity acceleration is evident. The velocity magnitude at the section across the pipe sees larger values than the upstream ones, and it peaks close to the pipe. In the downstream side, influenced by the recirculation zone and the downstream mount, the velocity profile at $x = 1.5D$ produces almost zero velocity at $y = 1D$, from which depth downwards, it accelerates and then decelerates again when approaching the bed. Further downstream, the velocity profile at $x = 3D$ and $x = 4.5D$ have small velocity magnitude even $1D$ above the bed due to the presence of the lee-wake vortices there. Because of the evolution of the lee-wake vortices with time, these two velocity profiles are more variant with time compared to those at the other sections.

The computed vorticity magnitude at $t = 1.5\ min$ is shown in Figure 5.22. High vorticity is observed at the free surface, along the bed surface, around the pipe and in the lee-wake vortices region. The free surface above the pipe and in the downstream side has larger vorticity than that in the upstream side. By contrast, along the bed surface, the vorticity in the upstream is larger than that behind the downstream mount ($x = 2D - 5D$) because the lee-wake vortices are higher above the bed as seen in Figure 5.20. The acceleration zone around the pipe, the recirculation zone in the immediate downstream, and the lee-wake vortices region

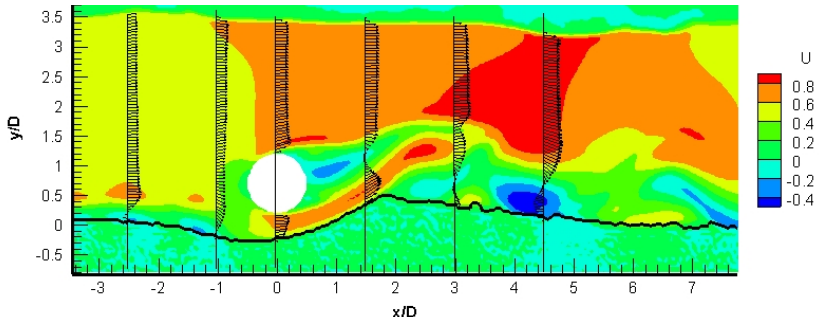

(A) $t = 80\ s$

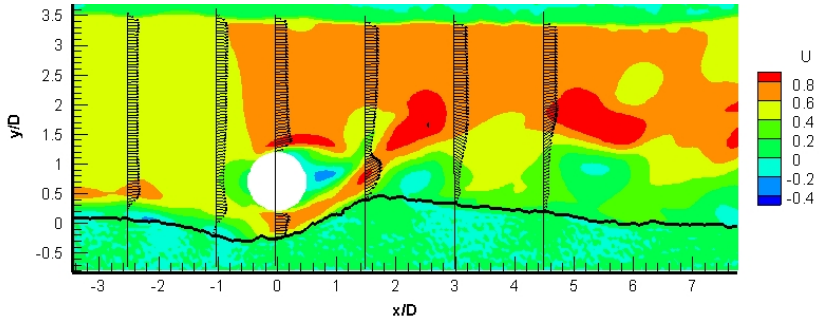

(B) $t = 85\ s$

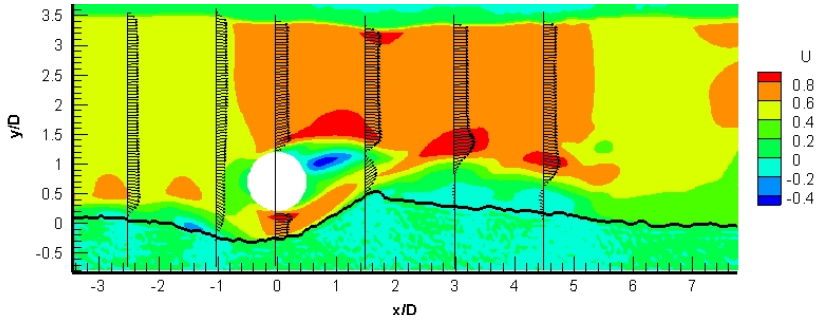

(C) $t = 90\ s$

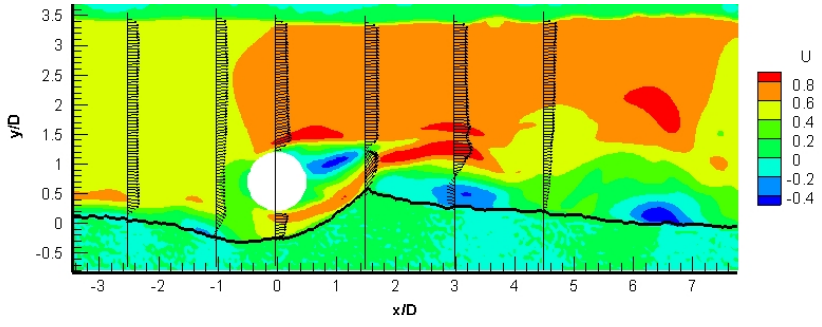

(D) $t = 95\ s$

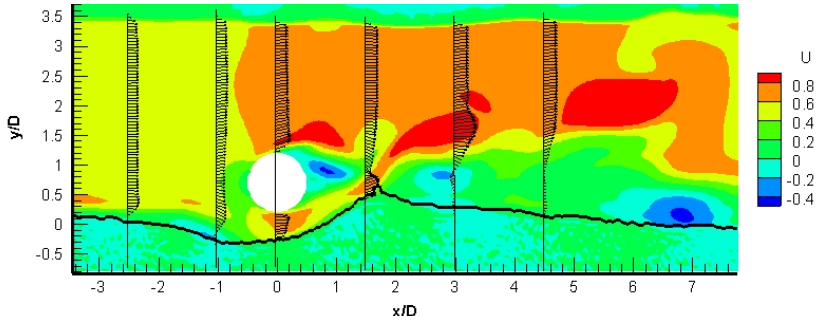

(E) $t = 100\ s$

FIGURE 5.21: Streamwise velocity and velocity profile at selected sections. Bold solid line: bed profile.

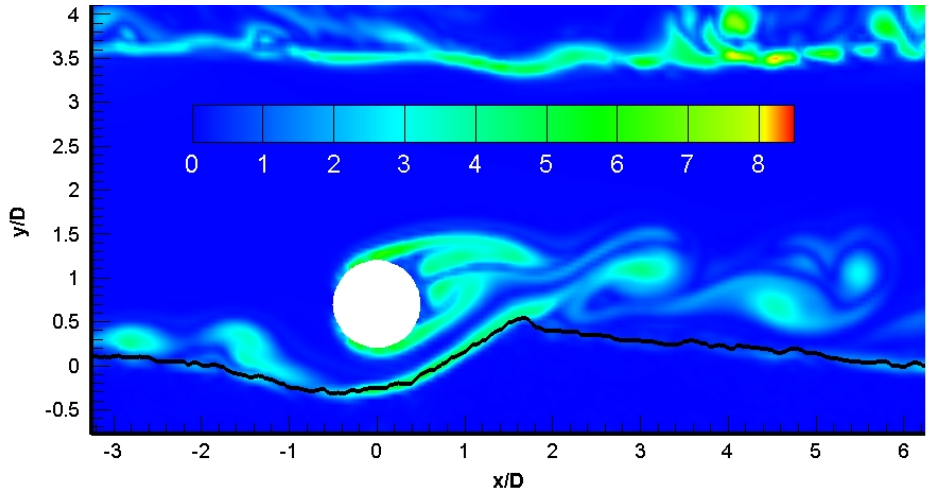

FIGURE 5.22: Vorticity magnitude at $t = 1.5\ min$. Bold solid line: bed profile.

have large vorticity as expected. It is noteworthy that the low vorticity in the small cavities between the recirculation zone and the pipe is also reproduced by the model.

Turbulence Structures

The computed sub-grid scale kinetic energy and sub-grid scale eddy viscosity are presented in Figure 5.23. It is clear that the sub-grid scale kinetic energy is more intense on the two sides of the pipe as shown in Figure 5.23a. The high value region below the pipe is larger than that above the pipe, suggesting a higher turbulence energy generation below the pipe. Along the bed surface at the upstream side, higher values of sub-grid scale kinetic energy than the majority water body are observed, and the high value region extends to the downstream side of the scour hole. The free surface downstream of the pipe also has a larger turbulence kinetic energy than the upstream side, suggesting the impact of the pipe and variation in the bed surface elevation on the free surface. In Figure 5.23b, the high value region

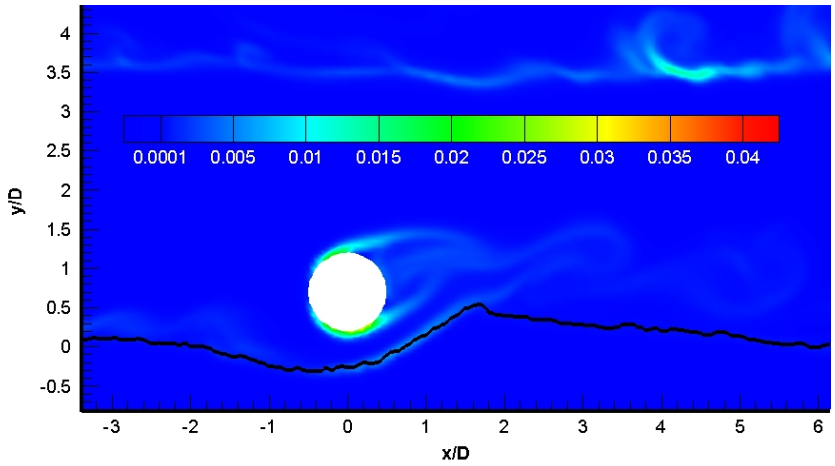

(A) Sub-grid-scale kinetic energy

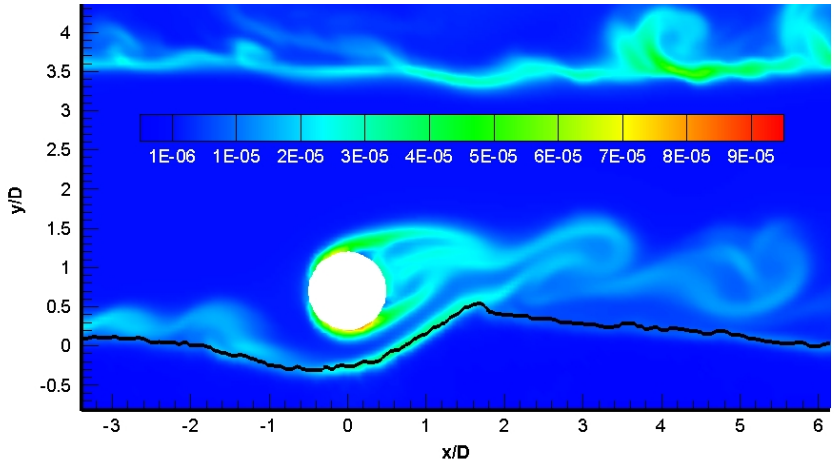

(B) Sub-grid scale eddy viscosity

FIGURE 5.23: Sub-grid scale kinetic energy and sub-grid scale eddy viscosity at $t = 1.5\ min$. Bold solid line: bed profile.

of sub-grid scale eddy viscosity can be found close to the bed surface, around the pipe perimeter, in the recirculation zone behind the pipe, in the location of lee-wake vortices, and at the free surface, which all overlap with the high vorticity regions as seen in Figure 5.22. These regions are also where particle motions are very active as will be shown in Figure 5.25. The high vorticity, high turbulence kinetic energy and eddy viscosity in those regions are good indicators for active particle motions, i.e., they can be the drive to facilitate particle motion, especially the particle entrainment. Once being picked up from the bed, particles in these regions can then be transported downstream quickly due to the strong flow velocity.

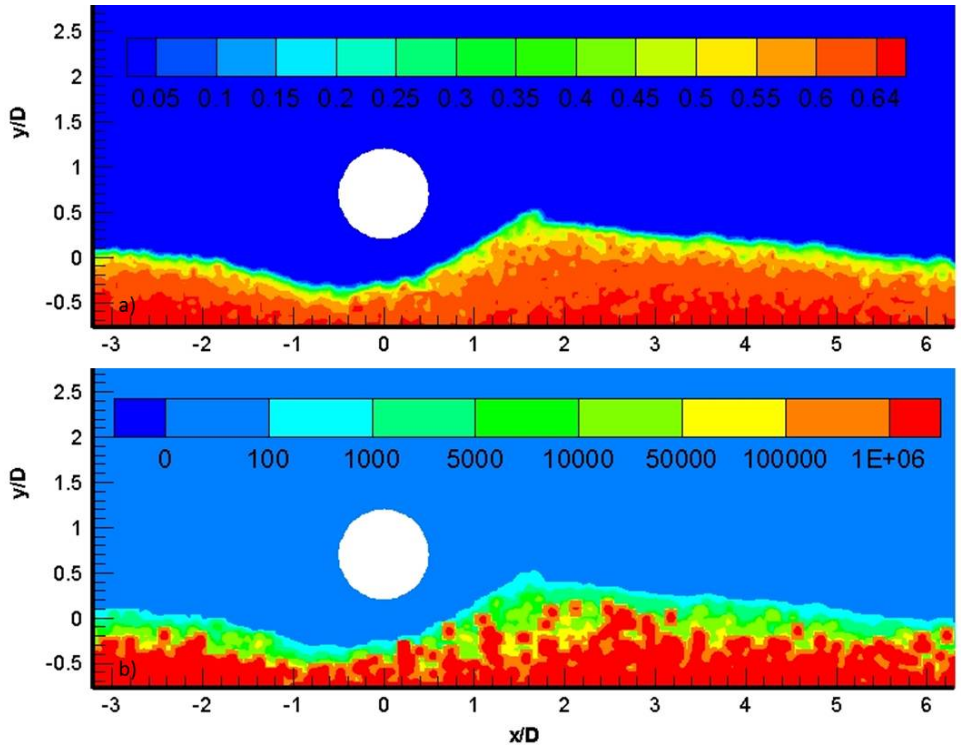

FIGURE 5.24: Contour of solid volume fraction (a) and modified viscosity (b) at $t = 1.5\ min$.

Modified Viscosity

As introduced in the preceding chapters, the bulk viscosity is modified to account for the influence of particles on the fluid phase. Employing Eilers Equation (Eq. 3.33)[11, 62], the modified viscosity largely depends on the distribution of solid volume fraction. In Figure 5.24a, the distribution of the solid volume fraction is depicted. From the bed surface to the bottom, the solid volume fraction increases towards fully packed condition. The isolines are parallel to the bed surface profile by large as expected. As seen in Figure 5.24b, the distribution of the modified viscosity follows the distribution pattern of the solid volume fraction. The increase in the modified viscosity is more dramatic where the solid volume fraction exceeds 0.55, compared to the bed surface regions where the solid volume fraction is between 0.35 to 0.55. Therefore, the modified viscosity mainly serves to stabilise the

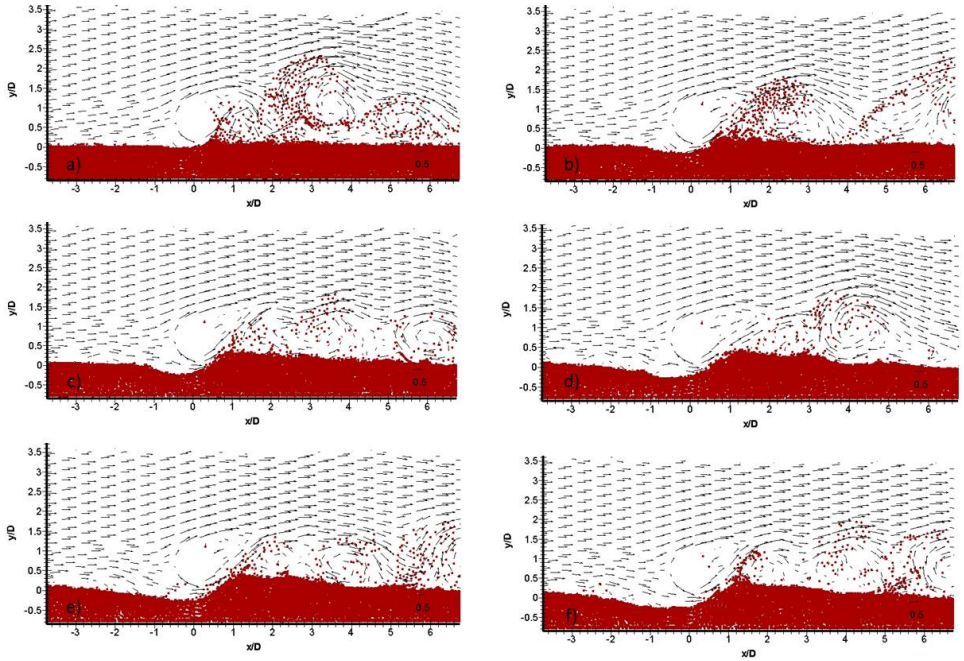

FIGURE 5.25: Particle distribution at selected time. *a*) $t = 4$ *s*, *b*) $t = 12$ *s*, *c*) $t = 24$ *s*, *d*) $t = 37$ *s*, *e*) $t = 41$ *s*, *f*) $t = 45$ *s*.

bed, and it has little influence in the main water body above the bed, where the solid volume fraction is very small due to the dilute suspension. It reflects the proper implementation of Eq. 3.33 in the model.

Particle Distribution

One of the advantages of this model is to trace the discrete particles in a natural way. Consequently, the sand transport can be resolved naturally, and the particle distribution and evolvement can be investigated straightforwardly. Figure 5.25 shows the particle distribution at selected time. The particles are coloured in red, and the flow velocity vectors are also plotted. In Figure 5.25a, we can see at $t = 4$ *s*, particles at the bed surface at the upstream side are dragged by the flow and start rolling and sliding along the bed (bed load). The bed between $x = -0.8D$

and $x = -0.2D$ starts to be scoured and a very mild curve forms underneath the pipe. Compared to the upstream side, the particle motions in the downstream side is dominated by suspension due to the stronger flow velocity and the vortex shedding. It can be seen that at this very beginning of the scour development, a large amount of particles downstream of the pipe have been entrained into the flow, and the bed surface at the downstream side has started to deform. At $t = 12\ s$, the scour hole extends upstream to $x = -1.6D$, and the gap right underneath the pipe is enlarged as shown in Figure 5.25b. As a consequence, particles are piled up near $x = 0.8D$. As time goes on, the scour hole at the upstream side continues developing, the gap between the pipe and the bed keeps enlarging, and the maximum scour location evolves downstream towards right underneath the pipe (see Figure 5.25c, Figure 5.25d, Figure 5.25e and Figure 5.25f). In addition, it is shown that the scour development at the beginning is largely dominated by entrainment and suspension in the downstream side. As time goes on, such phenomenon weakens, and instead the scour hole gradually takes shape. It demonstrates the ability of the model to clearly reproduce the tunnel erosion stage by tracing the particles from a Lagrangian perspective, and even the onset of scour can be reflected as well without using an initial artificial bed profile to facilitate scour development as seen in other models[45, 98].

Bed Evolution

The computed bed profile at $t = 1.5\ min$ is compared to the measurements[45] in Figure 5.26. The shape of the scour hole, the maximum scour depth, and the maximum deposition point in the downstream side are all in good agreement with the measurement, which is the major task of scour prediction. The maximum scour

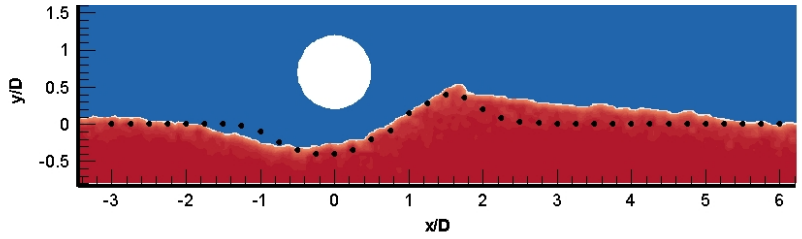

FIGURE 5.26: Computed bed profile at $t = 1.5\ min$ in comparison with the measurements (black dots).

depth is under-predicted by only 1 cm. However, some deviations are observed around $x = -1D$ and in the downstream side. In the modelling result, the bed is scoured slightly deeper between $x = -1.6D$ and $x = -0.8D$. That can be caused by the over-predicted vortex at this location. The over-predicted bed elevation in the downstream side, where the maximum over-prediction is 3 cm, can be associated with the weak flow there, which is not sufficient to wash the sediment particles further downstream. The overall performance of the model to resolve the local scour is considered to be satisfactory.

Figure 5.27 shows the development of the bed profile and the flow field over time. The bed underneath the pipe is eroded away first and the bed further downstream also starts moving from the early stage. The scour hole underneath the pipe is already formed at $t = 25\ s$, and a mount is taking shape due to deposition between $x = 1D - 2D$. These change in the bed elevation intervenes in the development of the flow field, i.e., a stronger jet from underneath the pipe propagates downstream and the lee-wake vortices evolve further downstream behind the mount. As the erosion underneath the pipe continues, a gentle slope is formed at the upstream side. Meanwhile, small vortices come into being above the slope in the upstream side as seen in Figure 5.27i and 5.27j. In the downstream side, the bed behind the mount is eroded away continually.

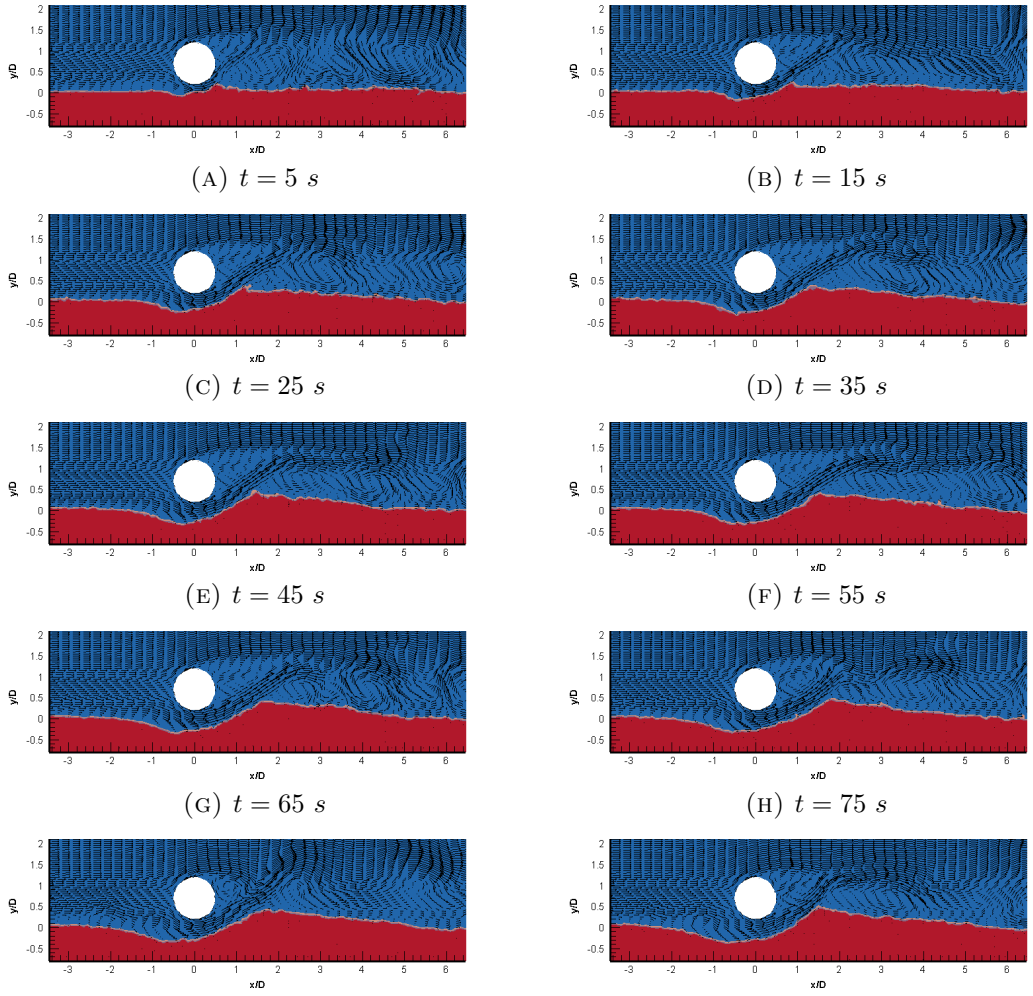

(A) $t = 5\ s$ (B) $t = 15\ s$

(C) $t = 25\ s$ (D) $t = 35\ s$

(E) $t = 45\ s$ (F) $t = 55\ s$

(G) $t = 65\ s$ (H) $t = 75\ s$

(I) $t = 85\ s$ (J) $t = 95\ s$

FIGURE 5.27: Bed profile and the flow velocity field at selected time.

Influence of Hydrodynamics on Bed Profile

After analysis of the detailed flow dynamics, particle motion and bed evolution, five follow-up tests are set up as shown in Table 5.1 to investigate the influence of the modified viscosity and turbulence models on the bed evolution. The results shown above are from Test 6 with modified fluid viscosity and using LES. In comparison, Test 5 also uses LES but the fluid viscosity remains unmodified. In Test 3 and 4, the standard $k - \omega$ turbulence model is employed, either with or without modified viscosity. In Test 1 and 2, only the fluid molecular viscosity is

Test number	Modified fluid viscosity	$k-\omega$ turbulence model	LES modelling
1	○	○	○
2	√	○	○
3	○	√	○
4	√	√	○
5	○	○	√
6	√	○	√

TABLE 5.1: Tests set-up for the current-induced pipeline scour case.

considered and the eddy viscosity is set to zero.

The computed bed profile and flow field in each test are shown in Figure 5.28 and Figure 5.29, respectively. In these two figures, results of Test 1 to Test 6 are shown in the sub-figure a to f in sequence. The fluid viscosity is not modified in the tests on the left column, by contrast with the modified viscosity in those on the right column. No turbulence model is used in the two tests on the top panel. On the middle panel, the $k-\omega$ turbulence model is employed; and on the bottom panel, LES is adopted. In Figure 5.28, we can see that the shape of the scour hole and the maximum scour depth in each test are all in good agreement with the measurements, which is the major purpose of scour prediction. However, the deposition mount at the upstream and downstream side of the pipe are predicted differently with different turbulence models. At the upstream side, using LES, Test 5 and Test 6 produce the bed profile with the best agreement with the measurements. Test 1 and Test 2 over-predict slightly around $x = -2D$. The bed profile produced by $k-\omega$ model in Test 3 and Test 4 are worse than the results in tests either with LES or without turbulence model. With the $k-\omega$ model, the maximum amount of over-prediction in bed elevation is near $x = -2D$. In the downstream side, the bed elevation is over-predicted between $x = 2D$ and $x = 5D$, the maximum scour depth is predicted very well though. A quantitative comparison among these tests are shown in Table 5.2. Results in Test

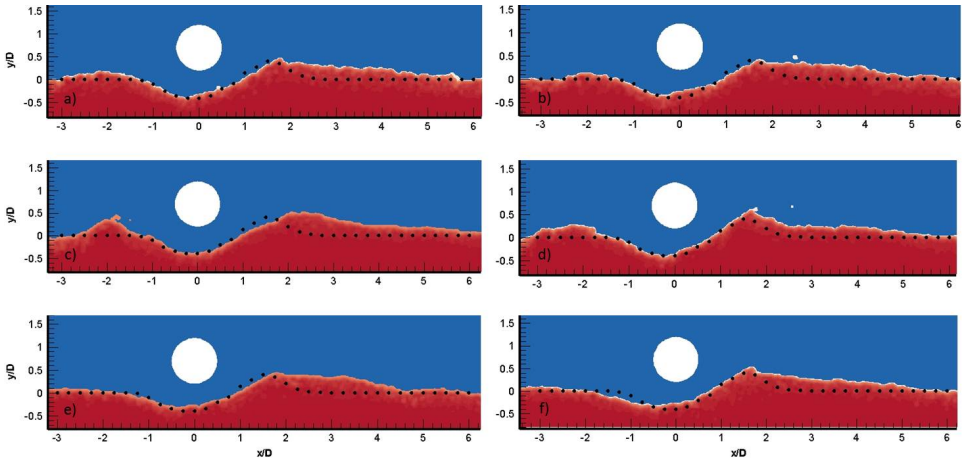

FIGURE 5.28: Computed bed profile at $t = 1.5\ min$ in comparison with the measurements (black dots). From a) to f) are Test 1 to Test 6 in sequence.

Test number	Upstream	Scour hole	Downstream
1	2 cm	1 cm	3 cm
2	1.2 cm	1.1 cm	3 cm
3	3.8 cm	0 cm	5 cm
4	3 cm	0 cm	3 cm
5	1 cm	1 cm	3.5 cm
6	1 cm	1 cm	3 cm

TABLE 5.2: Maximum discrepancies observed at the upstream side, scour hole and downstream side of the pipe in each test.

1 and Test 6 reach the best agreement with the measurement, while the results produced by $k - \omega$ model without modified viscosity in Test 3 see the biggest deviation from measurements. With respect to the effect of the modified viscosity, we can see that in each panel, tests with modified viscosity produce smoother bed profile at both the upstream and downstream side of the pipe, which are closer to the measurements. Especially at the downstream side, the over-predicted bed elevation is reduced by adopting the modified viscosity. Therefore, the modified viscosity plays its role in the interaction between the solid phase and the fluid phase, and consequently, it influences the formation of bed profile.

In Figure 5.29, the flow velocity vectors are plotted. The flow pattern in Figure 5.29a and Figure 5.29b resemble each other, where the only difference between

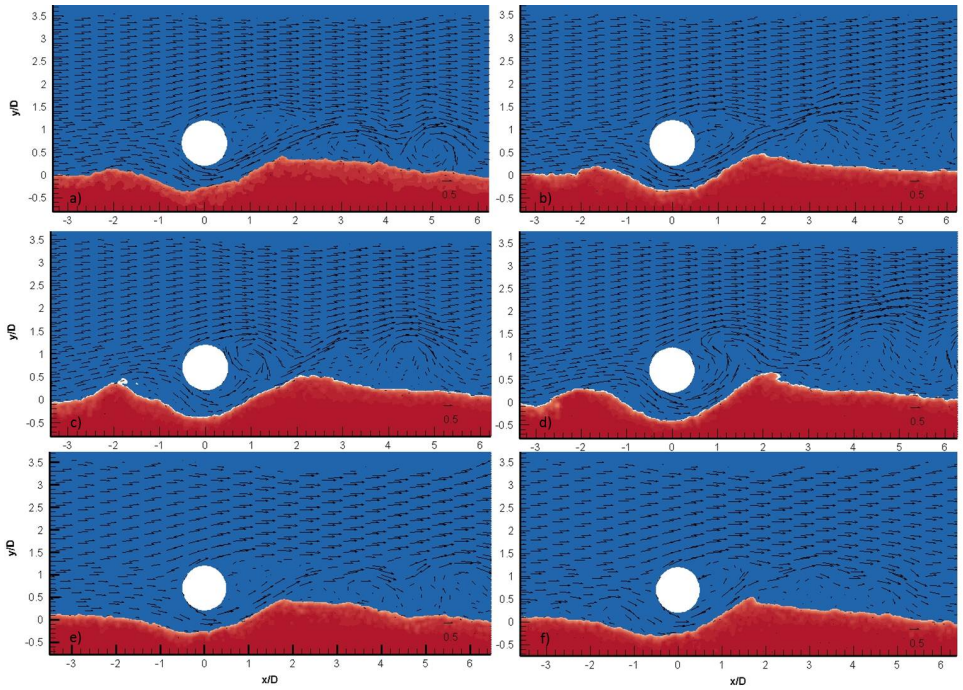

FIGURE 5.29: Computed flow velocity field at $t = 1.5\ min$. From a) to f) are Test 1 to Test 6 in sequence.

these two tests is whether the fluid viscosity is modified or not. Only the flow velocity very close to the bed surface is slightly different from each other. This finding also applies to the middle and bottom panels (see Figure 5.29c, Figure 5.29d, Figure 5.29e and Figure 5.29f). This is because the modified viscosity only influences the bed region, especially the regions of high solid volume fraction, and has little effect in the main flow body as shown in Figure 5.24. However, the flow patterns produced with different turbulence models are different to each other. The detailed flow vector field plotted at every point on the Eulerian grid in Test 2, Test 4 and Test 6 are shown in Figure 5.30 for a clearer comparison, in which no turbulence model, the standard $k - \omega$ turbulence model and LES is employed respectively. The acceleration jet underneath the pipe in the scour hole, and the flow acceleration above the pipe are all captured in these three tests. This serves as a prerequisite to the well captured scour hole in these tests. However, at the upstream side, only LES resolves the detailed vortices immediately above the bed surface (see Figure 5.30c), while without turbulence modelling, only a

small vortex is formed at $x = -2D$ (see Figure 5.30a); and $k-\omega$ model generates a much bigger vortex in front of the upstream mount (see Figure 5.30b), which explains the over-predicted bed elevation observed in Test 2 and Test 4. At the downstream side, without turbulence modelling, the recirculation zone behind the pipe is bigger, and the dissipation of the vortex is much weaker than that modelled with LES. In test 4 with the $k-\omega$ model, the flow field at the downstream side is much distorted, and the wake flow region above the bed starting from $x = 2D$ and extending downstream is larger than that in the other two tests. Test 6 with LES resolves the fine details of the flow structure, and consequently, the predicted bed profile is in better agreement with the measurement.

Onset of Scour

Onset of scour is the initial stage in the scour development underneath a pipeline. Seepage flow and piping are the two dominant processes involved[80]. The seepage flow in the bed underneath the pipe is driven by the pressure difference between the upstream and downstream side of the pipe. When it reaches a critical value, piping takes place. The sand at the immediate downstream of the pipe will rise and eventually a mixture of water and sand will break through and a breach or a narrow pathway is formed.

However, in numerical modelling of scour development, onset of scour is rarely simulated. Most existing scour models initiate the simulation with a gap between the pipe and the bed, where an initially sinusoidal bed profile is the most commonly used trick to facilitate scour development. In the results of the current-induced

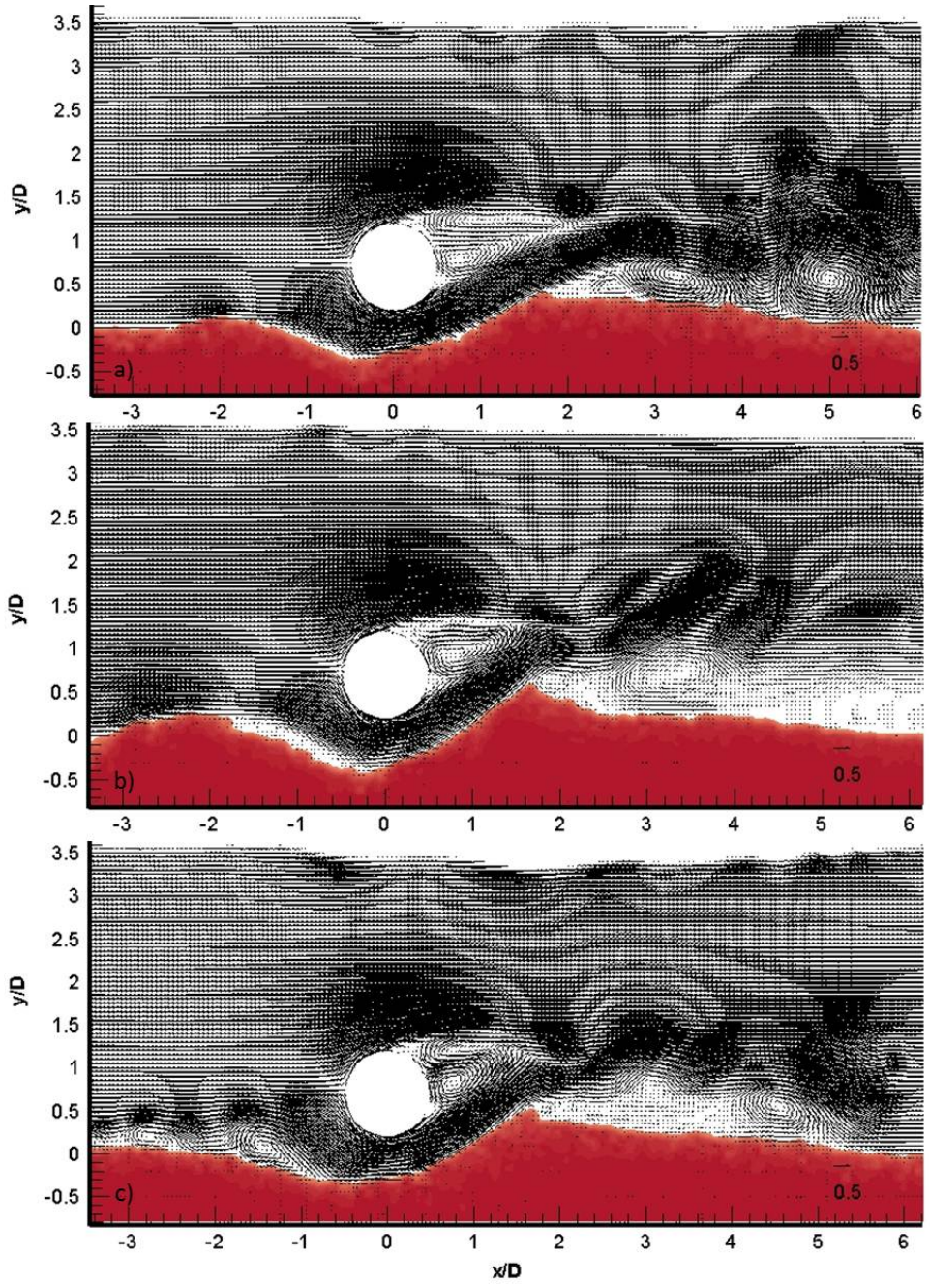

FIGURE 5.30: Detailed flow velocity field at $t = 1.5$ *min* in Test 2 (a), Test 4 (b), and Test 6 (c).

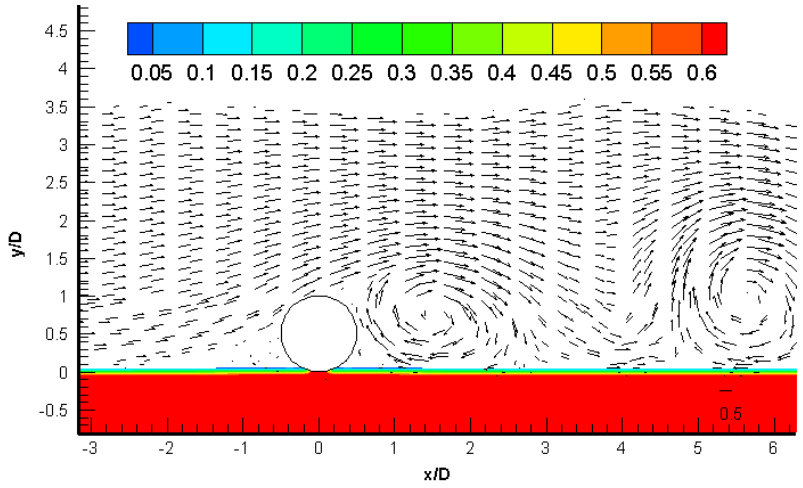

FIGURE 5.31: The initial set-up for simulation of onset of scour.

pipeline scour presented so far, an initially flat bed profile is used in the present model, however still with an initial 2 *cm*-high gap.

To study the onset of scour, the pipe is placed directly on the bed without any gap as shown in Figure 5.31, apart from which, the test set-up is the same as in Test 6 (see Table 5.1). It is therefore a direct test to examine the model's capability to resolve the scour initiation process. The flow field is developed before allowing the bed to move in order to produce a realistic and stable hydrodynamic environment for the scour development. Then the bed is free to evolve with this developed flow field as an initial condition. The flow field and the distribution of the solid volume fraction are shown in Figure 5.31.

Figure 5.32, Figure 5.33 and Figure 5.34 show the time development of the bed profile and the flow velocity field once the bed is mobile. The colour bar in these three figures are all the same as shown in Figure 5.31. It is seen in Figure 5.32 that, there is almost no disturbance in the bed upstream of the pipe in the initial 0.5 *s* due to the very small flow velocity immediately above the bed. On the contrary,

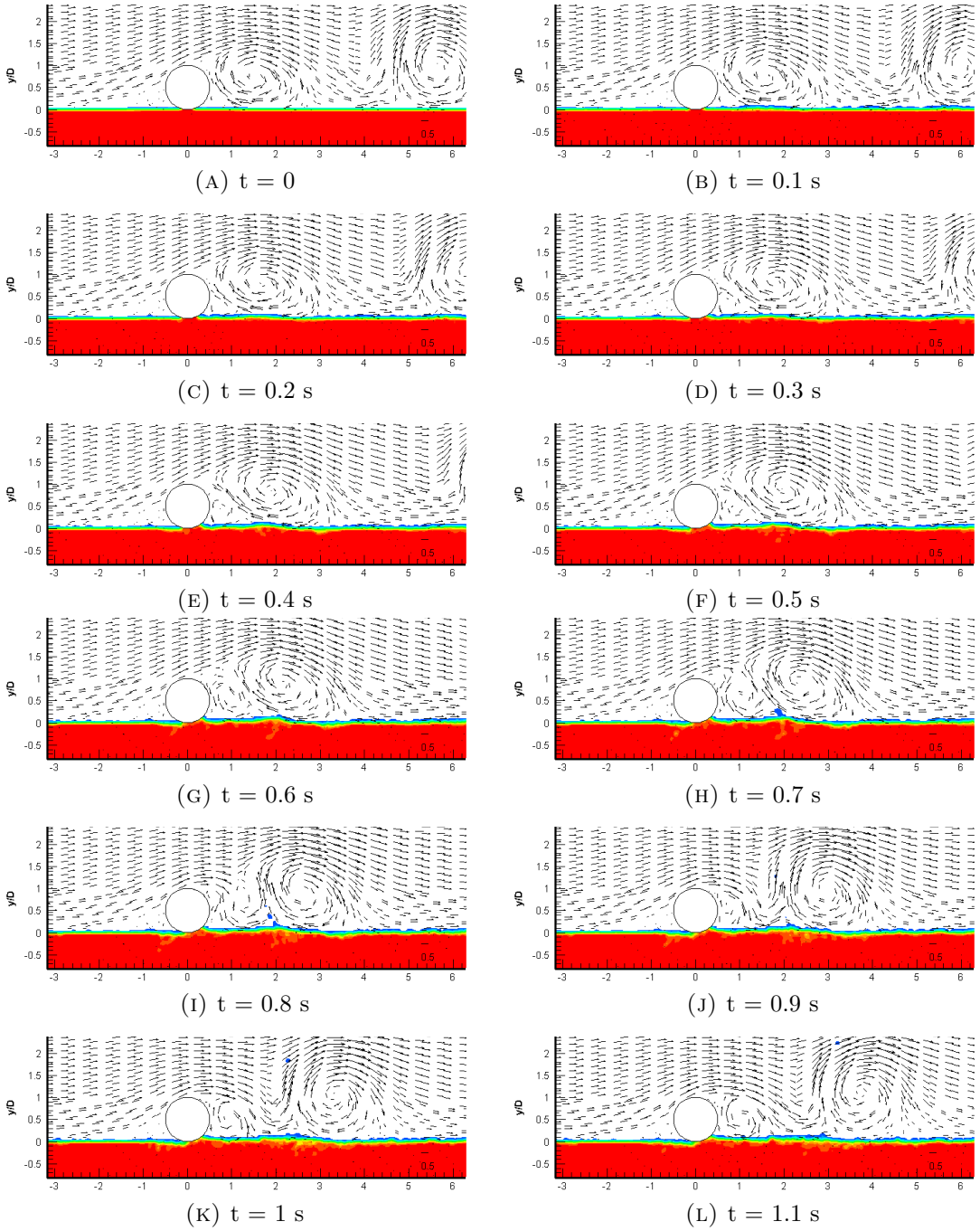

(A) t = 0 (B) t = 0.1 s

(C) t = 0.2 s (D) t = 0.3 s

(E) t = 0.4 s (F) t = 0.5 s

(G) t = 0.6 s (H) t = 0.7 s

(I) t = 0.8 s (J) t = 0.9 s

(K) t = 1 s (L) t = 1.1 s

FIGURE 5.32: Development of the bed profile and flow velocity field (Part I).

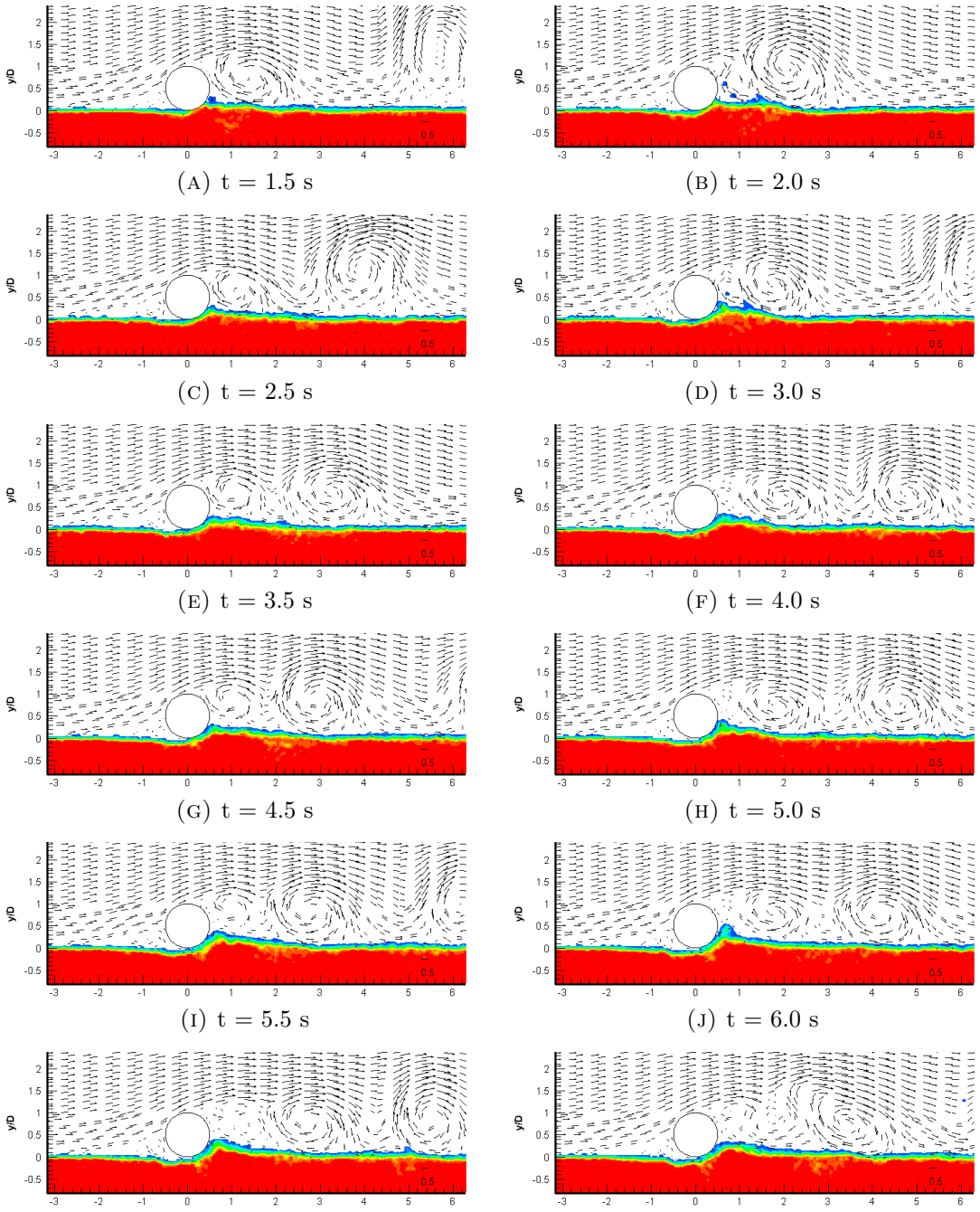

(A) t = 1.5 s (B) t = 2.0 s

(C) t = 2.5 s (D) t = 3.0 s

(E) t = 3.5 s (F) t = 4.0 s

(G) t = 4.5 s (H) t = 5.0 s

(I) t = 5.5 s (J) t = 6.0 s

(K) t = 6.5 s (L) t = 7.0 s

FIGURE 5.33: Development of the bed profile and flow velocity field (Part II).

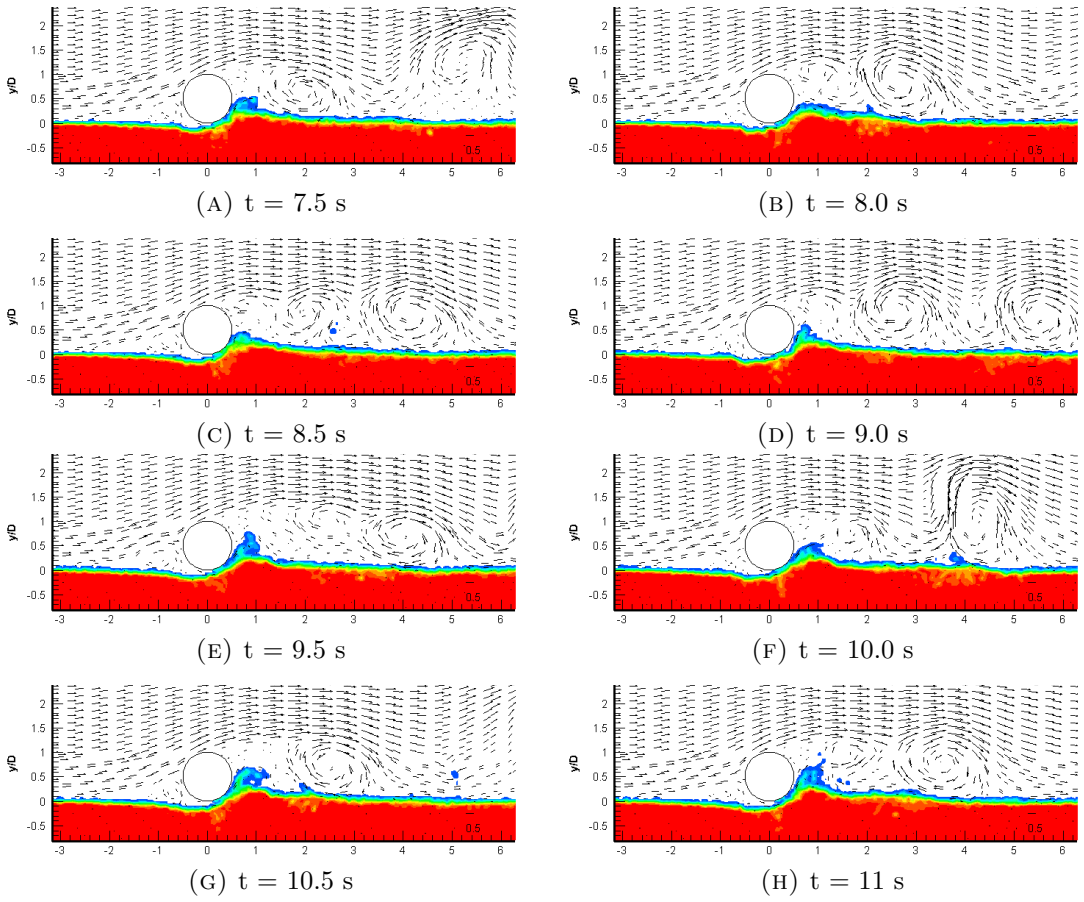

(A) t = 7.5 s (B) t = 8.0 s

(C) t = 8.5 s (D) t = 9.0 s

(E) t = 9.5 s (F) t = 10.0 s

(G) t = 10.5 s (H) t = 11 s

FIGURE 5.34: Development of the bed profile and flow velocity field (Part III).

at the downstream side, remarkable vortices are observed and a disturbance in the bed in the immediate wake of the pipe is visible from $t = 0.2\ s$. Due to the considerable flow velocity and the evolving vortices above the bed, deformation in the bed surface downstream of the pipe has already been observed in the initial 1.1 s, the amplitude of which is very minor though. The bed surface between $x = 0.1D$ and $x = 0.2D$ starts rising in the first place and piping occurs. Subsequently, the initially fully packed region underneath the pipe between $x = -0.1D$ and $x = 0.1D$ starts moving along the pipe perimeter and evolving towards the downstream side. The region of low solid volume fraction in the bed surface initially in front of the pipe moves towards downstream and locates directly underneath the pipe till $x = 0$ at $t = 1.1\ s$.

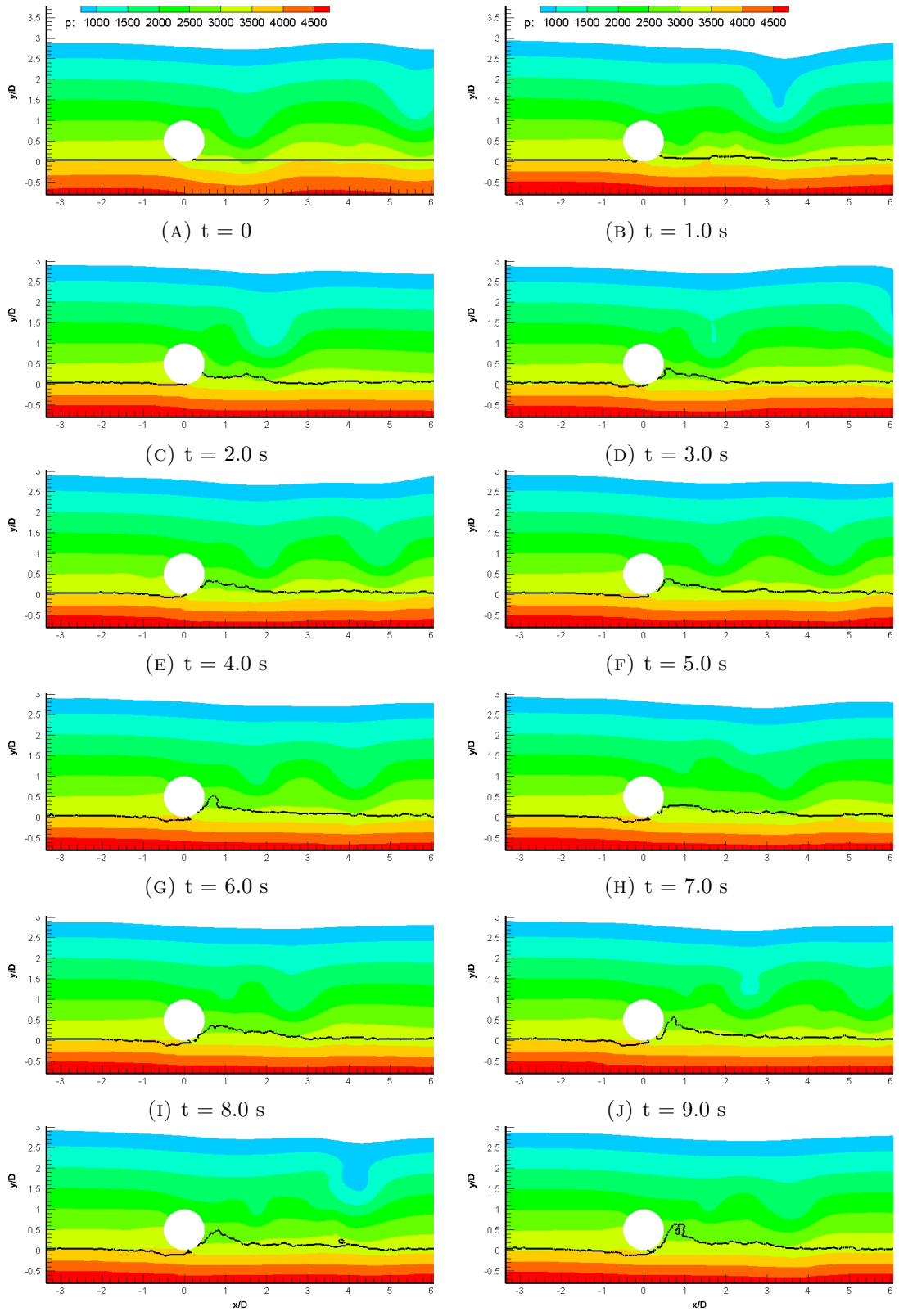

(A) t = 0 (B) t = 1.0 s

(C) t = 2.0 s (D) t = 3.0 s

(E) t = 4.0 s (F) t = 5.0 s

(G) t = 6.0 s (H) t = 7.0 s

(I) t = 8.0 s (J) t = 9.0 s

(K) t = 10.0 s (L) t = 11.0 s

FIGURE 5.35: Development of the pressure field. Bold black line: bed profile.

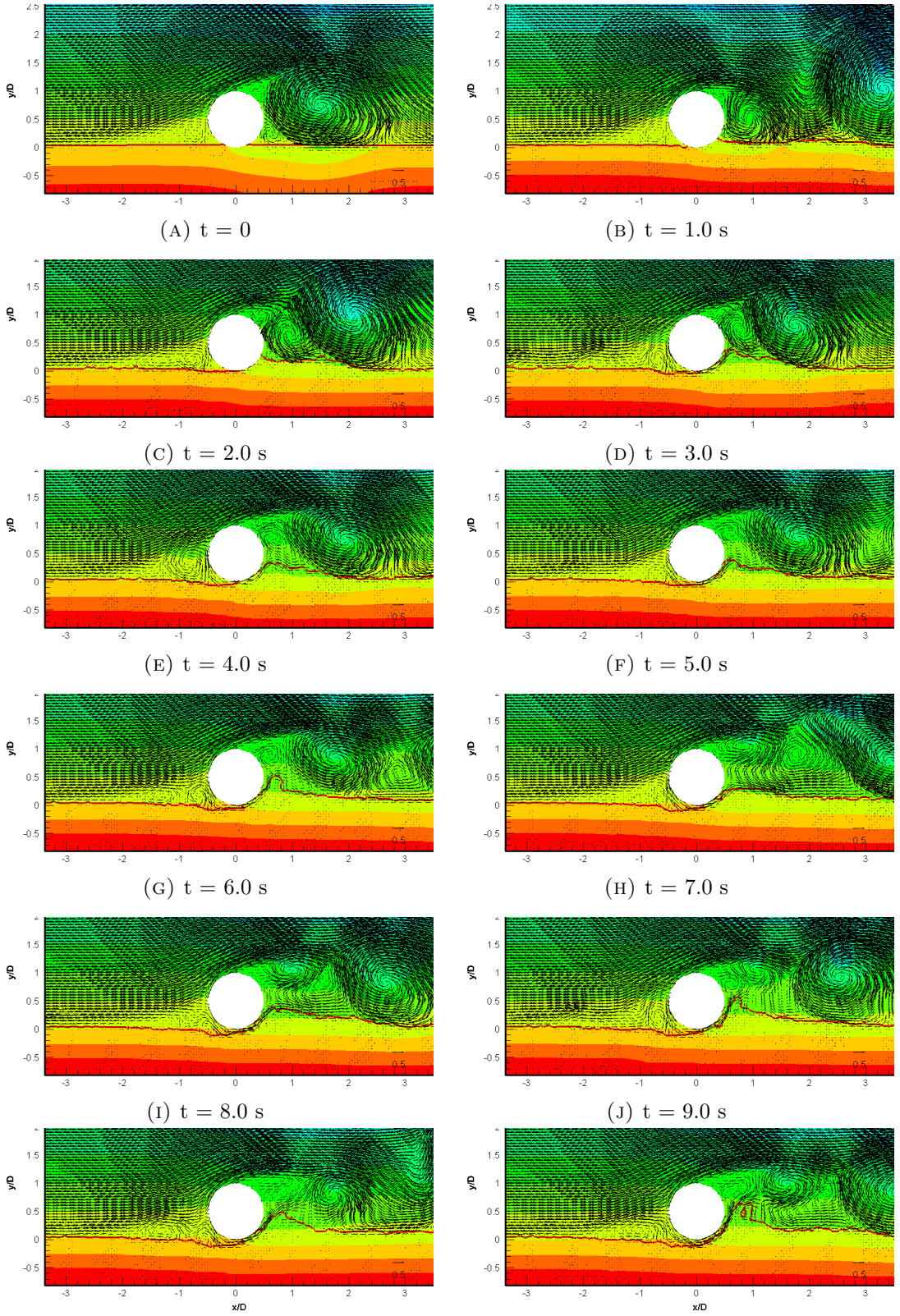

(A) t = 0 (B) t = 1.0 s

(C) t = 2.0 s (D) t = 3.0 s

(E) t = 4.0 s (F) t = 5.0 s

(G) t = 6.0 s (H) t = 7.0 s

(I) t = 8.0 s (J) t = 9.0 s

(K) t = 10.0 s (L) t = 11.0 s

FIGURE 5.36: Development of the flow field and bed profile. Contour: flow pressure field; vector: flow velocity field; bold red line: bed profile.

At $t = 2.0\ s$, the low solid volume fraction layer at the bed surface connects between the upstream and downstream side of the pipe and a very narrow pathway is formed underneath the pipe. A very mild slope underneath the pipe at the upstream side comes into being and starts taking shape from $t = 3\ s$. Meanwhile, the vortex between the pipe and this mild slope develops and further promotes the formation of the slope. At $t = 5\ s$, the bed surface is seen to detach from the pipe perimeter. It allows water to accelerate in the narrow pathway and get it expanded. The mixture of water and sand can move via this channel towards the downstream side more easily and a dune is formed gradually in the immediate downstream. Gradually the tunnel erosion stage starts. A jet of water and sand mixture is observed in the pathway underneath the pipe at $t = 6.0\ s$ (see Figure 5.33), and the vortices in the lee-wake side are adjusted due to the development of the dune. After that, the pathway keeps developing (see Figure 5.34), and the bed underneath the pipe is being eroded and moving downstream. The pathway underneath the pipe is more expanded around $t = 9.5\ s$, and the flow velocity in this pathway is comparable to the undisturbed velocity. As time goes on in the tunnel erosion stage, the pathway will develop into a scour hole and the dune in the downstream side will be more significant as shown in the preceding sections. The model's capability to simulate the onset of scour from an initially flat bed without any gap between the bed and the pipe is demonstrated well.

It is also noteworthy that at beginning ($t = 0.3\ s$), a small vortex is generated underneath the large vortex just above the bed downstream of the pipe. It will push away the large vortex and grow in size during $t = 0.5\ s$ and $t = 0.7\ s$. Later when the bed surface rises up ($t = 3.0\ s$), the small vortex will generate at a higher level and push the large vortex away fairly quickly ($t = 3.5\ s$). At $t = 10\ s$, the vortex is generated immediately behind the top of the pipe, other than at the bed surface. The flow behind the pipe above the bed then becomes fairly calm as the

hump is in place.

The pressure difference between the upstream and downstream side of the pipe is an important driving mechanism during onset of scour. The development of the pressure field during this process is shown in Figure 5.35. The bold black line in this figure is the isoline of the solid volume fraction being 0.05, which illustrates the most surface layer of the bed. The pressure difference is observed initially in Figure 5.35a, where the isobar in the bed underneath the pipe and at the downstream side is not as parallel as that at the upstream side. The pressure at the upstream side, i.e., in front of $x = 0$, is larger than that on the same elevation level in the downstream side. This pressure difference drives the initiation of the bed deformation underneath the pipe by forming a seepage flow in the first place. As the bed starts getting disturbed, although the isobar at the downstream side above the bed varies with time due to the adjustment of the flow to the presence of the pipe and the evolvement of the bed, that in the bed tends to become parallel to the bottom boundary. Especially when the pathway underneath the pipe is formed around $t = 5\ s$ and gradually becomes more expanded, the pressure difference between the upstream and downstream side is much less predominant in the bed. For a closer view, the distribution of the pressure field, the flow velocity field and the bed surface profile in a smaller neighbourhood of the pipe are presented in Figure 5.36. As the bed is porous, once it is mobile, there are very minor flow in the bed, which is not yet able to move the sand particles and deform the bed. Driven by the pressure difference underneath the pipe, the seepage flow there transfers momentum to the sand particles and gradually the bed surface in the immediate downstream of the pipe starts rising. At $t = 3.0\ s$, a breakthrough in the bed surface underneath the pipe is observed, and the flow velocity there is enlarged. Then more water at the upstream side squeezes into the breach underneath the pipe and accelerates there, which offers more momentum

to the particles to evolve downstream. Since $t = 5.0\ s$, the pressure difference between the upstream and downstream side is much less significant at this stage, and the large flow velocity in the pathway becomes the driving force to erode away the bed surface layer. As time goes on, tunnel erosion starts and the pathway is further enlarged.

5.4.2 Wave-Induced Pipeline Scour

To test the model's performance under waves, a wave scour test by Sumer and Fredsøe[78] is studied numerically by the model. The experiment was a wave-induced pipeline scour test performed in a 0.6 m wide wave flume[78]. The mean water depth was maintained constant at 40 cm. Waves were produced by a piston-type wave generator. The wave frequency was 0.82 s^{-1}, and the maximum outer flow velocity U_m was 0.24 ms^{-1}. The Keulegan-Carpenter number $KC = 11$. A pipe of a diameter $D = 3\ cm$ with a hydraulically smooth surface was placed on a sandy bed. The median grain size was 0.18 mm. The scour development was monitored by a video camera.

The computational domain is set as 30 cm long, 14.4 cm high and one cell wide. The mesh resolution is 0.15 cm. The time step is $1 \times 10^{-4}\ s$. The pipe is placed above a 2.4 mm deep bed. The critical solid volume fraction is 0.65, and the bed is fully packed with $\theta_s = 0.6488$ initially. Same as in the sheet flow simulation presented in Section 5.3.1, an oscillatory body force is used to reproduce the wave-induced oscillation near the bed to save computational costs. Periodic

boundary conditions are employed at the inlet and outlet boundary. Slip boundary conditions are used at the front and back boundaries such that the simulation is not restricted by the two-dimensional domain. LES is employed to resolve the turbulence characteristics.

Flow Field and Bed Evolution

Figure 5.37 shows the time series of the bed surface and the flow velocity field in one wave cycle. At $t = 29\ s$, water flows rightwards, and a vortex is generated at the r.h.s. of the pipe. A small vortex is also observed on the l.h.s. above the pipe. At $t = 29.1\ s$, flow starts reversing, the l.h.s. vortex above the pipe grows and small vortices are observed above the bed surface on the l.h.s. The flow keeps accelerating towards the l.h.s. during $t = 29.2 - 29.4\ s$, when large velocity is observed around the pipe, and the vortex on the l.h.s. is enhanced. At $t = 29.5\ s$, vortex on the r.h.s. no longer exists as the flow is completely leftward. At $t = 29.6\ s$, the vortices on the l.h.s. have developed well. Then the flow starts reversing towards the r.h.s again. Vortices exist on both side during the flow reversal as seen in Figure 5.37h, 5.37i, 5.37j and 5.37k.

The median grain size of the bed is only $0.18\ mm$, as a result of such fine sand, the bed is very fluidised under waves. When the flow is reversing towards the l.h.s., the bed underneath the pipe is eroded away towards the l.h.s., and a mild slope is formed between $x = 0$ and $x = -2\ cm$ during $t = 29.3 - 29.6\ s$. When flow reverses towards the r.h.s. from $t = 29.7\ s$, the sand is transported in the same direction toward underneath the pipe. Consequently, the slope formed previously

between $x = 0$ and $x = -2$ cm is backfilled, and the bed underneath the pipe almost recovers to level status at $t = 29.7 - 29.8$ s. After which, a very mild slope starts taking shape underneath the right half of the pipe.

The sub-grid scale kinetic energy, sub-grid scale eddy viscosity and the vorticity field at $t = 0.5$ min is shown in Figure 5.38. The distribution of the sub-grid scale kinetic energy follows that in the current-induced pipeline scour case as shown in Figure 5.23a: high kinetic energy is observed above and below the pipe and along the bed surface. In Figure 5.38b, the sub-grid scale eddy viscosity is of high value along the bed surface and around the pipe. High value of eddy viscosity is also found at the location of the l.h.s. vortex and further above on the l.h.s. On the r.h.s. of the pipe, a high value region is also observed between $x = 7 - 10$ cm, but it is weaker in magnitude compared to the l.h.s. where a vortex exists. Figure 5.38c shows the distribution of the vorticity field, the high value regions of which are almost identical to those of the sub-grid scale eddy viscosity. Such phenomenon is also found in the current-induced scour case.

The bed profile at 0.5 min and 1 min are compared to the measurements in Figure 5.39. The bed surface is plotted as the isoline of the solid volume fraction being 0.6. The overall scour pattern is well captured as seen in these two figures, where the gentle bed slopes on both sides of the pipe under waves are reproduced. The maximum scour depth is also in good agreement with the measurements. At $t = 0.5$ min, small fluctuations are observed in the bed surface between $x = -10$ cm and $x = 10$ cm, which illustrates the response of the bed to the oscillatory flow at the early stage. As time goes on, the gap between the pipe and the bed is enlarged, which slows down the near-bed flow velocity, and the bed surface is smoother at $t = 1$ min than at $t = 0.5$ min. As reviewed in Section 2.2.1,

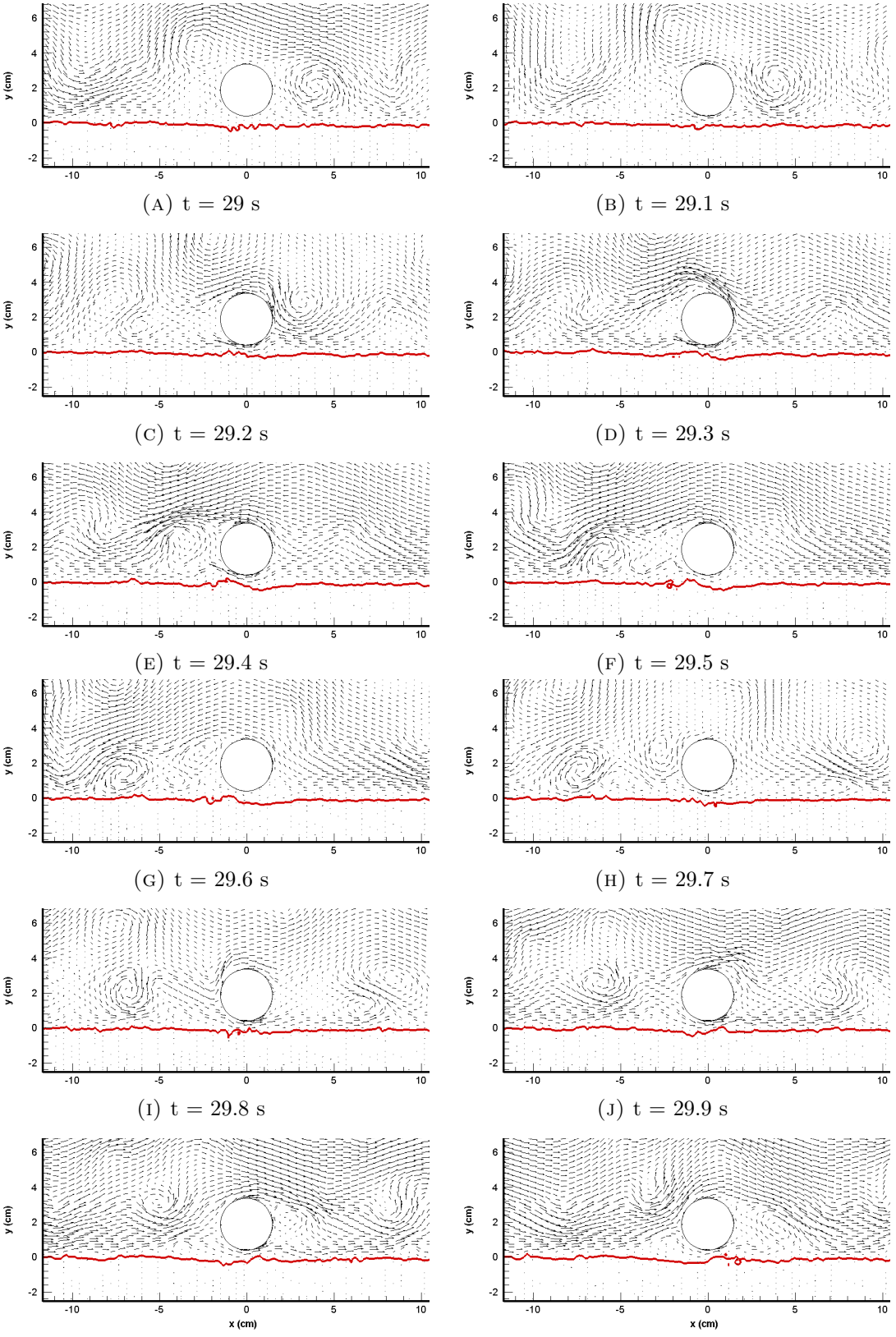

(A) t = 29 s (B) t = 29.1 s

(C) t = 29.2 s (D) t = 29.3 s

(E) t = 29.4 s (F) t = 29.5 s

(G) t = 29.6 s (H) t = 29.7 s

(I) t = 29.8 s (J) t = 29.9 s

(K) t = 30 s (L) t = 30.1 s

FIGURE 5.37: Development of the bed profile and flow velocity field.

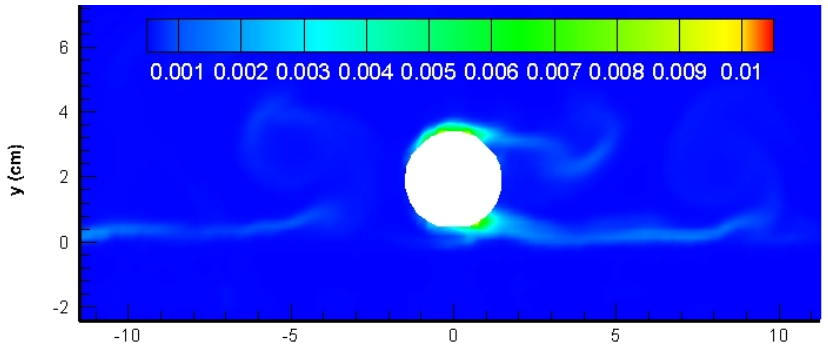

(A) Sub-grid scale kinetic energy

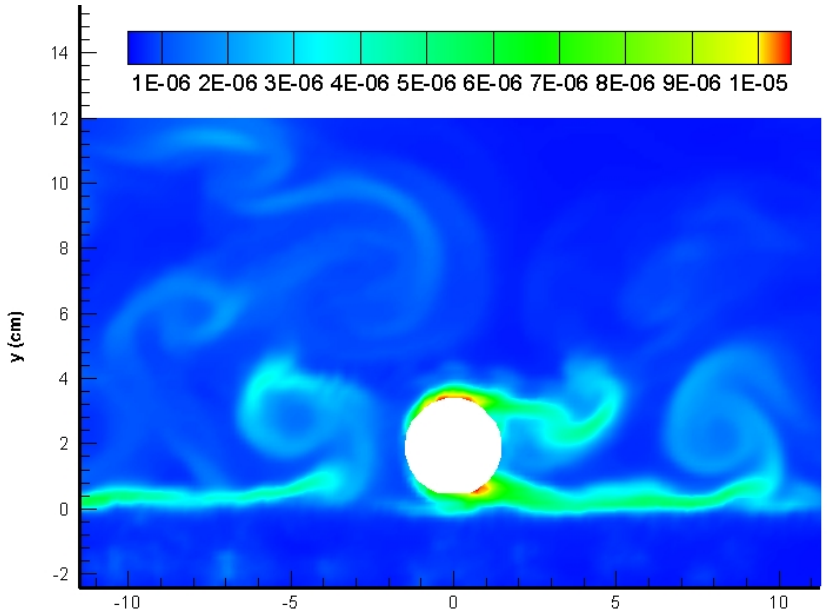

(B) Sub-grid scale eddy viscosity

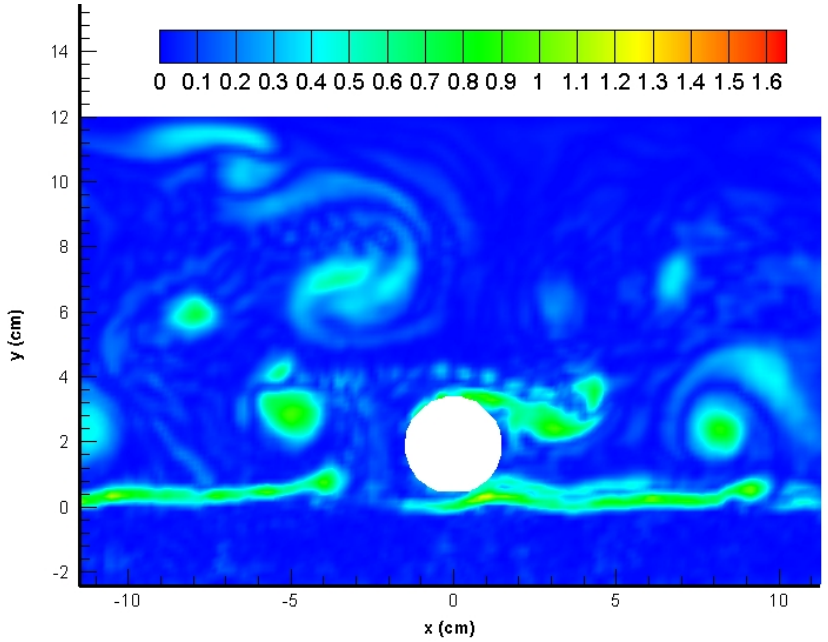

(C) Vorticity

FIGURE 5.38: Sub-grid scale kinetic energy, eddy viscosity and vorticity at $t = 0.5\ min.$

Sumer and Fredsøe[78] indicate that the extension of the lee-wake vortex street L_v under waves satisfies a relation that $\frac{L_v}{D} = 0.3KC$, and therefore the extent of the bed being influenced is largely of the same length scale. This is also reflected in the modelling results. In this case, $L_v = 9.9\ cm$, and the bed slope on both sides extends to around $x = \pm 7\ cm$. Although the scour depth is well predicted, the maximum scour depth at $t = 1\ min$ is slightly underestimated. This can be due to the fact that the computational domain is not long enough to avoid backfilling. Sand being eroded away and exit from the inlet/outlet boundary will get back into the domain from the other side as imposed by the periodic boundary condition. Therefore, it can get backfilled into the scour hole again. This issue can be avoided by using a longer domain, however, that means a much larger computational expense. Plus, as $L_v = 9.9\ cm$ in this case, using a domain of 15 cm long on each side of the pipe should be considered a proper choice. Considering the overall good behaviour of the modelling results, the model's ability to resolve wave scour is satisfactory.

Particle Distribution

The particle distribution and the flow vorticity field over a wave cycle are shown in Figure 5.40 and 5.41. It is evident that the particle distribution follows the distribution pattern of the flow vorticity throughout the wave cycle. It reflects the importance of the hydrodynamic drag force to the particle motion. Moreover, particles are located around a high vorticity region rather than in the core of it. At $t = 29\ s$, the main flow is rightward, and vortices are developed on the r.h.s. of the pipe. At $t = 29.1\ s$, the flow starts developing into a leftward flow as shown in Figure 5.37b. Particles are therefore moving towards the l.h.s. with the

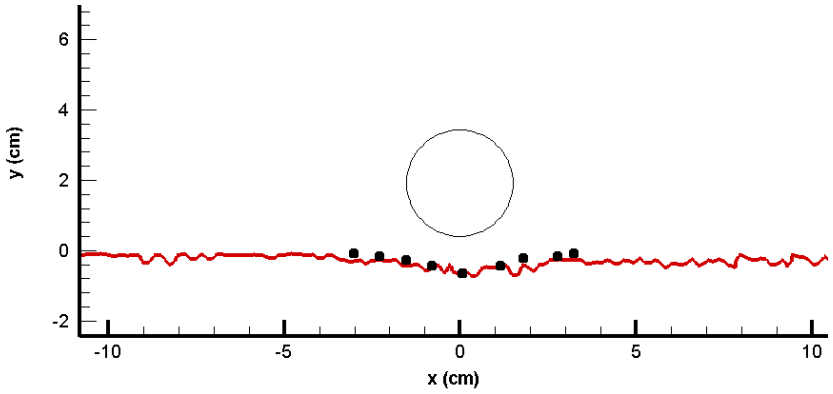

(A) $t = 0.5\ min$

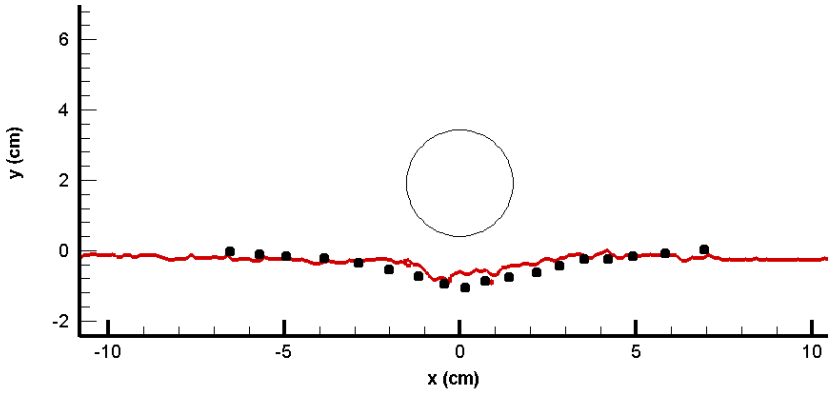

(B) $t = 1\ min$

FIGURE 5.39: Bed profile comparison against measurements. Red line: modelling result; black dots: measurements.

flow, and a small dune is formed under the left half of the pipe as seen in Figure 5.40d, 5.40e, 5.40f and 5.41a. At $t = 29.7\ s$, the flow reverses to a rightward flow, and particles are therefore transported towards the r.h.s. as well. The small dunes formed on the l.h.s are gradually washed towards the r.h.s. As a result, the bed recovers to almost level. As the rightward flow develops, a small dune starts forming underneath the right half of the pipe at $t = 30.1\ s$. It is also noteworthy that suspension is prevailing throughout the whole wave cycle due to the small particle size.

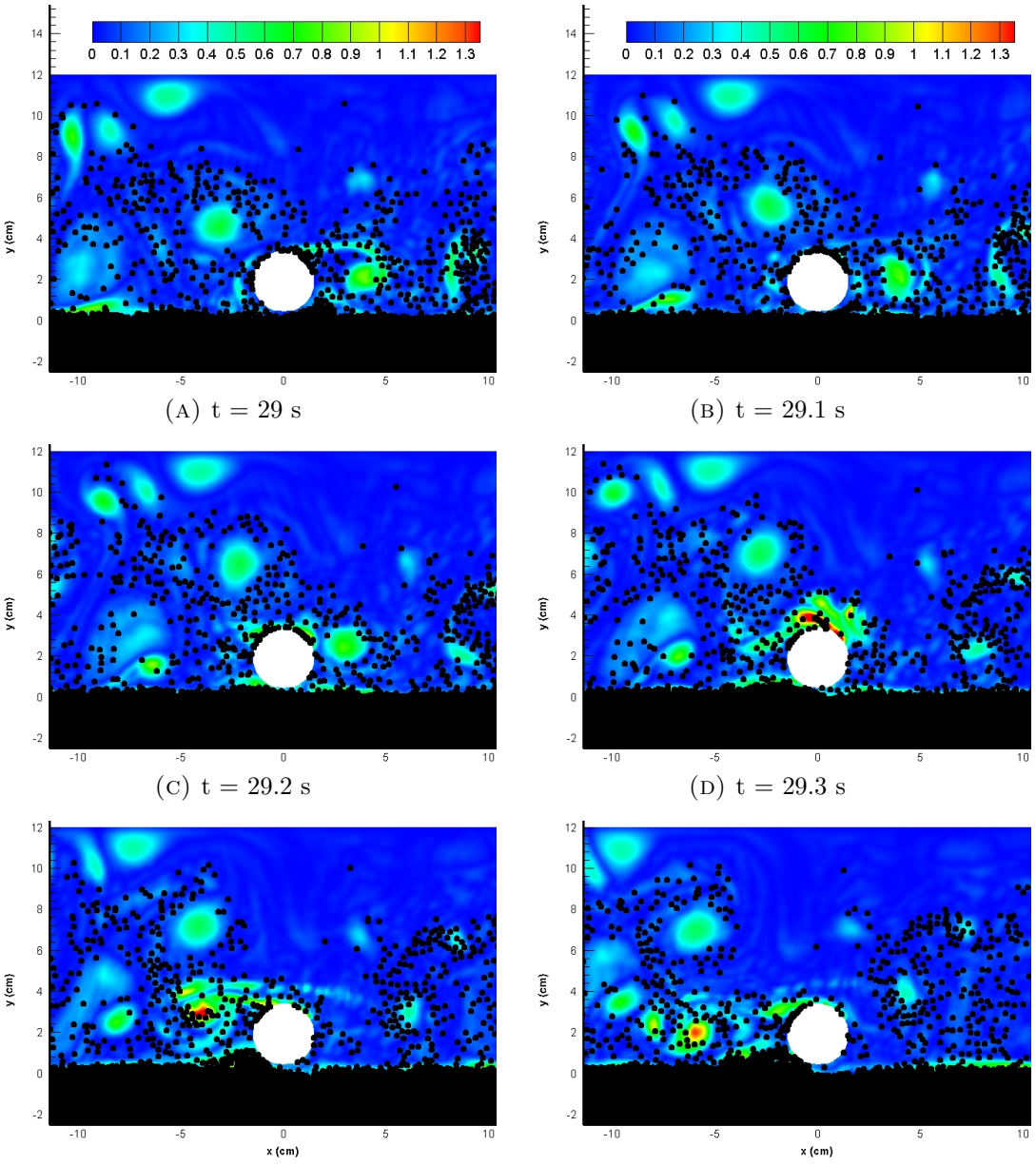

(A) t = 29 s (B) t = 29.1 s

(C) t = 29.2 s (D) t = 29.3 s

(E) t = 29.4 s (F) t = 29.5 s

FIGURE 5.40: Vorticity and particle distribution (Part I).

5.5 Conclusions

The model is applied to a range of experiments to testify its behaviour regarding the hydrodynamics, sediment transport and scour development, respectively. Firstly, the hydrodynamic performance of the model under steady currents and

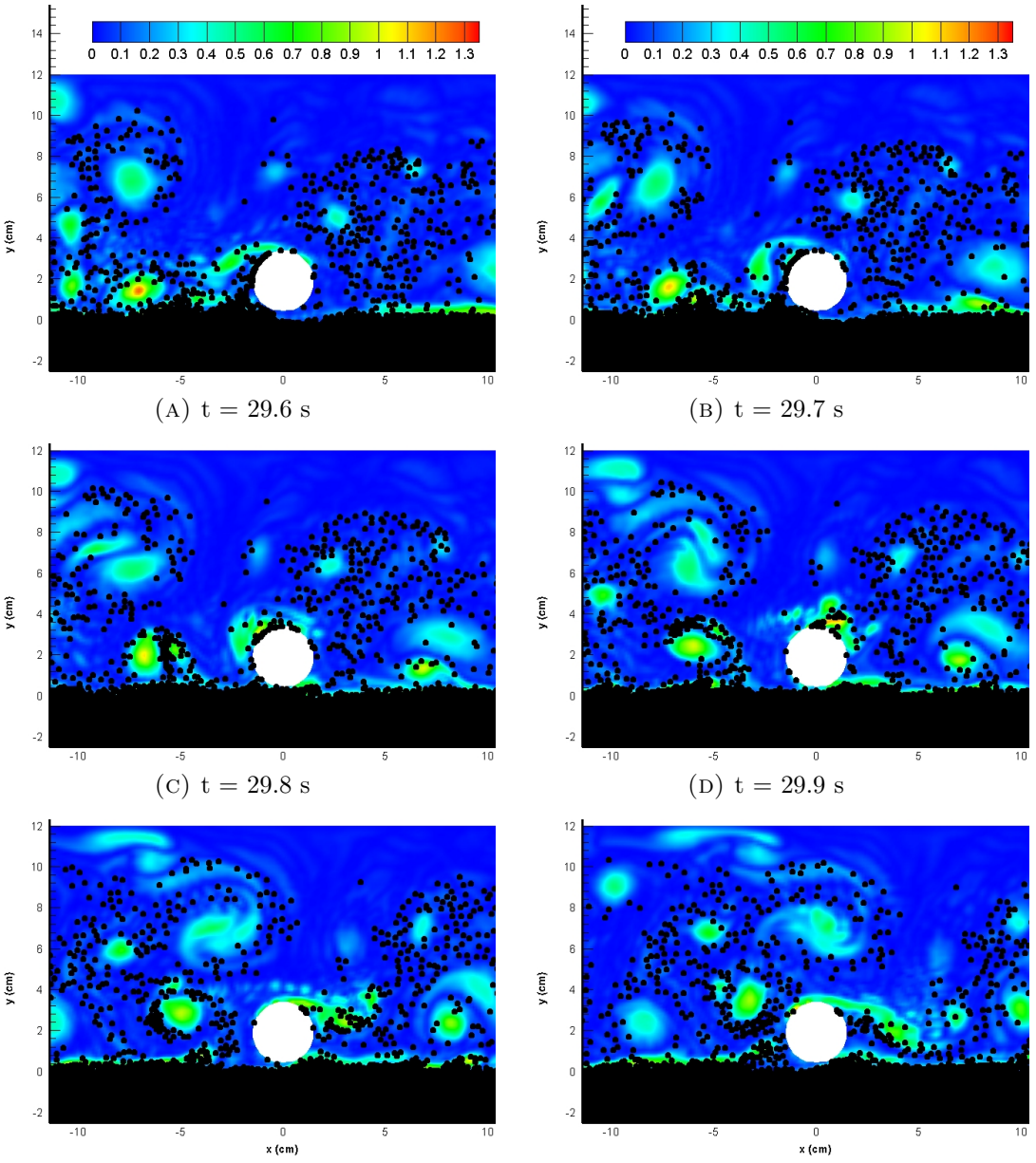

(A) t = 29.6 s (B) t = 29.7 s

(C) t = 29.8 s (D) t = 29.9 s

(E) t = 30 s (F) t = 30.1 s

FIGURE 5.41: Vorticity and particle distribution (Part II).

waves respectively are satisfactory. The predicted velocity profiles are in good agreement with the measurements, and the three-dimensional feature of the flow around a vertical pile is also resolved by the model, which is very promising. Some deviation exists in layers very close to the wall, where it is very demanding on the turbulence model and the mesh quality. A even finer mesh near the wall and a more accurately prescribed turbulence model, especially the wall function involved, can be the solution to eliminate such deviation. The water surface elevation and the

time-averaged horizontal velocity profile under a plunging wave are resolved well by the model, even around the breaking point. The overall pattern is captured well by the model, deviations in the maximum water surface elevation are observed though. Secondly, the sediment transport under such challenging conditions as an oscillatory sheet flow is resolved by the model. The sediment concentration profiles at various phases are in agreement with the measurements even at flow reversal.

In the end, the model is applied to benchmark pipeline scour cases under currents and waves respectively. In the current-induced scour case, the flow pattern around the pipe including detailed vortex structures is captured by the model with LES. The sub-grid scale kinetic energy is found to be high around the pipe where flow re-acceleration is observed, and the sub-grid scale eddy viscosity is high both around the pipe and above the seabed where vortices are prevailing. The modified viscosity basically follows the distribution pattern of the solid volume fraction due to the formulation, therefore, it is only effective in the bed as expected and helps to stabilise the bed. The predicted bed profile agrees well with the measurements especially the maximum scour depth and the shape of the scour hole. Particle motions are more active at the lee-wake side where a vortex street exists and the sub-grid scale eddy viscosity is high. In addition, the influence of the hydrodynamics on the bed profile development is also investigated by employing different turbulence models and modified viscosity. The results show that $k-\omega$ model cannot resolve the detailed structure of the vortices above the bed and therefore unrealistic pile-up of sand are found on both sides of the pipe. LES achieves the best results with a modified viscosity. The flow structures are resolved in detail and the bed profile is reproduced closest to the measurements. The modified viscosity is found to smooth the bed surface in comparison to the results with unmodified viscosity. Furthermore, the model's ability to simulate onset of scour from an initially flat bed without any gap between the pipe and

the seabed is demonstrated well. The pressure difference between the upstream and downstream side of the pipe, the breakthrough underneath the pipe and the formation of a pathway are all resolved by the model.

In the wave-induced scour case, the migration of the vortex from one side to the other side of the pipe is resolved by LES. The response of the bed surface to the oscillatory flow is resolved well. The bed profile reproduced by the model is in good agreement with the measurements. In addition, it is found that in both current-induced scour case and wave-induced scour case, the regions of high vorticity overlap with those of high sub-grid scale eddy viscosity. Particles are also found to be in those regions. It indicates the importance of the interaction among the hydrodynamics, turbulence and particle motion.

Chapter 6

Discussion, Conclusion and Future Work

The model is calibrated and validated prior to applying it to example cases. The capacity of the model to resolve the hydrodynamics, sediment transport and scour development has been presented in the preceding chapters. In this chapter, discussions of the present work, regarding the particle modelling approach and the Euler-Lagrange modelling, and answers to the questions proposed in the Chapter 1 are presented. Suggestions for future work are outlined at the end of the chapter.

6.1 Discussion

6.1.1 Particle Modelling Approach

Advantages

A particle approach has rarely been implemented in scour models. However, considering the discrete particle nature of the sediment phase, a particle approach is the proper way forward to model sediment transport and scour processes. In the present work, the sediment is traced using the particle approach in a Lagrangian perspective. Forces acting on a particle are the deterministic factors regarding the particle motion. This is a major advantage to reflect the detailed physics at the particle scale, as opposed to most existing scour models, which are highly dependent on empirical relations and parameterisations. Consequently, many uncertainties involved in modelling sediment transport and scour processes using the conventional approach can be removed. Such empirical formulas as the drag coefficient are still necessary in the present model. However, compared to other types of scour models, only a minimum amount of empiricism is included. This enables the present model to reflect the physics to the largest extent.

Firstly, governed by the forces acting on the particles, the influences of the flow on the sediment pick-up from the bed and the subsequent suspension in the water column are no longer dependent on empirical formulas and parameters to model

the entrainment rate, the bed load transport rate, etc. The physical processes like entrainment, suspension and deposition are directly determined by the net force acting on a particle. It is much more physical and generic than employing the empirical formulas and parameterisations, which are usually derived under certain experimental conditions and thus limited to those specific scenarios.

Secondly, the motion of the bed is determined by the collective movement of millions of particles, rather than the simple mass conservation principle of the Exner Equation. By resolving the particle motion straightforwardly according to the physics, the initiation of the particle motion and the development of the bed profile is not restricted by certain rules as imposed in continuum models. The model is able to initiate scour development from an initially flat bed without any gap between the bed and the cylinder, and no special treatment is needed, which few models to date are capable of doing so. The onset of scour, tunnel erosion and lee-wake erosion are all resolved by the model. In addition, the rapid scour development and steep slopes are also well captured by the model without the limitation as observed in mesh deformation type models.

Thirdly, the particles in the water column can be treated separately from the fluid motion, which leads to a better description of the sediment suspension process compared to the conventional advection-diffusion concept that is developed for continuum type models. Such a process is particularly important when the differences between the flow and the particle motion are large, for example in sheet flow conditions.

However, the advantages of the particle approach come at a price regarding the

computational expense. Although updating the particle velocity and position is straightforward, and the concept of parcel is introduced to reduce computational costs, the number of parcels involved in the calculation is still very large for scour problems, usually greater than the number of cells. For example, in the current-induced scour case, there are $36,164$ Eulerian cells, and $188,160$ Lagrangian parcels. Consequently, the update of the particles requires a large amount of time. Moreover, to better resolve the particle motion, Lagrangian sub-time steps are adopted in the particle tracking method, which obviously increases the overheads. To give a brief impression, in the current-induced scour case, it took approximately 6 hours and 40 minutes to produce simulation results of one second using a single modern processor on the high performance computer (HPC).

Formulation

The forces acting on a particle are the deterministic factors regarding the particle motion. However, certain empirical formulas or approximations are still needed to represent forces like the hydrodynamic drag force and the inter-particle stress. The drag coefficient involved in the drag force is one of the major considerations in terms of formulation due to the importance of the drag force in the fluid-solid interactions. The drag coefficient selected here has been employed in several other studies based on the MP-PIC method, where the solid volume fraction is an important factor. The appropriate involvement of the solid volume fraction in the drag coefficient is essential. Although the drag coefficient used in the present model has proven to work in other MP-PIC models, it is important to validate and verify its suitability in sand transport and scour modelling.

The inter-particle stress is another term that needs special formulation. The stress model employed in the present work is a conceptual continuum model, which has its merits in simplicity, computational efficiency, and compatibility with the Eulerian-Lagrangian framework. However, because of its conceptual nature, it is not fully able to represent the inter-particle effects. It reflects the particle collision effect to a certain extent, nevertheless, it cannot stop particles from over-packing on its own. Consequently, special treatment needs to be implemented to compensate this inability.

Such formulations will lead inevitably to uncertainties in the model results. This issue arises from the lack of knowledge in the physical processes at the particle scale. However, despite these deficiencies, the present model is able to predict the hydrodynamics, sediment transport and bed scour process accurately when compared with measurements. To a large extent, these results may suggest that the detailed micro-processes at the particle scale are less significant to the overall hydrodynamics and the scouring of the sandy bed. The self-organising of the bed materials can be determined by the usual macro-scale parameters used in the conventional transport models, such as the water depth, the flow speed, the turbulence viscosity, the waver period, the orbital velocity, the median grain diameter, etc.

Implementation

The particle motion is calculated on a per particle basis. Particles are advanced based on the given flow information, which is interpolated to the discrete particle

positions, and the particle properties, e.g., the median grain size and specific gravity. Several assumptions have been adopted in the calculation.

For example, all the particles are assumed to be spherical with the same diameter, which is a common assumption used in sediment transport and scour models. The irregularity in the particle shape and the distribution of the particle size are therefore neglected. However, the reality is that the sediment particles have different shapes and sizes as well as different specific gravity. It implies that the present model works better for well-sorted non-graded sand. Nevertheless, in the present particle module, the particle properties including the shape and size are affiliated to each parcel, which means that it is straightforward to have parcels with different properties from each other. The extension of the present model to account for various particle shape and size distribution is straightforward.

In addition, the impact of the mean flow on the particle motion is considered via the hydrodynamic drag force and the pressure gradient force. Whereas the impact of the instantaneous fluctuations in the flow is not taken into account based on the assumption that it is much less significant to the particle motion than the mean flow. However, the instantaneous fluctuations like the sub-grid scale eddies are of comparable scale with the particle size, especially for fine sand. Therefore, the dynamics between the turbulence fluctuation and the particles can be of vital importance at such micro scale, the ensemble effect may be negligible though.

The present implementation has proven to reproduce satisfactory results regarding the hydrodynamics, sediment transport and scour development. The above

assumptions are therefore considered to be sensible. In addition, the present implementation regarding the forces acting on a particle also facilitates the modification or extension of the present model to suit a variety of application areas. Its flexibility to allow inclusion or exclusion of a given force in the governing equation of the particle motion can cater for different study objectives, and enable the relative importance among the acting forces to be observed. For example, to study the scour development, the hydrodynamic drag force, the pressure gradient force, the gravitational force, the buoyant force and the inter-particle stress are included in the present study. If dilute particulate flows are the main study objective, it may also be necessary to include the viscous stress gradient term in the governing equation to account for the influence of the mean flow diffusivity on the particle motion. By contrast, the inter-particle stress can be neglected in very dilute particulate flows.

Furthermore, tracing the particles on a one-by-one basis allows the injection or removal of particles where needed. For example, when particles reach the outlet boundary in the current-induced pipeline scour case in Section 5.4.1, they are removed from the computation without any impact on the rest of the computation. The functionality of particle injection is also available in the present model. However, due to the lack of available laboratory tests, such functionality of the model is not included in the present work.

Validation

The present model has been validated with several experimental measurements at macro scale. However, the detailed measurement at the particle scale is not yet widely available and hence the uncertainties in the model's performance at micro-scale cannot be justified. In particular, the drag force on the individual particles cannot be validated directly but through the particle fall velocity tests. It reflects the current lack of knowledge in the micro-scale processes and the difficulty to approach or even obtain validated micro-scale measurements.

6.1.2 Euler-Lagrange Multiphase Approach

Advantages

The model is designed to study the scour development around offshore structures. Aiming to reveal the scour mechanics involved, an Euler-Lagrange multiphase approach is adopted to represent the inherent properties of the full three phases, i.e., water, air and sediment, and to resolve each phase according to the physics. The fluid phase, i.e., the mixture of water and air, is resolved by solving the modified Navier-Stokes equations on an Eulerian grid. The VOF method is incorporated via the two-fluid methodology to resolve the free surface so as to eliminate the inaccuracy in scour prediction due to the rigid lid assumption. The solid phase, i.e., the sediment particles, is governed by Newton's Law of Motion. Therefore,

the physics of the particle motion is implemented straightforwardly in the model, and the dependence on empirical relations is removed largely as discussed in the preceding section.

In the present scour model, the solid phase is resolved using the Lagrangian particle approach, therefore, the micro processes are resolved at the particle scale. The fluid phase is solved as a continuum on an Eulerian grid. By fully coupling the Lagrangian framework and the Eulerian computational grid, the ensemble effect of the micro processes is reflected on the Eulerian grid and subsequently imposed on the fluid phase. Likewise, the particles located in different parts of the Eulerian grid can receive the correct amount of impact from the fluid phase. The fully coupled system has a major advantage that the flow-particle interactions are realised and updated in real time. The particles are advanced by the instantaneous hydrodynamic drag force, pressure gradient force as imposed by the ambient flow, and the flow is influenced by the particles through the interphase momentum transfer. In contrast, in the Eulerian approach adapting Exner Equation method, it is common practice to update the flow field at a small hydrodynamic time step while the bed movement is updated at a much larger interval, on the assumption that the bed movement is very small over a given number of hydrodynamic time steps. Such methods cannot resolve the flow-sediment interaction as accurately as the present model partly due to the delay in the response between the two phases.

In addition, as the most important driving force to initiate particle motion, the seepage flow inside the bed underneath the pipeline is a key feature to be resolved. In the present model, the porous nature of the bed is well resolved due to the Euler-Lagrange multiphase approach, where both the fluid and solid phase are represented inherently and the interactions between the two phases are correctly

interpreted. Consequently, the pressure difference and the seepage flow are captured well, and the model is able to resolve the onset of scour naturally. Whereas such a bed response is difficult to achieve for the Eulerian approach with the Exner Equations because of the continuum assumption of the bed and the isolated contact of the fluid and solid phase apart from at the bed surface, which relies on empirical relations for bed deformation.

Euler-Lagrange models are generally considered to be computational efficient, particularly compared to Lagrangian models. A further benefit of the Euler-Lagrange coupling is that some computational efforts can be reduced by using the ensemble information instead of the discrete particle information. For example, the solid volume fraction, which integrates the discrete particles information onto the Eulerian grid, facilitates the utilisation of continuum models to calculate the inter-particle stress and therefore save computational efforts. On the other hand, such convenience and efficiency may be at the expense of accuracy. The ensemble variables on the Eulerian grid only retain information at the Eulerian grid scale, and the information at discrete particle scale is lost. Therefore, it may lose the accuracy needed to correctly represent the physical effects, which could lead to accumulated errors or even incomplete representation of the desired physical effects. For example, the continuum model of the inter-particle stress is used to represent the particle collision effect, which consumes much less computational efforts than a Lagrangian collision model. However, the continuum model itself cannot prevent particles from over-packing as a result of the continuum approximation and the very limited information used, i.e., the solid volume fraction only. However, even if it is affordable to use a Lagrangian collision model, the knowledge on the processes involved in scour development at a particle scale has rarely been reported. Therefore, assumptions and approximations still seem inevitable. The potential influence of such processes on scour development and the subsequent impact of

the ensemble effect are also largely unknown, which can be possibly studied by laboratory experiments or preferably DNS.

Implementation

To achieve the fully coupled effect in the Euler-Lagrange multiphase approach, the particle tracking method to accurately position a particle on the Eulerian grid and the interpolation of variables from the Eulerian grid to the discrete particle positions are the two most important techniques. The interpolation method used in the model is the linear interpolation embedded in OpenFoam®. One may argue that linear interpolation is not accurate enough. However, considering that the particles are at sub-grid scale, and the grid size is usually small as well, the inaccuracy arising from such simple interpolation method can be considered acceptable. A more advanced interpolation method can certainly be employed in the future for comparison.

The particle tracking method has been described in Section 3.3.7, and it has been proven to position particles accurately on the Eulerian grid. However, for very fine particles, it usually takes longer to track due to the smaller particle time scale and consequently smaller Lagrangian sub-time-step. Simulations also show that fine particles sometimes hang in the tracking loop. A sophisticated remedy for this issue may be required in future development.

In the implementation, the solid volume fraction is a very important bridge between the hydrodynamic module and the particle module. It stores the collective effect of the particle position, and is involved in the calculation of the flow-particle interactions, in which the interphase momentum transfer is of vital importance. However, the implementation of the interphase momentum transfer cannot be verified quantitatively but has to be examined through its physical effect visually.

6.1.3 Model Application

A summary of the model applications is presented in Table 6.1. Different hydrodynamic conditions are tested, with or without a structure, and various turbulence models are employed. Good performance of the model is achieved overall, even under challenging conditions like plunging waves and oscillatory sheet flow. Regarding the scour process, the maximum scour depth and the slope underneath the pipeline are predicted very well. LES is a reliable choice to resolve the detailed flow structures especially immediately above the bed, which have a strong influence on the ultimate scour pattern. Moreover, in this multiphase Eulerian-Lagrangian framework, the particles distributions are well resolved. Particles are found to have preferential distributions around high vorticity regions in the sediment transport and scour processes, which is consistent with the finding by Balachandar and Eaton[5] regarding heavy particles (specific gravity to water greater than 1).

Calculating the forces acting on the particles to directly determine the particle motion and the realisation of the four-way coupling in the present model make it

Test	Processes involved	Structure	Turbulence model	Results
Vertical pile under currents	Current	Vertical pile	$k-\varepsilon$	Velocity profiles well predicted; 3D flow features captured; discrepancies close to bed at upstream.
Plunging wave test	Wave	Slope	$k-\omega$ SST	Water surface elevation, velocity and kinetic energy predicted well; better results in shoaling zone and surf zone than breaking zone.
Sheet flow test	Wave Sand transport	None	LES	Velocity discrepancies close to bed; sediment concentration well predicted, with discrepancies at bed surface.
Current-induced scour	Current Sand transport Scour process	Horizontal pipeline	$k-\omega$; LES	Flow structure and turbulence characteristics well resolved; particle distribution and bed profile predicted well; mechanics of onset of scour revealed; tunnel erosion and lee-wake erosion stages captured.
Wave-induced scour	Wave Sand transport Scour process	Horizontal pipeline	LES	Bed profile predicted well; particles' response to waves well represented.

TABLE 6.1: Model applications.

a natural modelling approach for scour studies. The tunnel erosion and lee-wake erosion stages are well captured, where the vortices in the flow have a significant influence on the scour process. In addition, onset of scour is also resolved without additional numerical assumptions or approximations. The driving mechanisms like the pressure difference between the upstream and downstream side are well represented. However, the treatment of the fully packed bed is still a very challenging task for scour modelling. Although the particle interaction is reflected by the inter-particle stress, it is not adequate enough to deal with the complexity of a fully packed bed robustly. Therefore future work is proposed in Section 6.3.

6.2 Conclusions

Q1. How can the free surface effect and a mobile sandy bed be simulated simultaneously with the flow dynamics in a CFD model?

The multiphase modelling approaches enable the simulation of more than one phase simultaneously. In particular, the Euler-Lagrange multiphase approach has been proven in the present work to be capable of dealing with the full three phases involved in scour problems, i.e., water, air and sediment. For the flow dynamics, a modified two-fluid methodology is adopted to simulate the fluid phase, i.e., the mixture of water and air, as a continuum. The VOF method is incorporated to capture the free surface. The solid phase, i.e., sediment, is governed by Newton's Law of Motion in the Lagrangian framework, and it is traced on a per particle basis. The fluid phase and the solid phase are fully coupled, and the interactions

between particles are also resolved. Therefore, the mobile sandy bed and the flow dynamics are influencing each other, and the response from each other is always instantaneous.

Q2. How can the flow-sediment interactions be represented effectively in a CFD model?

Firstly, it is important to represent the flow and sediment in their natural way, respectively. In the present model, the flow is simulated as a continuum using the Navier-Stokes Equations, and the sediment is represented by discrete particles following Newton's Law of Motion. Therefore, the inherent properties of each phase are correctly represented. Secondly, both phases are connected by the Eulerian computational grid, where the interactions between them can be calculated efficiently. The influence of the flow on the particles are realised by the hydrodynamic forces acting on a particle, and the impact of the particles on the flow is imposed via the interphase momentum transfer, which is added to the momentum equation of the flow. In this way, the flow-sediment interaction is represented with a sound theoretical footing and a minimum amount of empiricism. Consequently the effective representation of the interaction is achieved.

It is noteworthy that flow-sediment interaction is a rather complex process. The interaction is certainly not limited to those realised in the present work. For example, the mass coupling and energy coupling are also other aspects apart from momentum coupling; the hydrodynamic forces acting on a particle also includes lift force etc. among others. However, the hydrodynamic forces included in the present work and the momentum coupling are the predominant ones, and are

therefore implemented in the model in the first place. Other aspects are proposed for future work.

Q3. How does the particle motion initiate in the scour process?

Particle motion initiates when the agitating force on a particle outweighs the resisting force. In the scour process, particularly pipeline scour, the agitating force are the hydrodynamic drag force and the pressure gradient force, and the resisting force are the gravitational force and inter-particle stress. The pressure gradient between the upstream and downstream end of the pipe induces a seepage flow in the bed. When the hydrodynamic forces caused by the seepage flow outweigh those resisting forces, particle motion is initiated.

Q4. How does the flow structure, especially the turbulence characteristics, affect the scour pattern?

Flow condition, structure properties, including the structure size, shape, orientation etc., and the seabed formation are the three aspects that determine the ultimate scour pattern. Flow-structure-seabed interactions are also dynamic processes that change constantly. Regarding the flow structure, particularly in pipeline scour cases, the scour pattern under current is different from that under waves. However, in both cases, vortices are the deterministic flow structure that affect the scour pattern. The turbulence characteristics, in particular, the sub-grid scale eddy viscosity is always high in those regions where vortices exist. In current-induced scour, the flow acceleration underneath the pipe during tunnel erosion

shapes the scour hole rapidly. Small vortices are formed immediately above the bed at the upstream once a mild slope is formed, and the vortex flow at the downstream side of the pipe dominates the lee-wake erosion, which gradually erodes away the downstream mount formed by deposition. The flow structures generated with $k-\omega$ model and LES are different from each other. The former hardly resolves the vortices at the upstream side, resulting in a higher mount than the experimental measurement; and the lee-wake vortices are higher above the bed and less organised than those resolved by LES.

In wave-induced scour, due to the oscillatory nature of the flow, vortices develops on both sides of the pipe. Gentle slopes therefore form on both sides underneath the pipe. The development of the scour hole underneath the pipe takes a longer time than current-induced scour even though the main flow magnitude is comparable to each other. This is attributed to the constantly changing flow magnitude and direction. Not all the time is the flow strong enough to erode the bed surface. Instead, only during a small period of a wave cycle is the flow strong enough to substantially erode the bed. In addition, when the flow changes direction, the pathway underneath the pipe and the gentle slope formed on one side of the pipe can be refilled again by sand, and the bed surface can recover to a level that is observed in the early stage. Only when sufficient sand has been transported farther away from the pipe does the scour hole gradually stabilise and erosion become continuous.

Q5. How does the particle motion affect the overall scour process?

Seabed is made of individual sediment particles. The ensemble effect of the moving

particles during scour process will determine the ultimate scour pattern. Particle motion is found to be very active in the lee-wake side under a steady current. Gradually when the flow is developed, particle suspension tends to calm down, and instead the particles move along the bed surface, i.e., bed load transport is more crucial to the ultimate scour pattern. In wave-induced scour, the constantly changing flow field due to the oscillatory nature of waves makes particle suspension significant all the time. Like in current-induced scour, particle distribution under waves is also found to be dense in high eddy viscosity regions, and avoiding the core of high vorticity regions. The entrainment and settling of particles are largely dominated by the flow, and their ensemble effect together with the particles moving along the bed surface will determine the ultimate bed profile.

6.3 Suggestions for Future Work

A novel scour model using the Euler-Lagrange multiphase approach has been developed in the present work. Its performance in the hydrodynamics, sediment transport, and scour development has been well demonstrated. With the encouraging performance and its promising potential, further model development, more detailed studies of the processes involved in scour development, and applications to a wider range of scenarios are anticipated. Suggestions for future work are therefore outlined in this section.

6.3.1 Further Model Development

Various Particle Properties

In the present model, the sediment particles are considered as non-cohesive spherical sand of a uniform size. In reality, sediment particles are of different properties, which can impact the scour process and the ultimate scour depth. For example, Pluim-van der Velden and Bijker[63] studied the impact of cohesive sediment on the scour process under steady current, and found that it has impact throughout the whole scour process. Compared to a sand bed, for a sand-silt mixture, a higher critical shear stress is needed for the initiation of particle motion; no deposition occurs at the downstream side of the pipe; and the scour depth is generally smaller[63].

The particle modelling approach employed in the present work enables it to assign additional properties to each particle, including particle size, shape, cohesion etc. By introducing those extra variables to the particles, particles can have various sizes, shapes and cohesion as needed. This attractive feature can be easily realised in the model. However, with these additional properties, the corresponding formulations to take into account each of these properties properly are the major challenges. The impact of particle size distribution, particle shape and cohesion have been studied occasionally in the past, most of which are conducted under specific experimental conditions. General findings are reported similar to the one in the preceding paragraph, and some empirical relations are derived. However,

there is still a lack of knowledge in more generic formulations regarding the flow-particle and particle-particle interaction with these additional factors, especially at the particle scale. There is yet a widely adopted formulation, or an empirical relation. Moreover, there is also a need for reliable experimental data for calibration and validation purposes.

Elaborate Implementation of Forces

The hydrodynamic drag force, pressure gradient force, net buoyant force and the inter-particle stress are implemented in the present model, which are the most prominent forces for dense dispersed flow in the scour process. To better resolve the particle motion and the flow-particle interaction, a more elaborate implementation of the forces acting on a particle and a more detailed examination of the interphase momentum transfer can be useful for further development. The viscous stress force, added mass force, and lift force among others can be investigated and implemented in the present model.

In addition, the inter-particle collision and friction need to be better interpreted in the model. Currently, the inter-particle stress is adopted to account for the particle translational collision effect, whereas the rotational collision and the friction effect are not represented. A proper representation of such effects can further improve the robustness of the model. The prediction may be improved as well. However, the understanding of the inter-particle collision and friction at the particle scale is still far from satisfactory. Studies under specific experimental conditions have

been carried out, whereas a generic understanding or formulation with a sound theoretic footing is not evident to date.

Turbulence-Particle Interaction

The enhancement in the turbulence level around the structures is one of the key factors leading to an enhanced sediment transport capacity and therefore the occurrence of scour. However, the knowledge of the turbulence enhancement is still an area of uncertainty. Using LES, the flow field is resolved with very detailed structures. The turbulence characteristics are also resolved. The distribution pattern of the sub-grid scale eddy viscosity is found to follow that of the flow vorticity field, around which the particles are also densely distributed, providing insight on the implications between the hydrodynamics, turbulence and the particle distribution.

Employing the MP-PIC particle modelling approach, the particles can be resolved at the sub-grid micro scale. The interaction between the particles and the turbulence in the fluid phase can therefore be investigated. However, the knowledge of the turbulence-particle interaction is still one of the most challenging topics in multiphase flow due to the stochastic nature of both. The enhanced turbulence dissipation due to the presence of the particles and the transfer of the kinetic energy from the flow to the particles are two of the important mechanisms identified[5]. Furthermore, the influence of the turbulence on the mean and fluctuating forces

is also non-negligible at micro scale. However, studies on such effects remain inconclusive due to their complex nature and the difficulties in obtaining accurate experimental measurements.

Therefore, an appropriate implementation of such processes still remains an open topic with the limited theoretical footing. Some empirical and semiempirical relations have been reported. Balachandar and Eaton[5] reviewed the experimental and numerical studies in turbulent dispersed multiphase flow, in particular dilute dispersed flow, regarding the preferential concentration of particles, the effect of turbulence on the interphase coupling and the modulation of the turbulence due to the presence of the particles. As concluded by Balachandar and Eaton[5], the mechanisms of turbulence modulation and the parametric dependence are still poorly understood, even in dilute dispersed flow. In dense dispersed flow such as the sheet flow regime, the turbulence-particle interactions can be even more complex. Fundamental investigations in this field is widely needed.

The turbulence-particle interaction is a very important topic for multiphase flow. However, the ensemble effects of such micro scale processes on the sediment transport and scour processes remain largely unknown. The Euler-Lagrange framework in the present model makes the investigation possible, the formulation and implementation need careful consideration though.

6.3.2 Model Application

The model has been successfully applied to benchmark pipeline scour cases. The scour development under currents and waves respectively have been well resolved. The scour development under combined current and waves would be the next step. In addition, the onset of scour and the tunnel erosion stage of the scour development have been successfully resolved by the model. Expanding the numerical capacity of the model to study the equilibrium scour status by realisation of parallelisation can be promising. Moreover, the two-dimensional features in pipeline scour have been investigated successfully in the current application, whereas the three-dimensional features such as the spread of scour along the pipeline, backfilling and self-burial process are yet to be investigated.

Apart from that, in the case of a steady current passing a vertical pile mounted on a rough rigid bed, the streamwise velocity profiles are resolved very well, small deviations exist near the bed though. The three-dimensional feature of the flow is well captured, which is very encouraging for future application of the model to the scour development around a vertical pile, which is another common structure type in the offshore area. Obviously, this would also rely on the realisation of parallelisation due to the large amount of computational resources needed.

Furthermore, the application of the model to multiple structures in the offshore area is also anticipated. For example, the local scour at adjacent pipelines or vertical piles in a tandem arrangement or side-by-side arrangement, and even the global scour in an array of structures. The secondary scour effect with scour

protections can also be studied once the parallelisation is realised.

6.3.3 Conclusions

Studying the scour process using the Euler-Lagrange multiphase approach has proven its many advantages over the conventional continuum approaches. The particle modelling approaches like the MP-PIC method are powerful in their ability to resolve the scour process at the particle scale, and their potential to reveal more detailed micro scale processes is very encouraging. However, the lack of knowledge in the particle motion, particularly the flow-particle and particle-particle interactions is a major barrier for further development. Nevertheless, it is envisaged that studying the sediment transport and scour development at the particle scale is an inevitable way forward to resolve the detailed processes, reveal the mechanism and improve the predictions. Realisation of parallelisation is another aspect for further development such as to expand the model application to study the three-dimensional features of the scour process and the scour at multiple structures.

References

[1] R.V. Ahilan and J. Sleath, *Sediment transport in oscillatory flow over flat beds.*, Journal of Hydraulic Engineering. **113** (1987), 308–322.

[2] K. Anastasiou and C. T. Chan, *Solution of the 2d shallow water equations using the finite volume method on unstructured triangular meshes*, International Journal for Numerical Methods in Fluids **24** (1997), no. 11, 1225–1245.

[3] M.J. Andrews and P.J. O'Rourke, *The multiphase particle-in-cell (mp-pic) method for dense particulate flows*, International Journal of Multiphase Flow **22** (1996), no. 2, 379 – 402.

[4] C. J. Baker, *The laminar horseshoe vortex*, Journal of Fluid Mechanics **95** (1979), 347–367.

[5] S. Balachandar and J.K. Eaton, *Turbulent dispersed multiphase flow*, Annual Review of Fluid Mechanics **42** (2010), no. 1, 111–133.

[6] J.E. Bardina, P.G. Huang, and T.J. Coakley, *Turbulence modeling validation, testing, and development*, Tech. report, NASA Technical Memorandum 110446, 1997.

[7] P. Beaudan and P. Moin, *Numerical experiments on the flow past a circular cylinder at sub-critical reynolds number*, Tech. Report TF-62, Stanford University, 1994.

[8] H. N. C. Breusers and A. J. Raudkivi, *Scouring, iahr-airh hydraulic structures design manual*, Balkema, Rotterdam, 1991.

[9] A.J. Cihonski, J.R. Finn, and S.V. Apte, *Volume displacement effects during bubble entrainment in a travelling vortex ring*, Journal of Fluid Mechanics **721** (2013), 225–267.

[10] M. Dixen, B.M. Sumer, and J. Fredsøe, *Numerical and experimental investigation of flow and scour around a half-buried sphere*, Coastal Engineering **73** (2013), no. 0, 84 – 105.

[11] H. Eilers, *The viscosity of the emulsion of highly viscous substances as function of concentration*, Kolloid-Zeitschrift **97** (1941), no. 3, 313–321.

[12] A. Einstein, *Eine neue bestimmung der molekuldimensionen (german) [a new determination of molecular dimensions]*, Annalen der Physik **19** (1906), 289306.

[13] F. Engelund and J. Fredsøe, *A sediment transport model for straight alluvial channels*, Nordic Hydrology **7** (1976), 293–306.

[14] S. Ergun, *Fluid flow through packed columns*, Chemical Engineering and Processing **48** (1952), 89–94.

[15] J. H. Ferziger and M. Peric, *Computational methods for fluid dynamics*, Springer-Verlag, 2002.

[16] D.R. Fuhrman, C. Baykal, B.M. Sumer, N.G. Jacobsen, and J. Fredsøe, *Numerical simulation of wave-induced scour and backfilling processes beneath submarine pipelines*, Coastal Engineering **94** (2014), no. 0, 10 – 22.

[17] D. Gidaspow, *Multiphase flow and fluidization: Continuum and kinetic theory descriptions*, Academic Press, 1994.

[18] A.J. Grass, *Sediment transport by waves and currents*, University College, London, Dept. of Civil Engineering, 1981.

[19] F. Hajivalie, A. Yeganeh-Bakhtiary, H. Houshanghi, and H. Gotoh, *Euler-lagrange model for scour in front of vertical breakwater*, Applied Ocean Research **34** (2012), 96 – 106.

[20] M. Hamidipour, J. Chen, and F. Larachi, *Cfd study on hydrodynamics in three-phase fluidized beds-application of turbulence models and experimental validation*, Chemical Engineering Science **78** (2012), no. 0, 167 – 180.

[21] J.M. Harris and R.J.S. Whitehouse, *Marine scour: Lessons from natures laboratory*, Scour and Erosion: Proceedings of the 7th International Conference on Scour and Erosion, Perth, Australia, 2-4 December 2014, CRC Press, 2014, p. 19.

[22] S. E. Harris and D. G. Crighton, *Solitons, solitary waves, and voidage disturbances in gas-fluidized beds*, Journal of Fluid Mechanics **266** (1994), 243–276.

[23] M. Heidarpour, H. Afzalimehr, and E. Izadinia, *Reduction of local scour around bridge pier groups using collars*, International Journal of Sediment Research **25** (2010), no. 4, 411 – 422.

[24] P. Higuera, J.L. Lara, and I.J. Losada, *Realistic wave generation and active wave absorption for navier-stokes models: Application to openfoam.*, Coastal Engineering **71** (2013), 102–118.

[25] C Hirsch, *Numerical computation of internal and external flows*, John Wiley & Sons, Ltd, 1991.

[26] C.W Hirt and B.D Nichols, *Volume of fluid (vof) method for the dynamics of free boundaries*, Journal of Computational Physics **39** (1981), no. 1, 201 – 225.

[27] P. Hjorth, *Studies on the nature of local scour*, Bulletin series A / Department of Water Resources Engineering, Lund Institute of Technology, University of Lund, AV Centralen, 1975.

[28] R. I. Issa, *Solution of the implicitly discretised fluid flow equations by operator-splitting.*, Journal of Computational Physics **62** (1986), 40–65.

[29] N G Jacobsen, D R Fuhrman, and J Fredsøe, *A wave generation toolbox for the open-source cfd library: Openfoam®*, Int. J. Numerl. Meth. Fluids **70** (2012), no. 9, 1073–1088.

[30] H. Jasak, *Error analysis and estimation for the finite volume method with applications to fluid flows*, Ph.D. thesis, Imperial College, University of London, 1996.

[31] H.R. Jensen and B.L. Jensen, *Flow visualization and numerical simulation of the flow around marine pipelines on an erodible bed.*, Proc. 8th Int. Conf. on Offshore Mech. and Arctic Engrg., Amer. Society of Mech. Engrs. **5** (1989), 129–136.

[32] T. Karambas, *2dh non-linear dispersive wave modelling and sediment transport in the near shore zone*, Coastal Engineering Proceedings (1998), 2940–2953.

[33] S. Karimipour and T. Pugsley, *Application of the particle in cell approach for the simulation of bubbling fluidized beds of geldart a particles*, Powder Technology **220** (2012), no. 0, 63 – 69, Selected Papers from the 2010 NETL Multiphase Flow Workshop.

[34] A. Khosronejad, C. Hill, S. Kang, and F. Sotiropoulos, *Computational and experimental investigation of scour past laboratory models of stream restoration rock structures*, Advances in Water Resources **54** (2013), 191 – 207.

[35] H.S. Kim, M. Nabi, I. Kimura, and Y. Shimizu, *Numerical investigation of local scour at two adjacent cylinders*, Advances in Water Resources **70** (2014), 131 – 147.

[36] A. Kumar, U.C. Kothyari, and K.G.R. Raju, *Flow structure and scour around circular compound bridge piers a review*, Journal of Hydro-environment Research **6** (2012), no. 4, 251 – 265.

[37] B.E. Launder and D.B. Spalding, *The numerical computation of turbulent flows*, Computer Methods in Applied Mechanics and Engineering **3** (1974), no. 2, 269 – 289.

[38] T.L. Lee, D.S. Jeng, G.H. Zhang, and J.H. Hong, *Neural network modeling for estimation of scour depth around bridge piers*, Journal of Hydrodynamics, Ser. B **19** (2007), no. 3, 378 – 386.

[39] K. Levenberg, *A method for the solution of certain non-linear problems in least squares*, Quarterly Journal of Applied Mathmatics **II** (1944), no. 2, 164–168.

[40] E. Leveque, F. Toschi, L. Shao, and J.P. Bertoglio, *Shear-improved smagorinsky model for large-eddy simulation of wall-bounded turbulent flows*, Journal of Fluid Mechanics **570** (2007), 491–502.

[41] F. Li and L. Cheng, *A numerical model for local scour under offshore pipelines.*, J Hydr Eng **125** (1999), 400–406.

[42] F. Li and L. Cheng, *Numerical modelling of local scour around offshore pipelines*, VI Journees nationales Genie Civil-Genie Cotier, Caen, France, 17-19 May 2000, pp. 123–136.

[43] F. Li and L. Cheng, *Numerical simulation of pipeline local scour with lee-wake effects.*, Int J Offshore Polar Eng **10** (2000), 195–199.

[44] M. Li, S. Pan, and B.A. O'Connor, *A two-phase numerical model for sediment transport prediction under oscillatory sheet flows*, Coastal Engineering **55** (2008), no. 12, 1159 – 1173.

[45] D. Liang, L. Cheng, and K. Yeow, *Numerical study of the reynolds-number dependence of two-dimensional scour beneath offshore pipelines in steady currents*, Ocean Engineering **32** (2005), no. 13, 1590 – 1607.

[46] X. Liu and M.H. Garcia, *Three-dimensional numerical model with free water surface and mesh deformation for local sediment scour*, Journal of Waterway, Port, Coastal, and Ocean Engineering **134** (2008), no. 4, 203–217.

[47] X. Liu, B.J. Landry, and M.H. Garcia, *Two-dimensional scour simulations based on coupled model of shallow water equations and sediment transport on unstructured meshes*, Coastal Engineering **55** (2008), no. 10, 800 – 810.

[48] C. K. K. Lun, S. B. Savage, D. J. Jeffrey, and N. Chepurniy, *Kinetic theories for granular flow: inelastic particles in couette flow and slightly inelastic particles in a general flowfield*, Journal of Fluid Mechanics **140** (1984), 223–256.

[49] G.B. Macpherson, N. Nordin, and H.G. Weller, *Particle tracking in unstructured, arbitrary polyhedral meshes for use in cfd and molecular dynamics*, Commun. Numer. Meth. Engng **25** (2009), 263–273.

[50] Y. Mao, *The interaction between a pipeline and an erodible bed*, Institute of Hydrodynamics and Hydraulic Engineering København: Series paper, Institute of Hydrodynamics and Hydraulic Engineering, Technical University of Denmark, 1986.

[51] S. Mayer and P. Madsen, *Simulation of breaking waves in the surf zone using a navier-stokes solver*, Coastal Engineering 2000, 2000, pp. 928–941.

[52] B.W. Melville and S.E. Coleman, *Bridge scour: By bruce w. melville, stephen e. coleman*, Water Resources Publications, 2000.

[53] F. R. Menter, *Two-equation eddy-viscosity turbulence models for engineering applications*, AIAA Journal **32** (1994), no. 8, 1598–1605.

[54] Y.Q. Nguyen and J.C. Wells, *Modeling bedform development under turbulent flows using large-eddy-simulation and immersed-boundary-method*, Computers & Fluids **111** (2015), 105 – 113.

[55] N. Nordin, *Complex chemistry modemodel of diesel spray combustion.*, Ph.D. thesis, Chalmers University of Technology, Gothenburg, 2000.

[56] T. O'Donoghue and S. Wright, *Concentrations in oscillatory sheet flow for well sorted and graded sands*, Coastal Engineering **50** (2004), no. 3, 117 – 138.

[57] T. O'Donoghue and S. Wright, *Flow tunnel measurements of velocities and sand flux in oscillatory sheet flow for well-sorted and graded sands*, Coastal Engineering **51** (2004), no. 11, 1163–1184.

[58] T. O'Donoghue, S. Wright, S. Pan, M. Li, A. Davies, and J. Malarkey, *Numerical and experimental study of wave-generated sheet flow.*, International Conference on Coastal Engineering. World Scientific, Singapore. (2004), 16901702.

[59] S. Pagliara and I. Carnacina, *Influence of large woody debris on sediment scour at bridge piers*, International Journal of Sediment Research **26** (2011), no. 2, 121 – 136.

[60] N.A. Patankar and D.D. Joseph, *Lagrangian numerical simulation of particulate flows*, International Journal of Multiphase Flow **27** (2001), no. 10, 1685–1706.

[61] S.V. Patankar, *Numerical heat transfer and fluid flow*, Hemisphere Publishing Corporation, 1981.

[62] A.M. Penko, J. Calantoni, and D.N. Slinn, *Mixture theory model sensitivity to effective viscosity in simulations of sandy bedform dynamics*, OCEANS 2009, MTS/IEEE Biloxi - Marine Technology for Our Future: Global and Local Challenges, Oct 2009, pp. 1–9.

[63] E.T.J.M. Pluim-van der Velden and E.W. Bijker, *Local scour near submarine pipelines on a cohesive bottom.*, BOSS 92, 6th Intl Conf on the Behaviour of Offshore Structures. 7-10 July, London, UK., 1992.

[64] C.M. Rhie and W. L. Chow, *A numerical study of the turbulent flow past an isolated airfoil with trailing edge separation.*, AIAA J. **21** (1983), 1525–1532.

[65] J.E. Richardson and V.G. Panchang, *Three-dimensional simulation of scour-inducing flow at bridge piers.*, J. Hydraul. Eng. **124** (1998), no. 5, 530–540.

[66] P.L. Roe, *Approximate riemann solvers, parameter vectors, and difference schemes*, Journal of Computational Physics **43** (1981), 357–372.

[67] P.L. Roe, *Characteristic-based schemes for the euler equations*, Annual Review of Fluid Mechanics **18** (1986), no. 1, 337–365.

[68] B. Rogers, M. Fujihara, and A.G.L. Borthwick, *Adaptive q-tree godunov-type scheme for shallow water equations*, International Journal for Numerical Methods in Fluids **35** (2001), no. 3, 247–280.

[69] B.D. Rogers, A.G.L. Borthwick, and P.H. Taylor, *Mathematical balancing of flux gradient and source terms prior to using roes approximate riemann solver*, Journal of Computational Physics **192** (2003), no. 2, 422 – 451.

[70] A. Roulund, B. Sumer, J. Fredsøe, and J. Michelsen, *Numerical and experimental investigation of flow and scour around a circular pile*, Journal of Fluid Mechanics **534** (2005), 351–401.

[71] H. Rusche, *Computational fluid dynamics of dispersed two-phase flows at high phase fractions*, Ph.D. thesis, Imperial College, University of London, 2002.

[72] J.A. Sethian, *Level set methods: Evolving interfaces in geometry, fluid mechanics, computer vision, and materials science*, Cambridge Monographs on Applied and Computational Mathematics, Cambridge University Press, 1996.

[73] D. Snider, *An incompressible three-dimensional multiphase particle-in-cell model for dense particle flows*, Journal of Computational Physics **170** (2001), no. 2, 523–549.

[74] D.M. Snider, P.J. O'Rourke, and M.J. Andrews, *Sediment flow in inclined vessels calculated using a multiphase particle-in-cell model for dense particle flows*, International Journal of Multiphase Flow **24** (1998), no. 8, 1359 – 1382.

[75] D.M. Snider, P.J. O'Rourke, and M.J. Andrews, *An incompressible two-dimensional multiphase particle-in-cell model for dense particle flows*, La–13280-ms, Los Alamos National Lab., NM (United States), June, 1997.

[76] C.B. Solnordal, V. Kenche, T.D. Hadley, Y. Feng, P.J. Witt, and K.S. Lim, *Simulation of an internally circulating fluidized bed using a multiphase particle-in-cell method*, Powder Technology **274** (2015), no. 0, 123 – 134.

[77] B. Sumer, N. Christiansen, and J. Fredsøe, *The horseshoe vortex and vortex shedding around a vertical wall-mounted cylinder exposed to waves*, Journal of Fluid Mechanics **332** (1997), 41–70.

[78] B. Sumer and J. Fredsøe, *Scour below pipelines in waves*, Journal of Waterway, Port, Coastal, and Ocean Engineering **116** (1990), no. 3, 307–323.

[79] B. Sumer and J. Fredsøe, *Scour around pile in combined waves and current*, Journal of Hydraulic Engineering **127** (2001), no. 5, 403–411.

[80] B. Sumer and J. Fredsøe, *The mechanics of scour in the marine environment*, Advanced Series on Ocean Engineering, World Scientific, 2002.

[81] B. Sumer, J. Fredsøe, and N. Christiansen, *Scour around vertical pile in waves*, Journal of Waterway, Port, Coastal, and Ocean Engineering **118** (1992), no. 1, 15–31.

[82] B. Sumer, H. Jensen, Y. Mao, and J. Fredsøe, *Effect of lee wake on scour below pipelines in current*, Journal of Waterway, Port, Coastal, and Ocean Engineering **114** (1988), no. 5, 599–614.

[83] B. Sumer, Y. Mao, and J. Fredsøe, *Interaction between vibrating pipe and erodible bed*, Journal of Waterway, Port, Coastal, and Ocean Engineering **114** (1988), no. 1, 81–92.

[84] B.M. Sumer and J. Fredsøe, *Hydrodynamics around cylindrical structures*, Advanced Series on Ocean Engineering, World Scientific, 1997.

[85] B.M. Sumer, C. Truelsen, T. Sichmann, and J. Fredsøe, *Onset of scour below pipelines and self-burial*, Coastal Engineering **42** (2001), no. 4, 313 – 335.

[86] M. Syamlal, T.J. O'Brien, and W. Rojers, *Mfix documentation. theory guide. national technical information service, springfield, doe/metc-9411004, ntis/de9400087*, Tech. report, 1993.

[87] F.C.K. Ting and J.T. Kirby, *Observation of undertow and turbulence in a laboratory surf zone*, Coastal Engineering **24** (1994), 51 – 80.

[88] N. Tofany, M.F. Ahmad, A. Kartono, M. Mamat, and H. Mohd-Lokman, *Numerical modeling of the hydrodynamics of standing wave and scouring in front of impermeable breakwaters with different steepnesses*, Ocean Engineering **88** (2014), 255 – 270.

[89] L.C. van Rijn, *Principles of sediment transport in rivers, estuaries and coastal seas*, Principles of Sediment Transport in Rivers, Estuaries, and Coastal Seas, Aqua Publications, 1993.

[90] S. Wang, S. Guo, J. Gao, X. Lan, Q. Dong, and X. Li, *Simulation of flow behavior of liquid and particles in a liquidsolid fluidized bed*, Powder Technology **224** (2012), no. 0, 365 – 373.

[91] C.Y. Wen and Y.H. Yu, *Mechanics of fluidization*, Chemical Engineering Progress Symposium **Series 62** (1966), 100–111.

[92] R.J.S. Whitehouse, J.M. Harris, J. Sutherland, and J. Rees, *The nature of scour development and scour protection at offshore windfarm foundations*, Marine Pollution Bulletin **62** (2011), no. 1, 73 – 88.

[93] A. Yeganeh-Bakhtiary, M.H. Kazeminezhad, A. Etemad-Shahidi, J.H. Baas, and L. Cheng, *Euler-euler two-phase flow simulation of tunnel erosion beneath marine pipelines*, Applied Ocean Research **33** (2011), no. 2, 137 – 146.

[94] A. Yeganeh-Bakhtiary, B. Shabani, H. Gotoh, and S.S.Y. Wang, *A three-dimensional distinct element model for bed-load transport*, Journal of Hydraulic Research **47** (2009), no. 2, 203–212.

[95] AA Yeganeh-Bakhtiary, MM Zanganeh, EE Kazemi, L. Cheng, and Abd Wahab AK., *Eulerlagrange two-phase model for simulating live-bed scour beneath marine pipelines.*, ASME. J. Offshore Mech. Arct. Eng. **135** (2013), no. 3.

[96] T. Yoon and S. Kang, *Finite volume model for two-dimensional shallow water flows on unstructured grids*, Journal of Hydraulic Engineering **130** (2004), no. 7, 678–688.

[97] A. Yoshizawa, *Bridging between eddy-viscosity-type and second-order turbulence models through a two-scale turbulence theory*, Phys. Rev. E **48** (1993), 273281.

[98] M. Zanganeh, A. Yeganeh-Bakhtiary, and A.K. Abd Wahab, *Lagrangian coupling two-phase flow model to simulate current-induced scour beneath marine pipelines*, Applied Ocean Research **38** (2012), no. 0, 64 – 73.

[99] H. Zhang, H. Mizutani, H. Nakagawa, and K. Kawaike, *Euler-lagrange model for local scour and grain size variation around a spur dyke*, International Journal of Multiphase Flow **68** (2015), 59 – 70.

[100] Y. Zhang, M. Zhao, K.C.S. Kwok, and M.M. Liu, *Computational fluid dynamics-discrete element method analysis of the onset of scour around subsea pipelines*, Applied Mathematical Modelling (2015).

[101] M. Zhao, L. Cheng, and Z. Zang, *Experimental and numerical investigation of local scour around a submerged vertical circular cylinder in steady currents*, Coastal Engineering **57** (2010), no. 8, 709 – 721.

[102] M. Zhao, S. Vaidya, Q. Zhang, and L. Cheng, *Local scour around two pipelines in tandem in steady current*, Coastal Engineering **98** (2015), 1 – 15.

[103] Z. Zhao and H.J.S. Fernando, *Numerical simulation of scour around pipelines using an eulereuler coupled two-phase model*, Environmental Fluid Mechanics **7** (2007), 121–142 (English).

[104] H. Zhu, X. Qi, P. Lin, and Y. Yang, *Numerical simulation of flow around a submarine pipe with a spoiler and current-induced scour beneath the pipe*, Applied Ocean Research **41** (2013), 87 – 100.